Alteration, geochemistry, and paragenesis of the Midas epithermal gold-silver deposit, Elko County, Nevada

E.D. Leavitt* and G.B. Arehart
Department of Geological Sciences, MS-172, University of Nevada, Reno, Reno, Nevada 89557-0138

SUMMARY

The Ken Snyder mine in the Midas district is located in north-central Nevada along the eastern margin of the northern Nevada rift. Epithermal precious metal- and selenium-rich quartz-adularia-calcite veins formed in N- and NW-trending faults at 15.4 Ma, roughly coeval with rhyolitic magmatism. Patterns of alteration reflect effects of increasing temperature and water:rock reactions towards the Colorado Grande and Gold Crown veins and with time. Distal weak propylitic alteration (calcite-chlorite) gives way to moderate propylitic alteration (chlorite-calcite-pyrite-smectite), and increased wall rock replacement and veining closer to the main veins. An epidote isograd (first appearance of epidote) forms the contact between moderate and intense propylitic alteration (chlorite-pyrite-epidote-smectite-albite ± prehnite ± adularia). Haloes of potassic alteration (adularia-chlorite-pyrite/marcasite-smectite/illite-quartz) extend 30 m from veins. Fe-rich chlorite and increased abundances of pyrite occur closer to the main veins, and adularia, illite, and kaolinite are present in wall rocks. Formation of banded veins coincided with potassic alteration. High-grade crustiform veins are composed of alternating metal-rich and quartz-calcite-adularia-rich bands. The principal metal-bearing phases include naumannite, pyrite, chalcopyrite, electrum, sphalerite, and galena. Pathfinder elements typical of epithermal systems, including Hg, As, and Sb, as well as K form haloes above ore-grade veins. Base metals show no significant enrichment over the vertical interval studied.

ABSTRACT

Alteration, geochemistry, and paragenesis of the Colorado Grande and Gold Crown veins in the Ken Snyder mine, Midas district, demonstrate spatial and temporal variations that are similar to other epithermal bonanza vein systems. Alteration shows patterns of increasing temperature and water:rock reactions towards the main veins, and with time. The main types of alteration include: weak, moderate and intense propylitic; potassic, intense potassic and silicic-potassic; argillic; and silicic. Weak propylitic alteration (calcite-chlorite) is widespread and common in mafic volcanic rocks. Moderate propylitic alteration (chlorite-calcite-pyrite-smectite) extends up to 400 m from the main veins, exhibits an increase in replacement of wall rock minerals and veining, and is composed of mineral assemblages that indicate temperatures of ~200º to 230°C. An epidote isograd forms the boundary between moderate and intense propylitic alteration (chlorite-pyrite-epidote-smectite, lesser albite, ± prehnite in mafic rocks, +adularia in felsic rocks), and drapes over the main veins, recording paleoisotherms associated with upflow zones. These assemblages formed at

*zoracdavie@aol.com

Leavitt, E.D., and Arehart, G.B., 2005, Alteration, geochemistry, and paragenesis of the Midas epithermal gold-silver deposit, Elko County, Nevada, *in* Rhoden, H.N., Steininger, R.C., and Vikre, P.G., eds., Geological Society of Nevada Symposium 2005: Window to the World, Reno, Nevada, May 2005, p. 563–627.

temperatures of ~250°C. Gains in S, P, Ag, As, Sb, Hg, Zn, H_2O and CO_2 and losses in Mg accompanied propylitic alteration.

Potassic alteration (adularia-chlorite-pyrite/marcasite-smectite/illite-quartz) forms haloes that extend up to 30 m from the main veins and faults, and exhibits further increases in replacement of wall rock minerals and veining. Below ~1770 m elevation, epidote and albite are present, indicating temperatures similar to those of intense propylitic alteration. Illite/sericite and kaolinite, along with feldspars rimmed with adularia are present less than 10 m from the main veins. Fe-rich chlorite accompanies illite below ~1670 m elevation. Potassically-altered wall rocks of the main veins locally exhibit silica flooding and comprise a narrow zone of silicic-potassic alteration adjacent to the main veins; this alteration temporally overlaps the initial stages of formation of the main veins. Potassic alteration produced gains in K, S, Se, P, Ag, As, Sb, Hg, W, and losses in Ca, Mg, and Cr in mafic rocks; gains in S, Ba, Mg, Mn, P, Se, Ag, Sb, Cu, W, Bi, and losses in Na, Fe, Zn in rhyolites; and gains in S, Al, Ti, Mg, P, Sr, Cr, S, Cu and W with variable losses of Fe, K, Na, and Ca in felsic volcaniclastic rocks. Cross-cutting veinlets suggest that weak propylitic to silicic-potassic alteration types reflect a temporal progression with the most pervasive, and highest temperatures of alteration coeval with the onset of the main-stage veins. Argillic alteration occurs in subsidiary faults and permeable volcaniclastic rocks, and commonly overprints earlier alteration. Both argillic and silicic alteration are common at shallow levels of the system (i.e., at the present-day surface).

The main veins formed in deep-seated faults during multiple episodes of hydrothermal upflow producing crustiform ore with alternating bands rich in silica, adularia, bladed calcite, selenides and sulfides. The principal metal-bearing phases include naumannite, pyrite, chalcopyrite, electrum, sphalerite, and galena. Boiling textures are present over almost the entire vertical extent studied (~500 m). Pathfinder elements typical of epithermal systems, including Hg, As, and Sb, as well as K form haloes above ore-grade veins. Base metals show no significant changes over the vertical interval studied.

Key Words: Midas, alteration, geochemistry, paragenesis, epithermal gold-silver deposit, northern Nevada rift

INTRODUCTION

The Ken Snyder mine exploits a low-sulfidation epithermal vein system in the Midas district in north-central Nevada (Fig. 1). Commonly referred to as Midas, this gold deposit represents one of the more spectacular precious metal discoveries in the Great Basin made within the last decade (Goldstrand and Schmidt, 2000). It is the largest known precious metal deposit within the coeval suite of epithermal systems associated with the northern Nevada rift (NNR), and is the only vein system currently being mined. The deposit consists of a complex of Se-rich, high-grade Au-Ag veins or bonanzas, and contained a pre-mining total of approximately 3 Moz Au and 35 Moz Ag (0.25 oz/t or 8.5 g/t Au cutoff grade; R. Streiff, pers. commun., 2003; Leavitt et al., 2004). This deposit has renewed interest in exploration for bonanza-type deposits within the Great Basin, and epitomizes a precious metal target type that is the objective of numerous exploration programs throughout the world.

$^{40}Ar/^{39}Ar$ dates of volcanic rocks and quartz-adularia-precious metal veins constrain the timing and duration of Midas hydrothermal system, volcano-tectonic events, and mineralization (Leavitt et al., 2000; Leavitt et al., 2004). The 15.4 Ma age of veins at Midas is similar to ages of other precious metal-bearing epithermal systems along the NNR that range from 15.0 to15.6 Ma (John, 2001), as well as other epithermal systems associated with bimodal basalt-rhyolite volcanism that was widespread during this time in the northern Great Basin (Christiansen and Yeats, 1992; Fig. 1a). The Midas hydrothermal system developed during waning mafic volcanism, and was synchronous with rhyolite magmatism, local uplift, and faulting (Leavitt et al., 2004).

Exploration for low-sulfidation epithermal deposits such as Midas is often hampered by an inability to recognize surface or distal expressions of the hydrothermal system. Despite the presence of historic prospects and workings developed along relatively shallow portions of precious metal-bearing veins scattered throughout the mining district of Midas, and numerous drilling programs conducted within the last 20 years (LaPointe et al., 1991), the high-grade bonanza veins remained concealed until their discovery through a drilling program conducted by Ken Snyder in 1994 (Goldstrand and Schmidt, 2000).

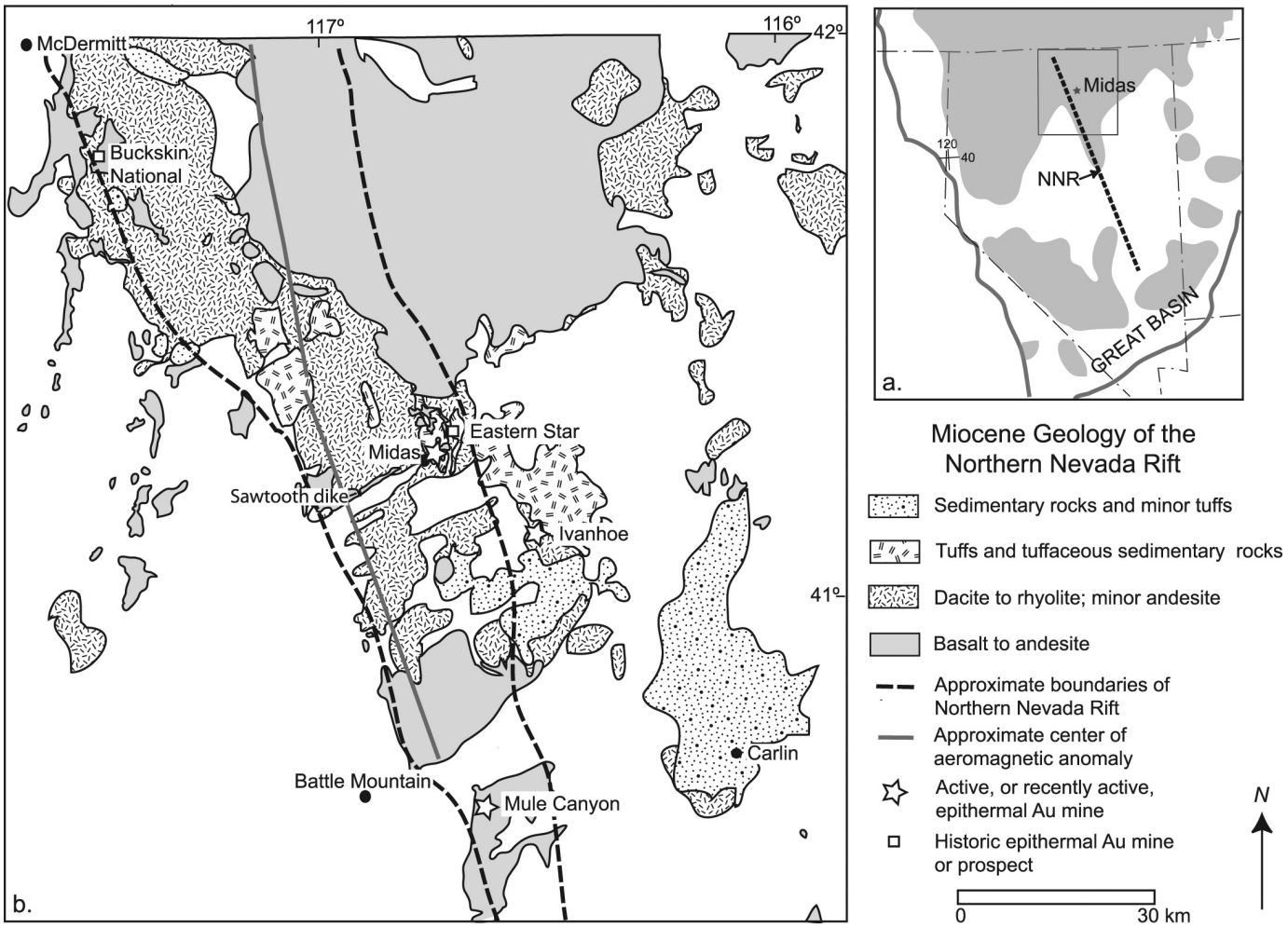

Figure 1. Location and general geology of the northern Nevada rift (NNR). a) Bimodal basalt-rhyolite assemblage (shaded) and axis of NNR. Modified from Christiansen and Yeats (1992), Ludington et al. (1996), and John (2001). b) Approximate locations of volcanic-hosted, low-sulfidation epithermal precious metal occurrences associated with the NNR. Modified from Stewart and Carlson (1976) and John and Wallace (2000).

Extensive vertical and lateral exposures of the Midas hydrothermal system from very near the paleosurface to depth include surface outcrops, drill core, and underground workings. Such three-dimensional access has provided a unique opportunity to study a low-sulfidation hydrothermal system in detail over 2500 vertical ft (760 m). To understand the evolution of the Midas hydrothermal system, research efforts have focused on several aspects of the deposit, described herein, including:

1. temporal and spatial variations in alteration mineralogy and geochemistry;
2. the relationship between hydrothermal alteration and main-stage vein formation;
3. identification of pathways of hydrothermal fluid flow, and possible sources of components.

Prior to this study no detailed or systematic characterization of alteration, geochemistry, and paragenesis of the Midas deposit had been carried out. General characteristics of alteration associated with the main productive veins at the Ken Snyder Mine have been described in several papers written soon after discovery of the deposit (Casteel et al., 1999; Goldstrand and Schmidt, 2000). Preliminary results of this study have been described in several abstracts (Leavitt et al., 2000; Leavitt, 2001; Leavitt, 2002). In this paper, detailed observations are developed into a model of the evolution of the system. Ultimately, these will lead to an improved understanding of the genesis of low-sulfidation systems in continental rift settings. A practical byproduct of this research is knowledge that may enhance exploration efficiencies in the Great Basin and similar settings worldwide.

GEOLOGIC SETTING

The Midas deposit is located on the east side of the NNR, a continental rift feature that extends from the Oregon border southeast through central Nevada (Fig. 1; Zoback and Thompson, 1978; Stewart and Carlson, 1976). The NNR and subparal-

lel lineaments formed during middle Miocene crustal extension and concurrent basalt-rhyolite bimodal magmatism. The lineaments are defined by aeromagnetic anomalies that locally correspond to alignments of volcanic vents, intrusions, fossil geothermal systems, and grabens (Zoback and Thompson, 1978; Blakley and Jachens, 1991; Zoback et al., 1994; John and Wallace, 2000; Ponce and Glen, 2002; Glen and Ponce, 2002). The Midas deposit is hosted by a bimodal basalt-rhyolite sequence of volcanic and volcaniclastic rocks in the southern Snowstorm Mountains. Dissection of the volcanic pile by normal faulting along the northern margin of the Midas trough, an E-NE striking graben that formed in late Miocene time, increased exposure of deeper levels of the Miocene volcanic rocks that host the deposit (Goldstrand and Schmidt, 2000; Wallace, 2003). The depth to pre-Tertiary basement is unknown but exceeds 1.5 km as determined by drilling (Leavitt et al., 2004). Relatively unaltered tuffs of mid-Miocene age overlie the uppermost portions of the hydrothermal system. Precious metal-bearing banded quartz-adularia-calcite veins are hosted by steeply-dipping, N- to NW-striking faults that exhibit significant normal offsets with a minor oblique component (Goldstrand and Schmidt, 2000; Leavitt et al., 2004).

A generalized stratigraphic column of the Midas area is shown in Figure 2, and includes $^{40}Ar/^{39}Ar$ dates reported by Leavitt et al. (2004). Figures 3 and 4 show the distribution of rock types in the vicinity of the Ken Snyder mine. Rhyolite ash-flow tuffs, flows, and volcaniclastic sediments of the lower tuff (Tlt), June Belle (Tjb), Elko Prince (Tep) and Esmeralda (Tes) formations (informal names) host ore-grade veins. Basalt and basaltic andesite dikes, sills, and flows (Tbg) that intrude and

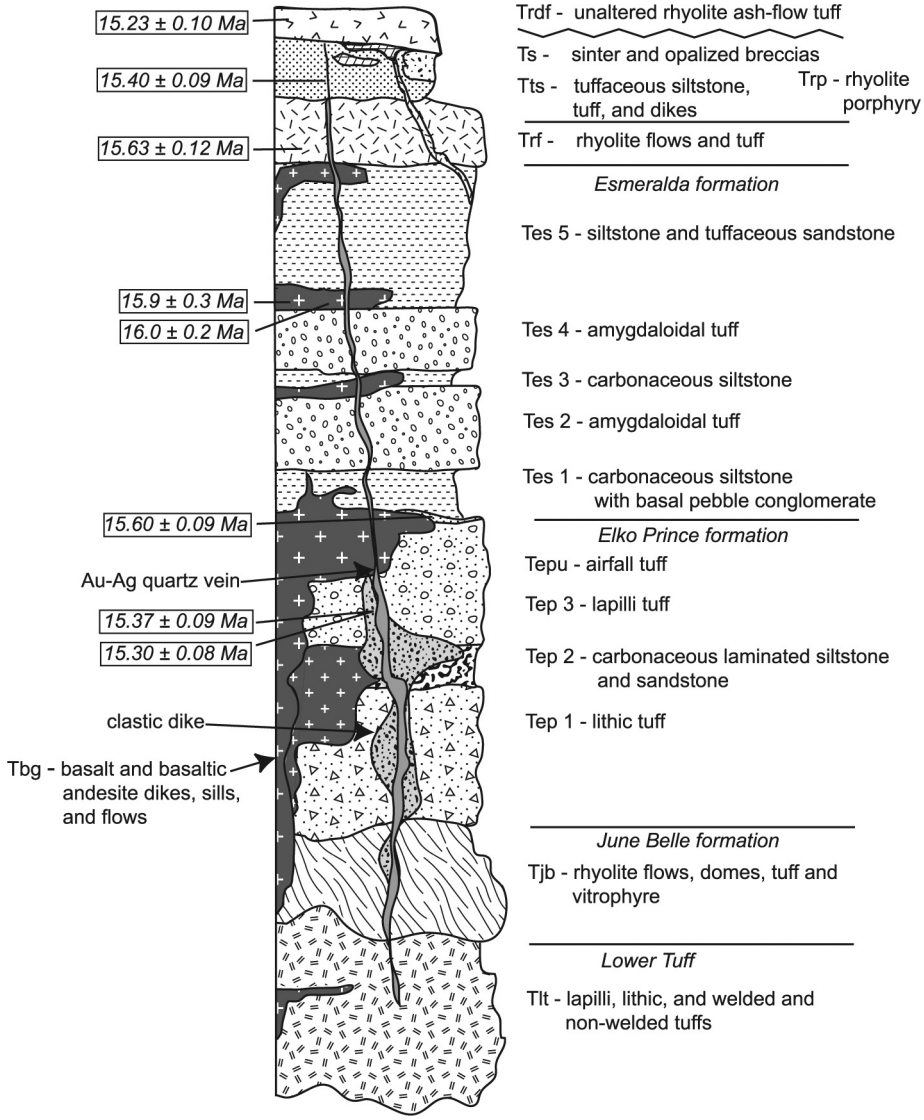

Figure 2. Generalized stratigraphic section of the Midas deposit. Geology modified from Goldstrand and Schmidt (2000). Relative locations of, and dates from geochronology samples shown.

interfinger with the host rock units are hydrothermally altered and contain minor amounts of precious and base metals, but generally do not host ore-grade veins (Goldstrand and Schmidt, 2000). Overlying flows of the red rhyolite (Trf; older than the main mineralizing event), and lacustrine sediments, tuffs (Tts), and rhyolite dikes (Tri; pre- to syn-mineralization) are locally significantly hydrothermally altered (Fig. 2). However, these upper units are not known to host significant quantities of precious metals (Leavitt et al., 2004). Approximately 10 km east of the Ken Snyder mine, a porphyritic rhyolite (Trp), thought to be correlative with rhyolite of the Sawtooth dike (Trpoi of Wallace, 1993; Leavitt et al., 2004), is altered and locally hosts

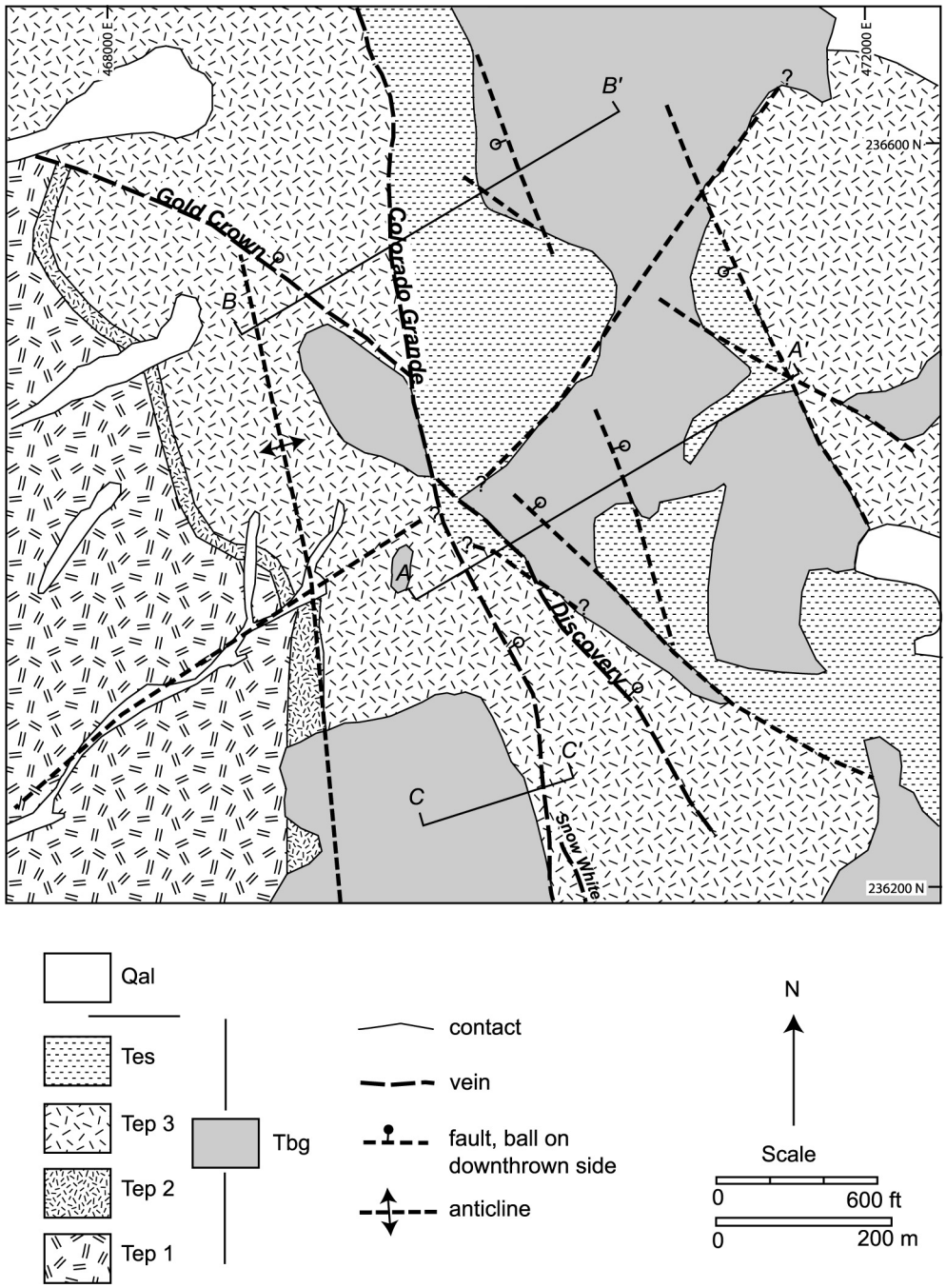

Figure 3. Geology of the Ken Snyder mine area, Midas district. Geology modified from Goldstrand and Schmidt (2000), and unpublished mapping by K. Snyder (1997), P. Goldstrand (2001), D. Rhys (2002), and E. Leavitt. Explanation of units as in Figure 2. Locations of NE-SW cross sections, A–A′ (Fig. 4a), and B–B′ (Fig. 4b) and C–C′ geochemical study shown.

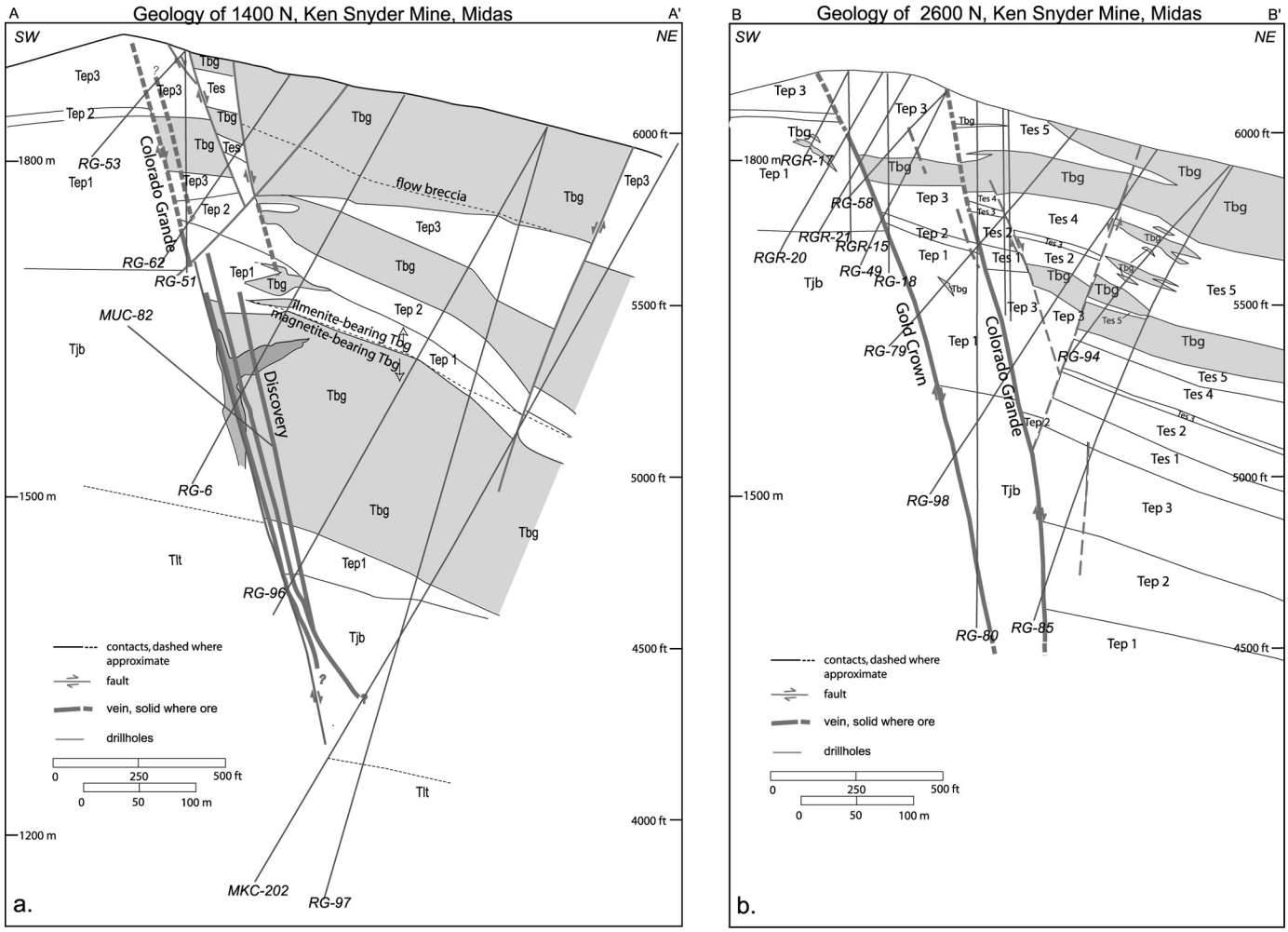

Figure 4. Geologic cross-sections approximately perpendicular to the main veins at the Ken Snyder mine including: a) 1400 N, and b) 2600 N. Geology modified from Goldstrand and Schmidt (2000). See Figure 2 for explanation of units, and Figure 3 for locations of sections.

cinnabar veinlets and old mercury workings (LaPointe et al., 1991). Stratigraphic relations suggest that the rhyolite porphyry (Trp) is similar in age to the lacustrine sediments and tuffs of Tts. A $^{40}Ar/^{39}Ar$ date of the Sawtooth dike is identical to that of high-grade veins at Midas. Unaltered rhyolite tuffs and vitrophyres (Trdf), which unconformably overlie opalized sediments of Tts, cap the hydrothermal alteration and are only slightly younger than mineralization (Fig. 2; Leavitt et al., 2004).

STRATIGRAPHIC UNITS

Hand specimen and petrographic descriptions of the least altered examples of the rock units are summarized in Table 1. Rhyolites that pre-date mineralization contain up to 10 volume percent phenocrysts of sanidine, lesser plagioclase, and minor ferromagnesian and opaque minerals in microcrystalline to cryptocrystalline groundmasses and matrices. Sanidines in the lower tuff and June Belle formation (Tlt and Tjb) are altered and exhibit mottled extinction typical of adularization (Henry et al., 1997). Sanidines in volcaniclastic rocks of the Elko Prince and Esmeralda formations (Tep and Tes) are unaltered unless adjacent to the main veins. Rhyolites that are syn- to post-mineralization (e.g., Trp) contain up to 20 volume percent phenocrysts of quartz and 5 to 10 volume percent sanidine. Pre-mineralization basalts and basaltic andesites are medium- to coarse-grained with up to 60 volume percent plagioclase and lesser amounts of olivine and pyroxene. Magnetite replaces ilmenite as the dominant oxide below approximately the 5000 ft level (~1520 m) in the 1400 N section (Fig. 4a). Further north magnetite appears at shallower levels, or the ~5850 ft level (1780 m) in the 2600 N section (Fig. 4b), and a change to ilmenite with decreasing depth is less well-defined. Very narrow dikes of ilmenite-bearing basalt locally intrude magnetite-rich basalt.

Major and trace element geochemical analyses of the least altered samples of volcanic rocks from the Midas area demonstrate the bimodal basalt-rhyolite nature of the volcanic sequence (see Appendix A for geochemical analyses). In a plot of total

TABLE 1. CHARACTERISTICS OF GEOLOGIC UNITS IN THE MIDAS AREA

Unit	Rock Type(s)	Phenocrysts, Crystals, or Clasts	Groundmass or Matrix	Accessory Minerals
Trdf	rhyolite ash-flow tuffs; vitrophyric to crystal-rich, and lithophysal	30–40% shards, 0.05–0.5 mm; 10–15% san, 0.2–1.0 mm; 1% plg, 0.5 mm; 1–2% pyx, 0.25 mm; rounded clasts of chal-zir-plg-pyx, 0.5–1.0 mm, mafic lapilli, and black glass	glassy to cryptocrystalline	1–2% hm, 1% lx, tr zir, all 0.05–0.1 mm
Trp	rhyolite porphyry	5–10% san, 3–10 mm; 15–20% qz, 0.5–1.0 mm	glassy, spherulitic, and microcrystalline qz, kf	1% opaques (ru, lx); tr zir
Tri	flow-banded, glassy and spherulitic rhyolite dikes	2–3% san, 0.5–2 mm; ± 1% plg, 0.5–2 mm	glassy, spherulitic, to cryptocrystalline, disseminated lx, hm, py, tr cp	tr zir, 0.1 mm; tr ru
Tts	interbedded vitric and lithic tuffs, siltstones, vent and tuff breccias, and opalized lacustrine sediments	tuff—50% shards, 0.5–1 mm; 1–10% san, 1.0–2.0 mm; ± 1% qz, 1–2 mm	glassy, axiolitic, cryptocrystalline	2–3% lx, 0.1 mm; 1–2% femags
Trf	red-brown glassy, massive, resistant to platy porphyritic rhyolite flows	3–5% san, 0.5–2 mm, euhedral, 3 mm, anhedral; ± 1–2% qz, 0.5–1 mm; ± <1% plg, 1–3 mm	glassy, spherulitic, axiolitic, to cryptocrystalline with qz±chal-hm-filled laminations	1–2% opaques (ilm, hm, lx), 0.01–0.1 mm; tr zir
Tes	amygdaloidal tuffs, sandy to carbonaceous siltstones, and basal conglomerates	tuff—1–30% plg, 0.1–0.5 mm; ± 1%–5% san, 0.1–0.3 mm; 1–3% femgs, 0.05–0.1 mm; = 10% lap; ± 1–2% lithic fragments, 1–10 mm	micro- to cryptocrystalline; devitrified, spherulitic	± 1–2% ilm/mt, 0.01–0.05mm; tr zir, 0.05–0.1mm
		siltstone—1% san, 1% plg, 1–2% (both subangular); 1–3% femgs (pyx); = 3% carbon fragments	very fine-grained qz, fsp, 0.01–0.05 mm; ± shards,	
Tbg	basalt and basaltic andesite to diabase sills, dikes, and flows	35–65% plg (lab to olig), 0.1–3 mm; 10–20% pyx (hyp, aug), 2–5 mm; 1–5% ol, 0.1–1mm	very fine-grained to glassy; intergranular, intersertal, to hypidiomorphic groundmass	1–10% ilm/mt, 0.05–0.5 mm; ± 1% py, 0.001–.01 mm; ± 1% pyr, 0.5–1 mm; tr cp;
Tep	rhyolite lithic, lapilli, and vitric tuffs; interbedded carbonaceous siltstones	tuff—1–10 % san, 0.1–3.0 mm; 1–10% plg, 0.1–2.0 mm; <1–3% femg; 1–70 % lith/lap/pum, 1–10 mm	microcrystalline to very fine-grained qz, kf; devitrified, locally spherulitic	±1% ilm/mt; ± tr ru, mon
Tjb	rhyolite tuffs, flows, and intrusions	5–10% san, 1–3 mm;1–3% plg, 0.5–2 mm; lithics, lapilli, pumice	eutaxitic; flow-banding; felsitic to spherulitic	± 1% femgs, 0.1 mm; ± 1% ilm
Tlt	rhyolite tuffs	5–10% san, 0.3–3 mm; = 1% plg, 1–3mm; 1–2% femgs, 1–2mm	glassy, microcrystalline devitrified; minor welding	3–5 % femgs; 1–3% ox; tr zir

Abbreviations: aug—augite, chal—chalcedony, cp—chalcopyrite, femgs—ferromagnesian minerals, hm—hematite, hyp—hypersthene, ilm—ilmenite, kf—potassium feldspar, lx—leucoxene, mon—monazite, mt—magnetite, ol—olivine, plg—plagioclase, py—pyrite, pyrrhotite—pyr, pyx—pyroxene, qz—quartz, san—sanidine, ru—rutile, zir—zircon; tr—trace

alkalis vs. silica (Fig. 5a) compositions of pre-, syn-, and post-mineralization rhyolites are indistinguishable. Compositions of pre-mineralization basalts lie within or straddle the tholeiitic and calc-alkaline fields (Fig. 5b). Basaltic andesites sampled from relatively high in the stratigraphic section lie well within the calc-alkaline field. The compositionally least evolved basalt overlies post-mineralization rhyolite porphyries in the Midas trough approximately 15 km to the southwest of Midas (Wallace, 1993). A K-Ar date of this unit (6.4 ± 2.3 Ma; Wallace et al., 1990) shows that it is significantly younger than the Midas deposit. Although the number of analyses of unaltered rocks is limited, the general trend of tholeiitic to calc-alkaline compositions prior to ~15.5 Ma, apparent increase in silicic volcanism by 15.4 Ma, and return to more primitive basalts during waning activity up to 10 m.y. later is consistent with trends observed in coeval volcanic sequences elsewhere within the Midas trough area and Oregon Plateau (e.g., Carlson and Hart, 1987; Hooper et al., 2002).

Faulting has deformed both pre- and post-mineralization rocks in the Midas district. The predominant fault orientations are NS to N30°W, N50°W to N60°W, and EW to ENE (Wallace, 1993; Blair, 1991; Casteel et al., 1999; Goldstrand and Schmidt, 2000; Fig. 3). The main productive gold-quartz veins, including the Colorado Grande (CG) and Gold Crown (GC), are hosted by normal faults with a component of oblique movement. The CG vein formed in a laterally and vertically persistent, NS- to N30°W-striking, steeply NE-dipping normal fault (Goldstrand and Schmidt, 2000). As much as 1000 ft (335 m) of normal displacement occurred along this fault prior to mineralization, with little additional displacement after formation of the veins (Goldstrand and Schmidt, 2000). The GC vein formed in a steeply northeast-dipping, N50° to 60°W-striking fault that splays into the footwall of the Colorado Grande fault. Other veins, including the Snow White and Discovery, developed in N20°- to N30° W-striking, steeply NE-dipping faults that splay southeastward from the southern portion of the CG vein (Goldstrand and Schmidt, 2000). East- to northeast-striking faults were active prior to and following mineralization and do not host significant quantities of precious metals (Goldstrand and Schmidt, 2000). Host rocks dip gently away from a NNW-trending anticline axis parallel to, and approximately 600 ft (180 m) west of, the Colorado Grande vein (Goldstrand and Schmidt, 2000; Fig. 3). Post-mineralization rhyolites appear to terminate at the flanks of the shallow anticline (Wallace, 1993).

METHODS OF STUDY

Detailed mapping and sampling of surface, core, and underground exposures was carried out in the Ken Snyder mine area, and reconnaissance level work was carried out in additional parts of the Midas district. Petrographic (transmitted and reflected), cathodoluminescence (CL), X-ray diffraction (XRD), Portable Infrared Mineral Analyzer (PIMA), scanning electron microscope (SEM), and electron microprobe (EMP) analyses were carried out on selected samples from surface, underground, and core. Surface mapping and logging and sampling of drill core were focused on the central portion of the deposit. Results of previous work including geologic mapping (P.M. Goldstrand, unpublished mapping, 1999; Goldstrand and Schmidt, 2000; D.A. Rhys, unpublished report, 2002; S. Garwin, unpublished mapping, 2002), drill logs from Franco-Nevada geologists, and unpublished petrographic work (unpublished reports, L.T. Larson, 1995, 1996, 1997, 1998) were incorporated into the compilation of geology, petrography, and geochemical data. A geologic map, interpretive geologic cross-

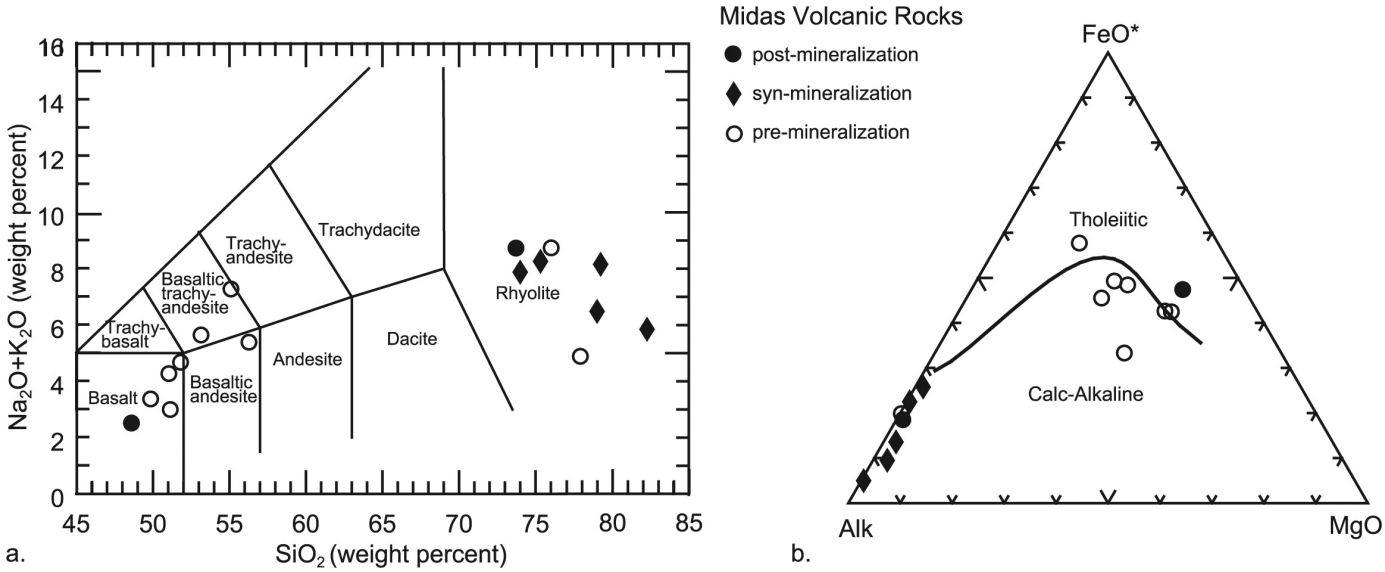

Figure 5. Plots of major oxides from whole-rock analyses including: a) total alkali-silica (TAS) diagram for least altered volcanic rocks at Midas. Rock classification from IUGS (Le Bas et al., 1986); b) AFM diagram for least altered volcanic rocks at Midas. Compositional fields from Irvine and Barager (1971). *Total iron as FeO. Silica-rich samples (>77% SiO_2) may reflect weak to moderate alteration.

sections for 1400 N and 2600 N, and alteration overlays are presented in Figures 3, 4, 6, and 7, and are discussed in more detail in the following sections.

Approximately 30 samples from core, surface, and underground were characterized using XRD analysis. Samples were ground with a mortar and pestle and a slurry of the powder was deposited on glass slides and dried, producing an oriented sample. Samples were analyzed using CuK_a radiation on a Philips automated XRD. Materials Data, Inc. (MDI) Datascan software was utilized to acquire data, and MDI Jade software that includes the ICDD-PDF minerals database was utilized to process data. Clay samples were run dry and glycolated with ethylene glycol. Representative analyses of clays are included in Appendix B.

Trace element and fire assay analyses of samples of core and reverse circulation holes from the 1400 N and 2600 N sections were provided by Franco-Nevada. Samples were generally continuous, and intervals ranged from less than 1 ft (~0.3 m) in areas of veining to a maximum of 10 ft (~3 m). Trace element analyses were carried out using standard aqua regia digestion and inductively coupled plasma (ICP) techniques. Fire assays for precious metals were carried out for high-grade samples.

Additional geochemical analyses of selected samples of core from 1400 N, and surface and underground samples were carried out for this study. Major oxides and rare earth elements were determined using ICP atomic emission spectroscopy (AES) and mass spectrometry (MS) techniques following a metaborate fusion. Most trace elements were determined fol-

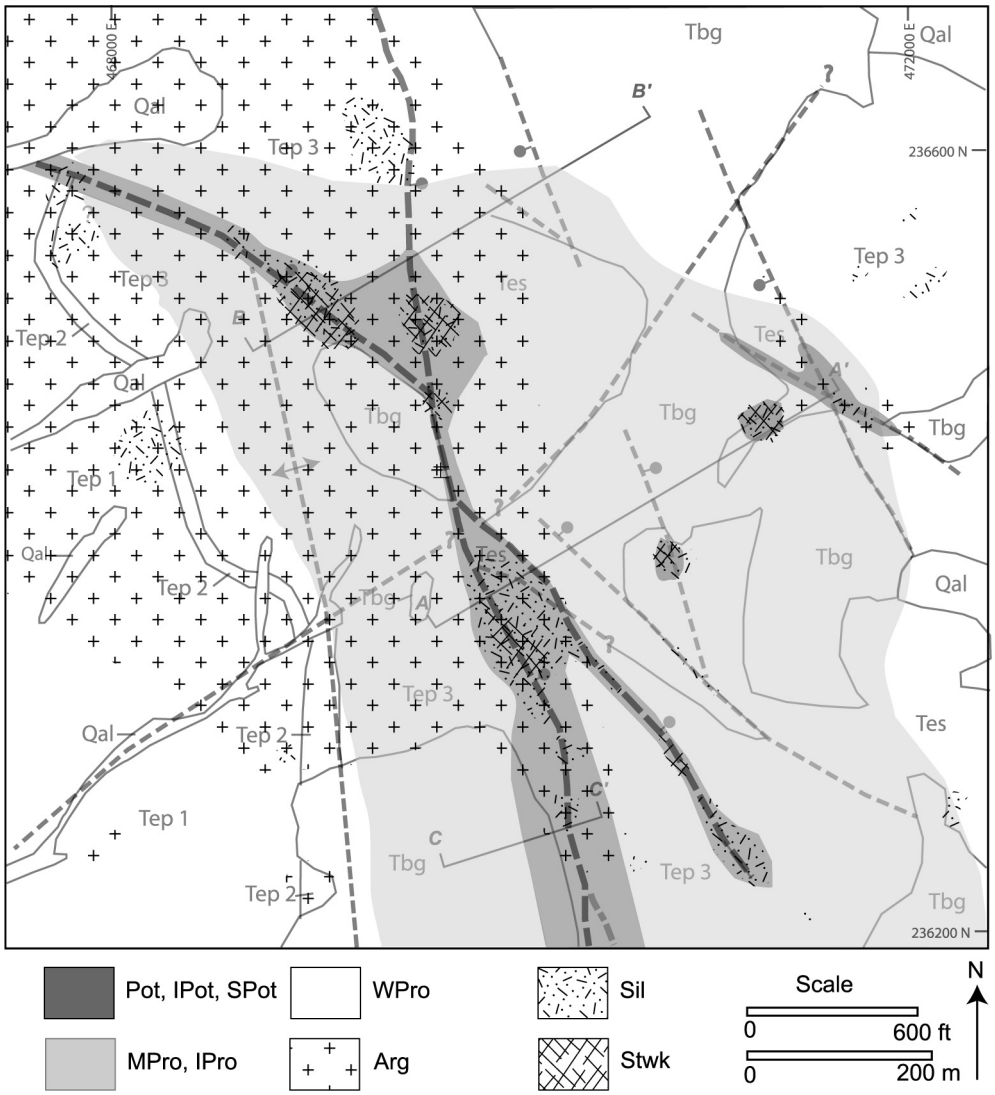

Figure 6. Interpretative alteration map of the Ken Snyder mine area. Midas district. Pot—potassic; IPot—intense potassic; SPot—silicic potassic; M Pro—moderate propylitic; IPro—intense propylitic; WPro—weak propylitic; Arg—argillic; Sil—silicic; Stwk—stockwork. Geology as in Figure 3. See Table 2 and text for descriptions of alteration types.

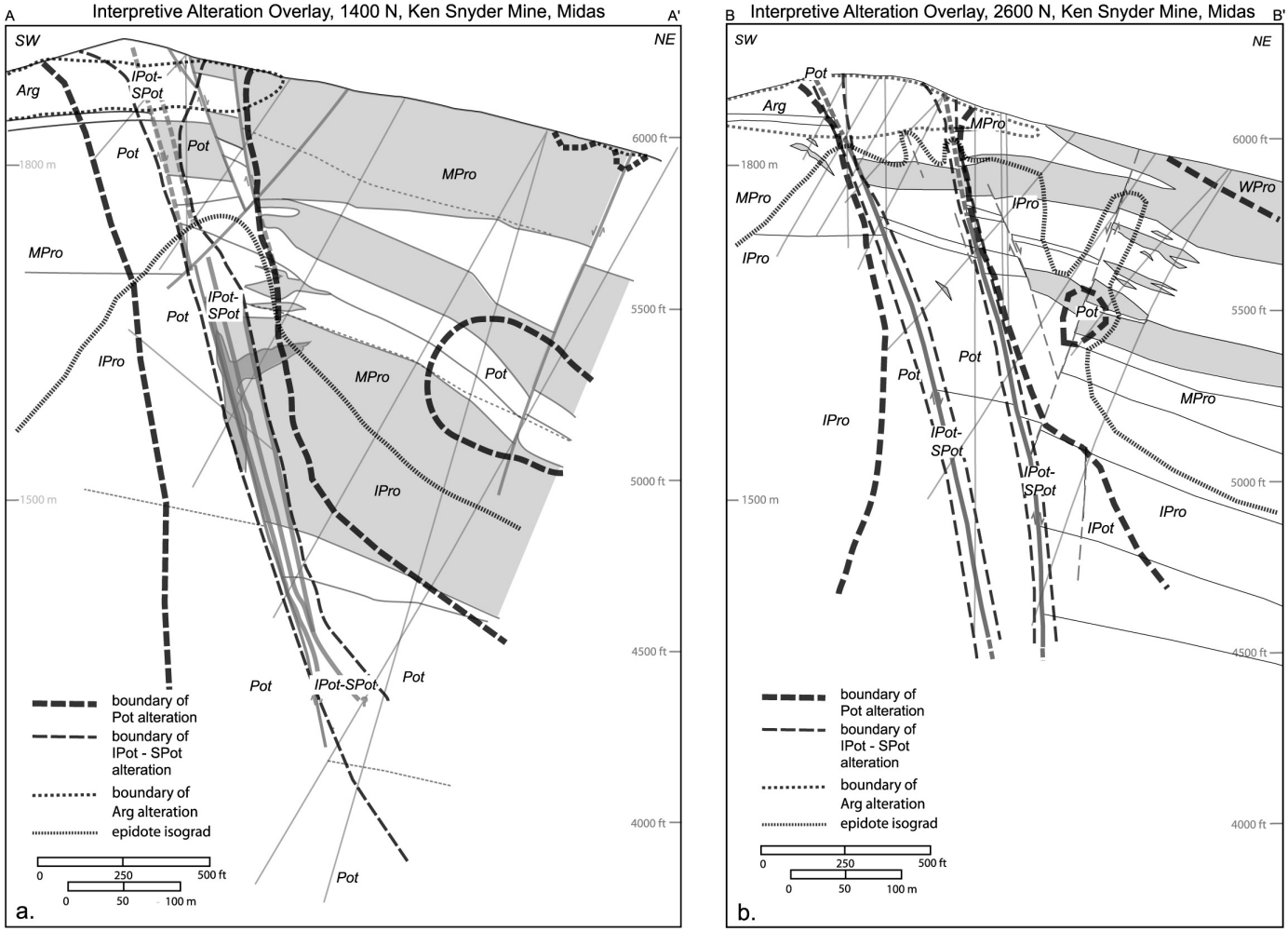

Figure 7. Interpretative alteration overlays for cross-sections of the Ken Snyder mine including: a) 1400 N, and b) 2600 N. See Figure 6 for explanation of alteration types and locations of sections, and Table 2 and text for descriptions of alteration types. Shaded areas are mafic rocks.

lowing nearly complete tri-acid digestion (HF-HNO_3–$HClO_4$, and HCl leach, a technique developed for increased sensitivity of trace elements), and ICP-MS. Selenium was determined with $HCl/KClO_3$ digestion, organic extraction and atomic absorption (AA). Hg was determined with aqua regia digestion and cold vapor AA. Sulfur and total carbon were determined with the Leco furnace (Appendix A).

HYDROTHERMAL ALTERATION

Alteration mineral assemblages exhibit a subtle though distinctive zonation centered on the main veins. With the exception of argillic and silicic types, alteration is zoned around the main veins and progresses from propylitic to potassic assemblages as the veins are approached (Figs. 6, 7, and 8). Weak propylitic alteration, only identified in mafic rocks, is widespread and likely deuteric. Closer to the veins moderate propylitic alteration is characterized by increases in fracturing and replacement of wall rock minerals, and abundances of chlorite and pyrite. With increasing depth and proximity to the veins, intense propylitic alteration includes minerals formed at higher temperatures. Within 30 m of the veins, and in subsidiary faults and breccia zones, potassic alteration contains intensely replaced and veined wall rocks, and is zoned from potassic to intense potassic to silicic-potassic zones towards the veins. Silicic alteration is less well understood, but is located above the level of ore and close to the present-day surface. Argillic alteration is most strongly developed in permeable volcaniclastic rhyolites of the Elko Prince and Esmeralda formations (Tep and Tes) along faults and at shallower levels of the deposit, and appears to overprint earlier types of alteration. The paragenesis of alteration minerals and main stage veins is summarized in Figure 9.

PETROGRAPHY OF ALTERATION TYPES

Alteration types were characterized for three dominant lithologies including: welded rhyolite tuffs, flows and intrusions of the lower tuff (Tlt), and June Bell formation (Tjb); per-

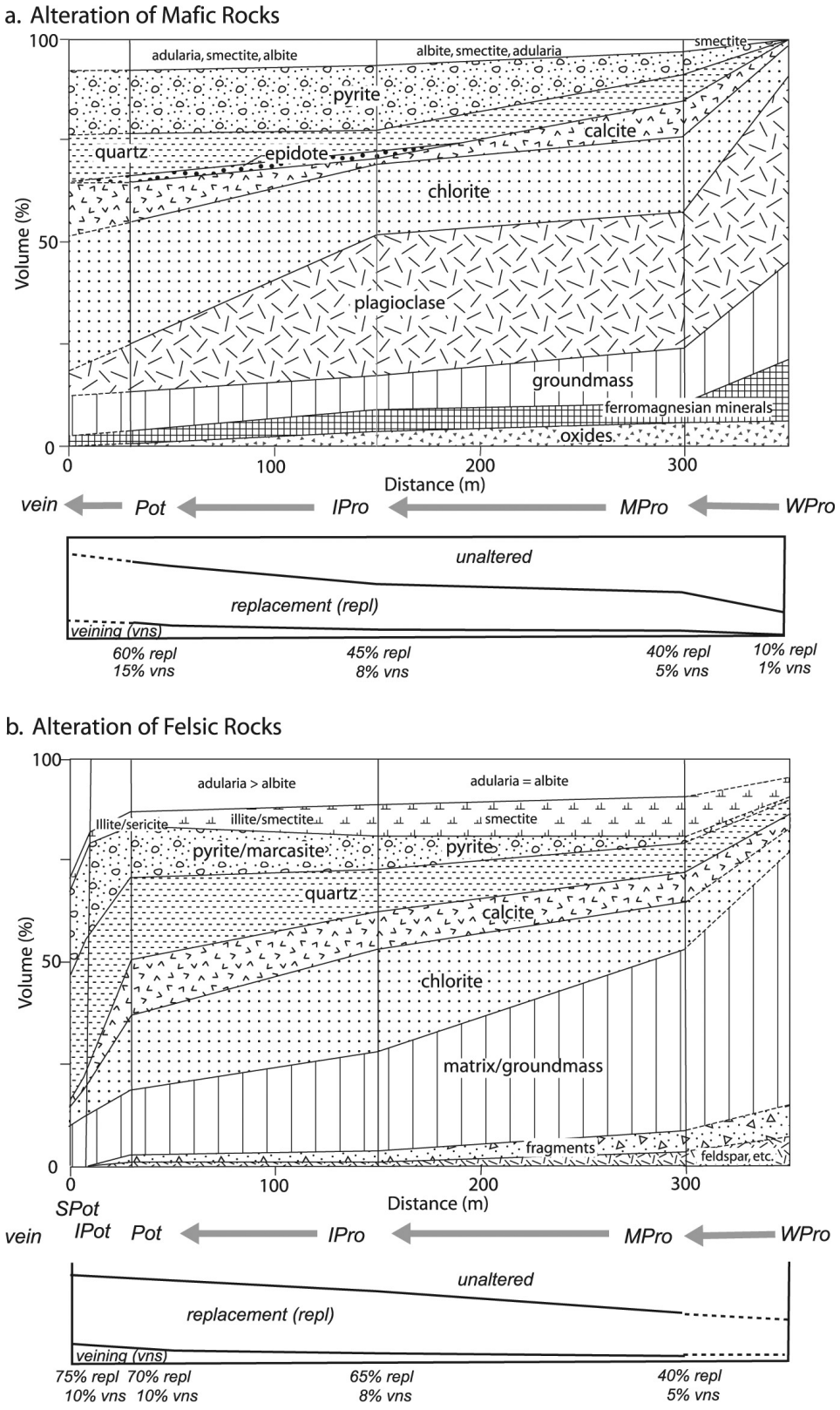

Figure 8. Schematic representation of progressive alteration of a) mafic rocks, and b) felsic rocks. Alteration types shown with spatial reference to main gold veins. Based on petrographic analysis of thin-section samples. Abbreviations as in Figure 6. See Table 2 and text for more detailed descriptions of alteration.

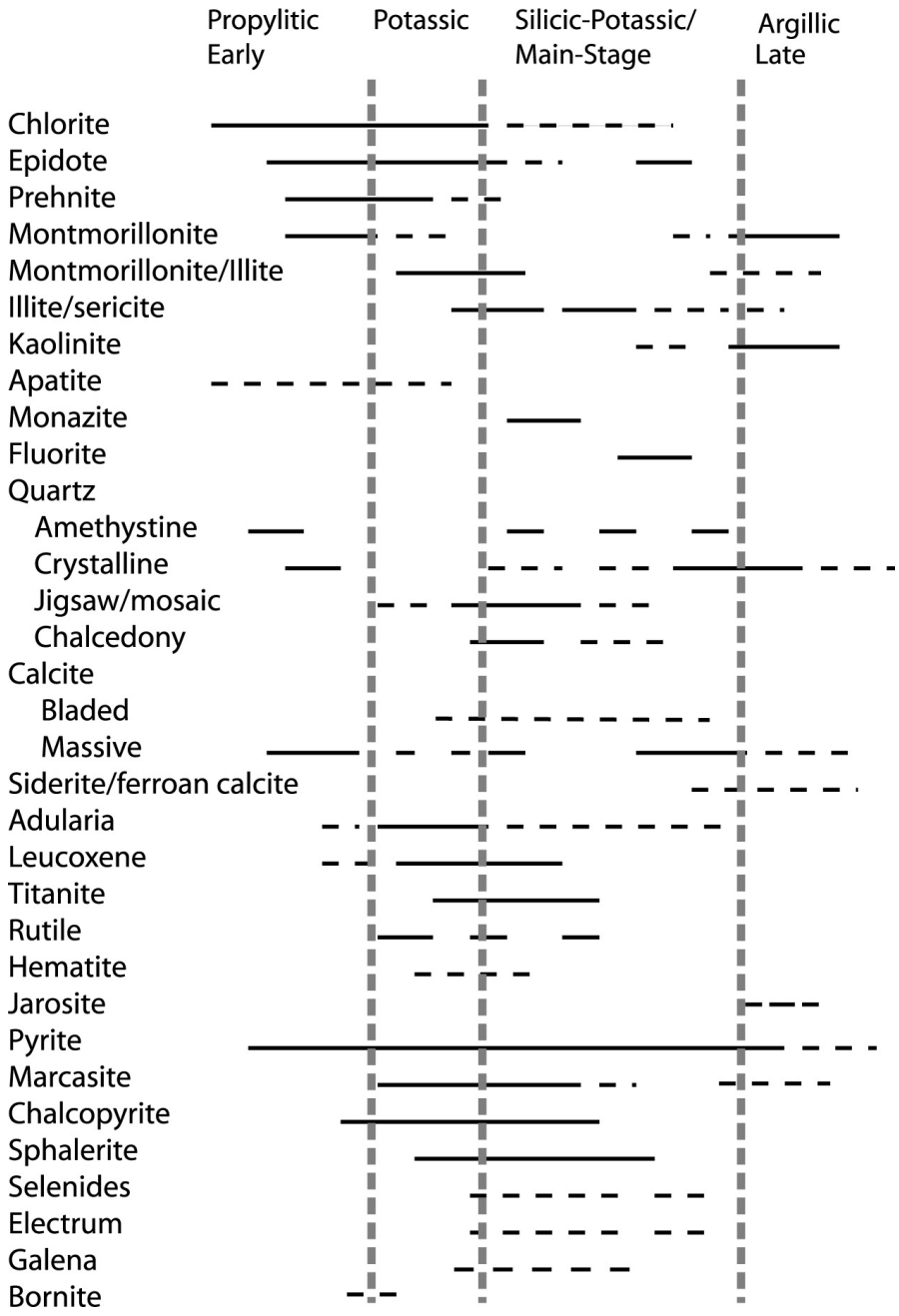

Figure 9. Paragenetic sequence of alteration types, and alteration and vein-forming minerals at the Ken Snyder mine. Main-stage mineral sequences generalized.

meable felsic volcaniclastic tuffs and sediments of the Elko Prince (Tep) and Esmeralda formations (Tes); and basalt and basaltic andesite flows, sills, and dikes (Tbg). Petrographic classification of alteration types was based upon the volume percent of wall rock mineral replacement and veining, and secondary mineral associations. These data were compared to geochemical analyses (Appendix A). Characteristics of the main alteration types are summarized in Table 2a and 2b, and Figures 8 and 9, and described below.

Weak propylitic—chlorite-calcite

Weak propylitic alteration of mafic rocks (Tbg) is present between 650 ft (~200 m) to several km from the veins, and above the 5575 ft level (1700 m) elevation (Figs. 6 and 7). Propylitized rocks are 10 to 35 volume percent replaced by alteration minerals; veins and fractures comprise an additional 1 to 5 volume percent of the alteration. Plagioclase is unaltered to weakly replaced by calcite and montmorillonite. Ferromag-

TABLE 2A. CHARACTERISTICS OF PROPYLITIC ALTERATION, KEN SNYDER MINE, MIDAS, NEVADA.

	Weak Propylitic/Chloritic (WPro)	Moderate Propylitic (MPro)	Intense Propylitic (IPro)
Mafic rocks			
Distribution	> 200 m from main veins; ~deuteric; above ~1700m	>125 m from main veins; above ~1780 m (5850′)	>25 m from main veins; distal from veins below ~1780 m (5850′); proximal, 1830 m (~6000′)
Alteration association	*chlorite-calcite±smectite±pyrite±* Fe-oxides	*chlorite-calcite-pyrite-smectite* albite±quartz±leucoxene±Fe-oxides	*chlorite-pyrite-epidote-smectite* albite-leucoxene±prehnite±calcite±titanite± chalcopyrite±apatite
Alteration /Textures	10–35% replaced; 1–5% veined	15–60% replaced; 1–10% veined	35–55% replaced; 2–15% veined
Plagioclase	fresh to partially replaced by calcite, smectite*	partially replaced by smectite, chlorite, calcite, and minor albite	partially replaced by chlorite, epidote, albite, and minor smectite, calcite ± prehnite, adularia
Ferromagnesian (olivine, pyroxene)	fresh to partially replaced by chlorite (brown), Fe-oxides, calcite, iddingsite (olivine); trace of sulfides/pyrite	partially replaced by chlorite and minor pyrite, iddingsite, calcite, and Fe-oxides	partially to completely replaced by chlorite ± pyrite, chalcopyrite, calcite
Oxides (magnetite, ilmenite)	fresh	weakly replaced by pyrite and leucoxene	partially to completely replaced by leucoxene ± titanite, pyrite; sulfidation of magnetite next to veinlets/structures
Groundmass	partially replaced by chlorite (brown), traces of leucoxene	partially to strongly replaced by chlorite (brown to green), pyrite, calcite, and traces of chalcopyrite	partially to completely replaced by chlorite, and minor epidote (brown), quartz, pyrite, leucoxene ± chalcopyrite, sphalerite, apatite, titanite
Veins	narrow fractures with brown chlorite, minor quartz and calcite; shallow-dipping	brown chlorite cut by light-green chlorite+quartz±pyrite cut by calcite-smectite±pyrite; increase in pyrite w/structures	chlorite-quartz to calcite±epidote±chalcopyrite to calcite-pyrite
Felsic rocks			
Distribution		> 300 m from main veins; above ~1675 m (5500′)	> 60 m from main veins; < 1830 m (6000′)
Alteration association		*chlorite-smectite-calcite-pyrite* adularia-albite-quartz-leucoxene (argillic overprint common)	*chlorite-pyrite-epidote-smectite* quartz-adularia-albite-leucoxene±apatite
Alteration /Textures		30–40% replaced; 1–5% veined	60–80% replaced; 2–10% veined
Sanidine		nearly completely replaced by adularia, and minor quartz, chlorite	nearly completely replaced by adularia
Plagioclase		nearly completely replaced by albite and minor smectite, chlorite	partially to completely replaced by albite, epidote and minor smectite, apatite
Ferromagnesian		nearly completely replaced by pyrite and minor leucoxene	completely replaced by epidote
Lithic/lapilli/pumice		variably replaced by chlorite, pyrite, leucoxene	partially to completely replaced by quartz, chlorite, epidote, leucoxene, pyrite
Groundmass/matrix		partially replaced by chlorite, quartz, calcite and minor leucoxene, pyrite	partially to completely replaced by chlorite (green), epidote, quartz, smectite, leucoxene
Veins			quartz-calcite to quartz-adularia-pyrite-calcite

*smectite—mostly Ca-montmorillonite; minor apple-green nontronite/saponite in MPro

TABLE 2B. CHARACTERISTICS OF POTASSIC ALTERATION, KEN SNYDER MINE, MIDAS, NEVADA.

	Potassic (Pot)	Intense Potassic (IPot)	Silicic-Potassic (SPot)
Mafic rocks			
Distribution	<30 m from main veins; ~1525–1830 m (5000 to 6000′); also in subsidiary structures, permeable zones		0–15 m from main veins; ~1800 m (5900′) to 1900 m (surface)
Alteration association	chlorite-pyrite/marcasite-quartz-adularia-rite-		quartz-adularia-smectite/illite-chlo-
	smectite/illite-albite±calcite±epidote±leucoxené ±apatite±titanite±chalcopyrite±sphalerite±rutile		pyrite/marcasite-calcite±kaolinite
Alteration /Textures	30–95% replaced; 5–25% veins		60–70% replaced; 5% veined
Plagioclase	partially replaced by albite, chlorite, smectite, illite/smectite, epidote and minor adularia, quartz, apatite		partially replaced by calcite, chlorite/chamosite, smectite/illite
Ferromagnesian	partially to completely replaced by chlorite/chamosite, pyrite		completely replaced by chlorite/chamosite, calcite
Oxides	partially replaced by pyrite ± leucoxene		
Groundmass	partially replaced by chlorite, adularia, quartz, epidote, and minor pyrite, marcasite ± chalcopyrite, sphalerite, apatite, rutile, titanite		partially replaced by chlorite, smectite, calcite, quartz, adularia and minor kaolinite
Veins	chlorite-pyrite to quartz-adularia ± chalcopyrite		silica flooding
Felsic rocks			
Distribution	10–30 m from main veins; ~765 m (2500′) to surface	<10 m from main veins; ~1340 m (4400′) to surface	adjacent to main veins
Alteration association	adularia-chlorite-quartz-pyite/marcasite-smectite/illite-albite-leucoxene±chalcopyrite± sphalerite±titanite±apatite±kaolinite±rutile± epidote±Fe-oxides	quartz-illite/sericite-kaolinite-pyrite/marcasite-adularia-quartz±leucoxene±titanite±chalcopyrite± apatite±rutile±Fe-oxides	quartz-adularia-illite/smectite-pyrite/marcasite±chlorite±kaolinite± leucoxene±apatite±epidote± chalcopyrite±selenide
Alteration /Textures	50–90% replaced; 1–20% veined	60–90% replaced; 5–35% veined	80–90% replaced; 5–15% veined
Sanidine	partially to completely replaced by adularia and less quartz, chlorite (bright-green), illite/smectite, kaolinite ± epidote, apatite, rutile, titanite, Fe-oxides	nearly completely replaced by adularia, illite/sericite, quartz, kaolinite ± apatite, chlorite/chamosite (at depth); rimmed with adularia	nearly completely replaced by adularia, illite/smectite, kaolinite ± apatite, chlorite/chamosite (at depth)
Plagioclase	partially to completely replaced by adularia, albite ± chlorite, epidote, illite/smectite, quartz, Fe- and Ti-oxides, kaolinite	nearly completely replaced by adularia, albite, kaolinite ± quartz, illite/sericite, pyrite, epidote, chlorite/chamosite (at depth), leucoxene, apatite, titanite	completely replaced by smectite/illite, kaolinite ± quartz, adularia, apatite, leucoxene, epidote, chlorite
Ferromagnesian	completely replaced by chlorite and leucoxene	completely replaced by chlorite, if distinguishable	
Lithic/lapilli/pumice	partially to completely replaced by quartz, chlorite, leucoxene, pyrite	chlorite, marcasite/pyrite, hematite ± kaolinite, Fe-oxides	same as matrix
Groundmass/matrix	partially to completely replaced by quartz, adularia, calcite, chlorite, smectite/illite, leucoxene, pyrite, ± marcasite, chalcopyrite, apatite, titanite	nearly completely replaced by quartz, adularia, illite/smectite, kaolinite, marcasite ± leucoxene, rutile, titanite, chalcopyrite	nearly completely replaced by quartz, adularia ± kaolinite, chlorite, epidote, pyrite, marcasite, Fe-oxides, smectite
Veins	chlorite to pyrite/marcasite to quartz-adularia-sphalerite to quartz-hematite to chlorite to calcite-smectite	chlorite to quartz-pyrite±rutile to quartz-sphalerite± adularia to quartz-marcasite-illite-galena	chlorite to epidote-quartz ±calcite-pyrite-galena-chalcopyrite

*smectite—mostly Ca-montmorillonite

nesian minerals are relatively fresh to moderately altered to brown chlorite (clinochlore), iddingsite, minor calcite, and traces of pyrite. Oxides (magnetite and ilmenite) are generally unaltered. The groundmass contains minor brown chlorite and trace amounts of leucoxene. Sulfides, including pyrite, are rare. Veinlets and fractures with brown chlorite and minor quartz and calcite are typically shallow-dipping and cut by subsequent veinlets associated with more intense alteration (Fig. 9).

Moderate propylitic—chlorite-calcite-pyrite-smectite

Moderate propylitic alteration occurs between 65 ft (~20 m) and 1300 ft (~400 m) fro, the main veins, and above the 4800 ft level (~1460 m; Figs. 6 and 7). Compared to weak propylitic, moderate propylitic alteration is characterized by more intense replacement of phenocrysts and groundmass (up to 60 vol% in mafic; 40 vol% in felsic), increased veining (up to 10 vol% in mafic), and increased abundances of calcite, pyrite and clay (Fig. 8). Altered mafic rocks are greenish black to gray-green and contain shallow-dipping veinlets of chlorite cut by steeply-dipping veinlets of calcite with dark selvedges of chlorite± pyrite. Plagioclase is partially altered to Ca-montmorillonite, chlorite, calcite, and minor albite. Ferromagnesian minerals are replaced by chlorite, iddingsite, and minor calcite and pyrite. Oxides are weakly altered to leucoxene and pyrite. The groundmass is partially replaced by chlorite, calcite, pyrite, and traces of chalcopyrite. Minor apple-green nontronite is present along fractures above the 5800 ft level (1770 m). Pyrite is present as clots (≤2 mm) on chlorite-lined fractures and in veinlets that cut chlorite-lined fractures. The abundance of pyrite increases adjacent to structures and in receptive horizons such as magnetite-bearing basalts and carbonaceous sediments (e.g., Tep 2). In the latter rock type pyrite is concentrated along carbonaceous laminations and forms up to 20 volume percent of the rock. Cross-cutting veins and fractures show a temporal evolution from brown chlorite (of earlier weak propylitic) to light green chlorite-quartz±pyrite to calcite-smectite±pyrite (Fig. 9).

Felsic tuffs contain pale-green clasts in pale-green to gray-white matrices. Sanidines exhibit mottled extinction typical of adularization, and are partially replaced by quartz, rutile, leucoxene, and pyrite. Plagioclase is partially replaced by albite, Ca-montmorillonite, and minor apatite. Ferromagnesian minerals are nearly completely replaced by pyrite and minor leucoxene. The clasts and matrix are turbid and partially altered to chlorite, smectite, leucoxene, calcite, pyrite, and minor rutile, titanite and adularia; pyrite and chlorite are more abundant in clasts. Quartz and calcite veinlets are common.

Intense propylitic—chlorite-pyrite-epidote-smectite

Moderate propylitic alteration gives way to intense propylitic alteration with increasing depth, proximity to the main veins and subsidiary structures, and is marked by the appearance of epidote. Intense propylitic alteration is characterized by increased replacement (to 75 vol%) of host rock minerals, veining (up to 15 vol% in mafic rocks, and 10 vol% in felsic rocks), abundance of chlorite, leucoxene, quartz, and decreased abundance of calcite. In hand specimen, mafic rocks are medium to light gray and contain bleached and darkened veinlet selvedges, the former due to increased quartz and the latter due to increased chlorite and pyrite. Epidote occurs as a replacement of plagioclase, in veinlets, and in the groundmass (Figs. 8, and 10a–c). The crystallinity and green color of epidote intensify with depth. Plagioclase is turbid to cloudy and partially altered to chlorite, epidote, albite, lesser smectite, calcite, and variable amounts of prehnite and adularia. Ferromagnesian minerals are partially to completely altered to chlorite and variable amounts of calcite, pyrite, and chalcopyrite. Oxide minerals are partially to completely altered to leucoxene, pyrite, and titanite. The groundmass is altered to chlorite with minor brown epidote, quartz, pyrite, leucoxene±chalcopyrite±sphalerite±apatite± titanite. Pale green (Mg-rich) chlorite grades into bright green (Fe-rich) chlorite with increasing depth and proximity to the main veins. Replacement of magnetite by pyrite is present in selvedges of veinlets of quartz-chlorite±epidote±prehnite (Fig. 10e–f), and is most common in haloes surrounding the CG and subsidiary faults in the hanging wall. Veinlets demonstrate a temporal evolution from chlorite-quartz to prehnite± pyrite to calcite±epidote±adularia±chalcopyrite±pyrite±bornite to chlorite±quartz±illite (Fig. 9).

An epidote isograd (first appearance of epidote with depth) forms the boundary between moderate and intense propylitic alteration zones, and shallows adjacent to the veins. The shallowest part of the epidote isograd roughly coincides with the top of ore grades in the GC vein at the 6000 ft level (1830 m) in section 2600 N (Fig. 7b), and with the top of ore grades in the CG vein at the 5600 ft level (1700 m) in section 1400 N (Fig. 7a). The isograd dips to the south from section 2600 N to 1400 N.

Volcaniclastic rhyolites of the Elko Prince and Esmeralda formations (Tep and Tes) contain increased abundances of veining, replacement, and secondary quartz and pyrite compared to moderate propylitic alteration. Feldspars (difficult to distinguish plagioclase from sanidine due to alteration) are replaced by albite and epidote, and sanidine is partially to nearly completely adularized. Ferromagnesian minerals are altered to pyrite. The matrix contains quartz, clay, adularia, and lesser pyrite, chlorite, iron oxides, leucoxene, rutile, and epidote. Cross-cutting veinlets show a temporal progression from calcite to quartz-adularia-pyrite/marcasite-calcite to quartz-illite-jarosite (Fig. 9).

Potassic—adularia-chlorite-pyrite/marcasite-smectite/illite-quartz

Potassic alteration forms a zone that extends up to 100 ft (~30 m) outwards from the main veins and is characterized by increased replacement (to 95 vol%) of host rock minerals and pyrite-quartz veining; increased abundances of marcasite (or

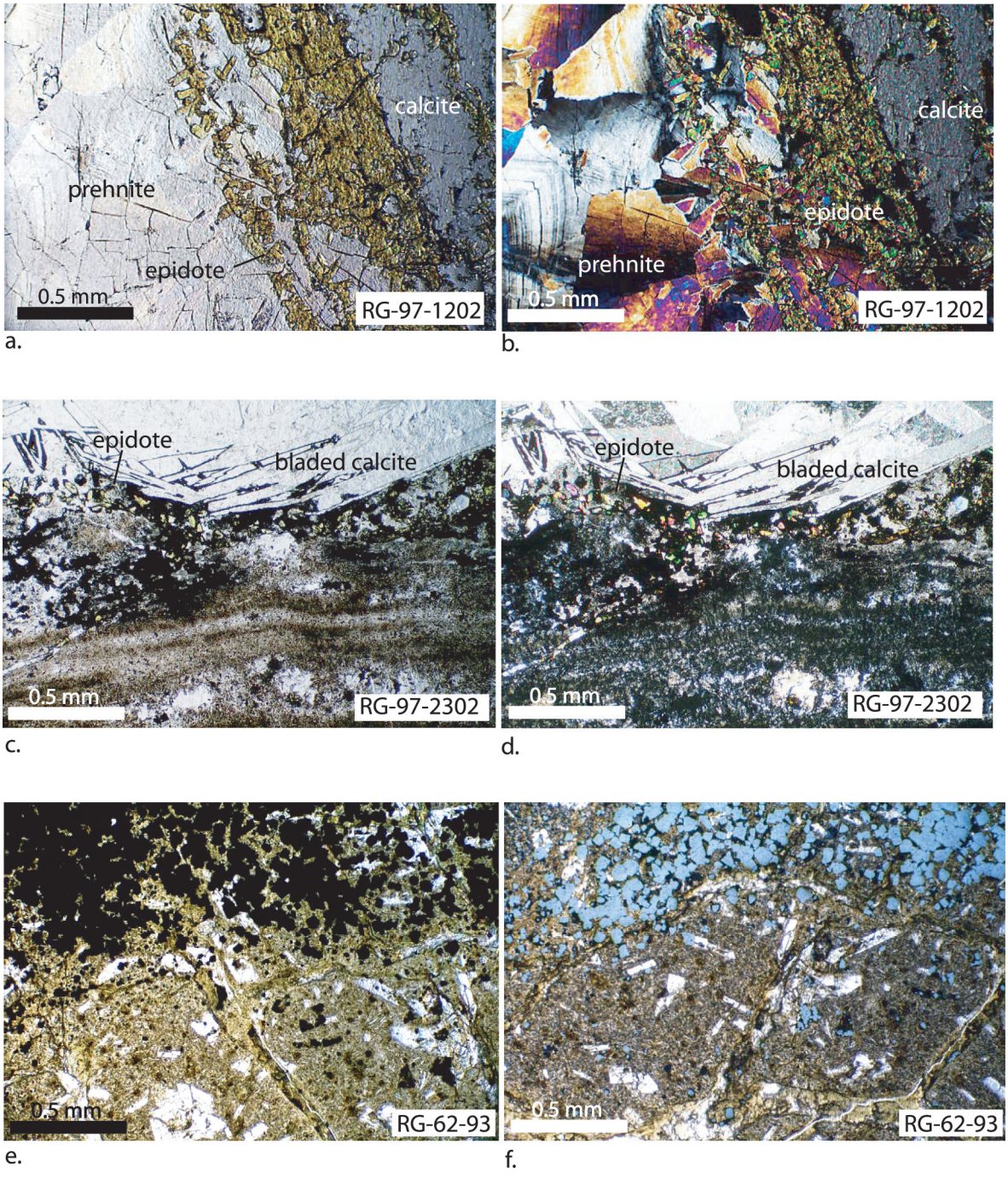

Figure 10. Photomicrographs of altered mafic rocks. a) and b) veinlet with prehnite, epidote and calcite in basalt (Tbg) (PPL and X polars); c) and d) bladed calcite and epidote in altered rhyolite (PPL and X polars); e) and f) pyrite-rich selvedge of chlorite-calcite veinlet in altered basalt (Tbg) (PPL and PPL/Ref).

marcasite replaced by pyrite), chalcopyrite, and sphalerite; appearance of bright-green to emerald-green chlorite (Fe-rich chamosite); and bleaching of vein and fracture selvedges in both mafic and felsic rocks. Subsidiary zones of potassic alteration are present along permeable faults and flow/intrusive contact breccias. Potassic alteration extends to the surface adjacent to the main veins where it is locally associated with stockwork veining which is overprinted by argillic alteration (Figs. 6 and 7).

In mafic rocks, the degree of replacement ranges to 95 volume percent, and veining forms up to 25 volume percent of the rock. Hand specimens are medium- to light-green-gray and

contain chlorite±calcite veinlets cut by narrow pyrite veinlets (0.5 to 2 mm wide) cut by quartz-pyrite±calcite veins (to 2 cm wide). In later veinlets calcite is locally bladed. Pyrite forms along vein margins and selvedges are commonly bleached. Plagioclase is partially to nearly completely replaced by albite, chlorite, smectite±illite/smectite, calcite, epidote, minor adularia, quartz, and apatite. Bright-green chlorite (Fe-rich clinochlore ± chamosite), pyrite, and leucoxene replace ferromagnesian minerals. Oxides are partially altered to pyrite and minor leucoxene. The groundmass is nearly completely replaced by chlorite, adularia, quartz, and lesser pyrite, marcasite, with variable sphalerite, chalcopyrite, apatite, rutile and titanite. Compared to intense propylitic alteration, adularia is more abundant and common in the groundmass. Pyrite is commonly rimmed by chalcopyrite followed by sphalerite. Prehnite is associated with zoned, rhombic adularia in veinlets in potassically altered rock at relatively shallow levels in 2600 N.

In felsic rocks the degree of replacement ranges to 90 volume percent, and veining forms up to 20 volume percent. In hand samples, rocks are light-gray to dark-green with pyrite concentrated in chlorite-rich lapilli, beds, and fragments. Sanidines are partially to completely adularized, turbid, and contain variable amounts of fine-grained quartz, kaolinite, chlorite, illite/smectite, epidote, apatite, titanite, rutile, and albite. Replacement by bright- to emerald-green chlorite (chamosite) is more common with depth. Plagioclase is turbid, displays patchy extinction, and is replaced by adularia, albite, and bright-green chlorite; crystal outlines are weakly preserved (see Table 2). Clastic fragments are replaced by chlorite or recrystallized to quartz ± adularia forming saccharoidal texture. The groundmass/matrix is cloudy and nearly completely replaced by minerals similar to those in the groundmass of mafic rocks. Veins and veinlets show a temporal progression from chlorite to pyrite/marcasite to quartz-adularia-sphalerite to quartz-epidote± hematite to chlorite to calcite (bladed and massive)-clay, and locally form stockworks. Dark purple amethystine quartz veinlets (1 to 3 mm wide) in flow-banded rhyolite, parallel to foliation, contain minor pyrite and chlorite along selvedges and epidote in cores.

Intense potassic—quartz-illite/sericite-pyrite/marcasite-adularia

Intense potassic alteration is present within 30 ft (~10 m) of the main veins. Similar to the outer potassic zone, the amount of replacement of wall rock minerals ranges up to 95 volume percent, but veining forms up to 35 volume percent of felsic rocks. Rocks are typically light-gray and pervasively bleached. Phenocrysts are nearly destroyed and identification of primary minerals is difficult. Rims of adularia on feldspars are distinctive. Despite an argillic overprint, traces of illite and adularia-rimmed feldspars are visible in thin sections of samples from surface outcrops along the projected trace of the main veins (Fig. 11a–d). Replacement of feldspars by illite (trace) is more common above the 5250 ft level (~1600 m), and gives way to replacement by emerald-green chlorite (chamosite) with depth (Fig. 11e–f). Kaolinite in feldspars is locally abundant. Cross-cutting veinlets show a temporal progression from chlorite to quartz-pyrite±rutile to quartz-sphalerite to quartz-illite-marcasite-sphalerite±galena (Fig. 9).

Silicic-potassic—quartz-adularia-illite/smectite-pyrite/marcasite

Silicic-potassic alteration is present in wall rocks of the main veins and includes secondary minerals present in the intense potassic zone as well as increased quantities of silica. In both mafic and felsic rocks the groundmass/matrix and veins contain abundant silica, adularia, calcite, sulfides, and minor selenides. This type of alteration coincides with early stages of vein formation and possibly with formation of silicic alteration near and at the paleosurface as described below.

Silicic—quartz±adularia±pyrite

Although similar in appearance to silicic-potassic, silicic alteration is a distinct type. Outcrops of siltstones of the Esmeralda formation (Tes) are intensely silicified adjacent to the main CG fault (Fig. 6) and appear texturally similar to sinters (Wallace, 1993; Goldstrand and Schmidt, 2002). Above the 6000 ft level (1830 m) and within 330 ft (100 m) of the CG vein, siltstones in core show similar effects of silicification. Moderate silicification of surface exposures of carbonaceous siltstones of the middle member of the Elko Prince formation (Tep 2; ≥ 5900 ft elevation or 1800 m) is present in the footwalls of the CG and GC veins (Fig. 6). Approximately 5 km northeast of the Ken Snyder mine, silicic alteration is well-developed in the red rhyolite (Trf) where it forms the footwall of a N-S fault; sinters and opalized sediments formed at or close to the paleosurface are present in the hanging wall. This style of alteration is distinct from silicic-potassic because it contains little to no adularia or bladed calcite.

Argillic—smectite-kaolinite±carbonate±pyrite

Argillic alteration overprints other types of alteration and exhibits both lithologic and structural controls. It is most common in permeable volcaniclastic rhyolites (Tep and Tes) above the 5800 ft level (1770 m), and along structures and flow/contact breccias. Argillized rhyolites are partially replaced by clays that form 5 to 35 volume percent of the rocks. XRD and PIMA analyses confirm that Ca-montmorillonite is the dominant clay and minor kaolinite is common. Within the main ore zones, fractures, veinlets, and fault surfaces containing Ca-montmorillonite—pyrite (commonly framboidal) ± siderite cross-cut earlier stages of alteration and the main veins.

Surface exposures of bleached, weakly to strongly argillized tuffs are widespread in the Midas district. Along the

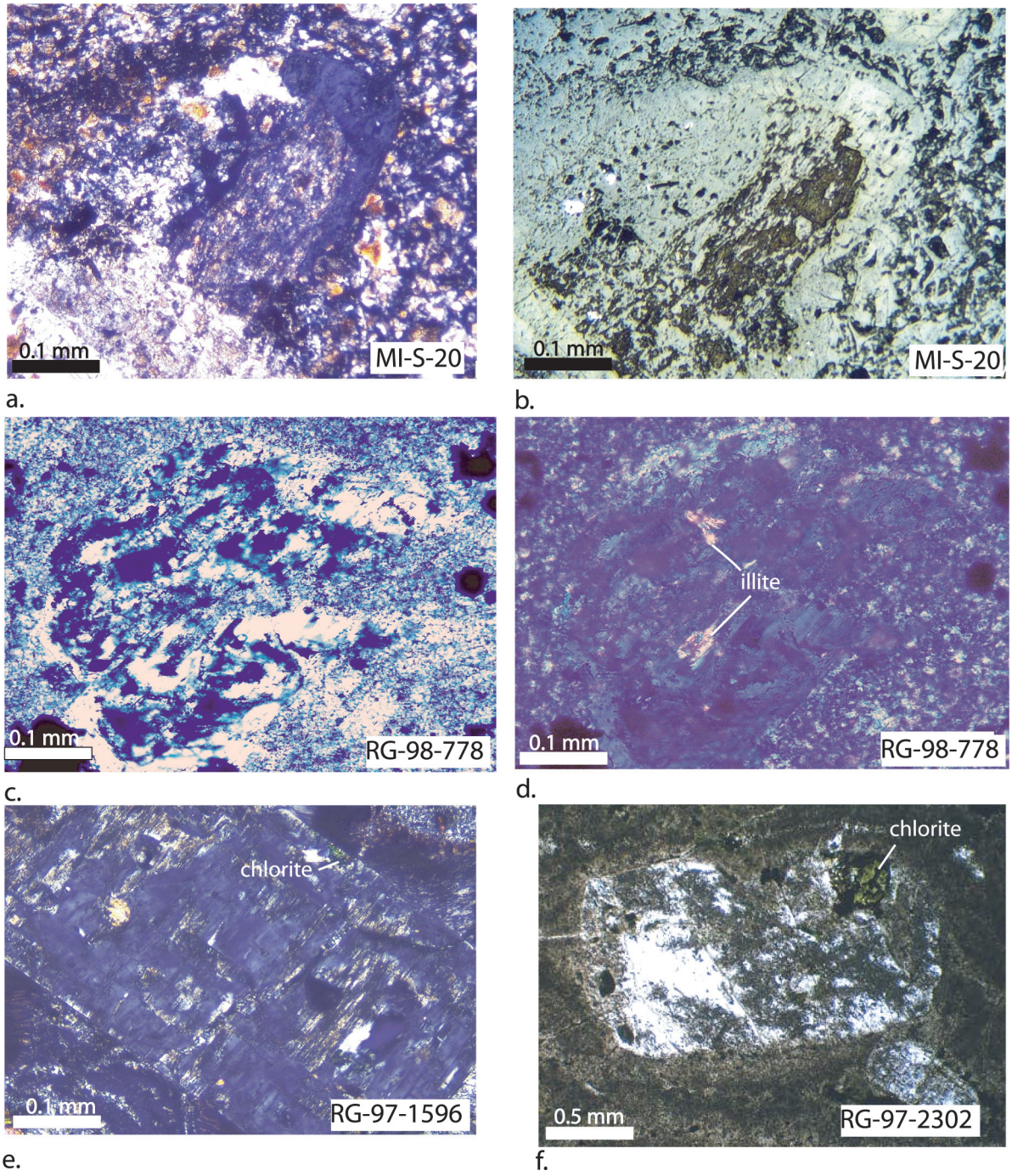

Figure 11. Photomicrographs of altered felsic rocks. a) and b) sanidine altered to clay, quartz, adularia, pyrite, with rim of adularia (X polars, Ref); c) and d) sanidine altered to clay, quartz, adularia, illite, with rim of adularia and trace of illite (PPL, X polars); e) and f) adularized sanidine replaced by chlorite, clay, trace of pyrite, and quartz (X polars, PPL).

CG fault, argillic alteration overprints potassically altered volcaniclastic rocks; bleached and Fe-stained rocks contain up to 20 volume percent casts of pyrite. In more distal areas, weakly welded tuffs of the Elko Prince formation (Tep) contain lithic fragments that have been altered to chlorite, calcite, and minor pyrite (now oxidized) with pumiceous fragments and feldspars that have been weakly to strongly replaced by clay. In these rocks argillic alteration appears to have overprinted propylitic alteration. In some areas vertical goethite-coated fractures in the tuffs grade outwards to bleached and argillized tuffs, suggestive of acid generation due to the weathering of pyrite along fractures and supergene argillic alteration.

MAIN STAGE VEIN FORMATION

The Colorado Grande and Gold Crown veins formed during numerous episodes of mineral deposition and brecciation (Goldstrand and Schmidt, 2000; D.A. Rhys, unpublished report, 2002; Leavitt et al., 2004). These episodes have been divided into six main stages, most of which contain substages (Table 3, Figs. 9 and 12); all stages are not present throughout veins. During Stage I, wall rocks were brecciated, and open spaces were filled with chalcedonic to cryptocrystalline quartz. In some areas, subsequent disruption of wall rocks produced clast-supported breccias with fragments of white, chalcedonic to fine-grained quartz and wall rock in a matrix of quartz ± adularia. Deposition of crustiform, colloform bands of chalcedony ± adularia ± sulfides ± selenides followed, producing barren to weakly mineralized vein material. Stage I probably coincides with silicic-potassic alteration; cross-cutting veinlets show that it followed formation of sphalerite-bearing veinlets associated with potassic alteration.

During Stage II, crustiform and colloform bands were deposited to form high-grade ore. Alternating dark and light bands are composed of quartz, calcite, adularia, sulfides, selenides, and electrum. Dark bands are enriched in electrum, naumannite, chalcopyrite, pyrite, sphalerite, and minor galena, aguilarite, and marcasite. Trace amounts of other selenides have been reported and include: fischesserite, clausthalite, eucairite, berzelianite, and eskebornite (Goldstrand and Schmidt, 2000). The banded ore of this stage ranges from several centimeters to several meters in thickness, and contains up to 20 metal-rich bands (D.A. Rhys, unpublished report, 2002). Metal-rich bands commonly coincide with fine-grained, adularia-rich bands, and are more abundant during the earlier part of Stage II. The abundance of electrum decreases with later bands and subsequent stages. Adularia and mosaic quartz (recrystallized texture of Dong et al., 1995) are more abundant in earlier bands; pyrite and crystalline quartz are more abundant in later bands. Both bladed and massive calcite is present in Stage II. Interstitial massive calcite is generally more iron-rich than bladed calcite, as determined by staining and cathodoluminescence. Pyrite is most abundant in early and late bands; chalcopyrite is locally abundant in later electrum-bearing bands. Banded ore exhibits several minor intermittent episodes of brecciation and/or turbulence. Fragments of older bands, lithic clasts, and xenocrysts reflect varying degrees of transport within these breccias. Towards the end of Stage II, amethystine quartz filled interstices of bladed calcite in the northern portion of the GC vein; further south it formed thin seams in banded ore of the Discovery vein.

Widespread breccias up to several meters wide comprise Stage III veins. The breccias include clasts of veins and lithic fragments up to several centimeters in size in a calcite-pyrite/marcasite-rich matrix with quartz, adularia, and minor selenides, chalcopyrite, sphalerite, and electrum. Bladed calcite typically replaced by quartz was deposited in portions of the CG and GC veins at the beginning of Stage III. Locally chlorite is common, and in some areas specular hematite is relatively abundant.

Stages IV, V, and VI represent a decline in Au and Ag. Stage IV is a discontinuous but distinctive horizon, up to 10 cm wide, of bladed calcite replaced by white quartz that forms blocky faces. Amethystine quartz bands and a clastic dike comprise Stage V. The clastic dike disrupted earlier vein material and produced loosely consolidated, matrix-supported breccias with fragments of banded quartz veins and wall rocks in a calcite-rich matrix that show sorting adjacent to contacts (Goldstrand and Schmidt, 2000; Rhys, unpublished report, 2002). In the northern and southern portions of the deposit, veins of amethystine quartz cut across older bands; elsewhere amethystine quartz fills interstices of bladed calcite (replaced by white quartz). During Stage VI, parallel to cross-cutting veins containing brownish crystalline and drusy clear quartz, pyrite/marcasite, and minor sphalerite formed. Late cross-cutting veinlets and fracture coatings of euhedral to framboidal pyrite, smectite (Ca-montmorillonite), ± Fe-rich calcite and siderite are common.

GEOCHEMISTRY

Several studies of gold-quartz veins in the Midas district and Ken Snyder mine have characterized geochemical zoning within the veins and adjacent wall rocks (Blair, 1991; Cleverly, 1997; Goldstrand and Schmidt, 2000). Gold-quartz veins in the Midas district (not specifically within the Ken Snyder mine) demonstrate a strong increase in As, Sb, and Hg at the surface and a slight increase in base metals with depth (Blair, 1991). In a study of the CG vein and wall rocks, Goldstrand and Schmidt (2000) noted a strong positive correlation between Au, Ag, Se, and Cu, and enrichment in Au, Ag, Se, Cu, Sb, F, and Te, and depletion in Zn, Fe, Hg, and As in the vein (see Tables 1 and 2, Goldstrand and Schmidt, 2000). In a mass balance study of the GC vein, Cleverly (1997) compared analyses of vein, wall rock breccias, and fault gouge material to a least altered standard rock (average of 75 vol% rhyolite and 25 vol% basalt to represent proportions of host rocks). Relative to this standard, vein material is enriched in Ag, Ni, Mo, Pb, Rb, Se, Cu, Li, Be, Bi, Sb, W, and depleted in Mn, Sr, V, Zn, As, Co. All three zones (vein, breccia, gouge) showed enrichment in Mo, Ag, Be, and W, and depletion in Zn, Co, V, Sr, and As. Se enrichment was restricted to the vein and gouge material. Results of the present study expand upon those of the previous studies and are described below.

Analysis of two sets of data was carried out for this study. A new set of ICP data includes analyses of major oxides and trace elements for selected samples of core, primarily from 1400 N section, and the surface (Appendix A). The analyses have been used to create correlation matrices, isocon diagrams, and assess chemical changes that accompanied alteration and mineralization. Existing ICP data for drill holes in the 1400 N and 2600 N sections (provided by Franco-Nevada) were compiled and plotted to show spatial variations in geochemistry.

TABLE 3. PARAGENESIS OF THE COLORADO GRANDE AND GOLD CROWN VEINS, KEN SNYDER MINE, MIDAS

Stage	Substage					
I early vein (silicic-potassic)	a. chalcedony/ crypto-crystalline quartz	b. breccia; quartz matrix; fragments of wall rock; chalcedony ± adularia	c. crustiform, colliform bands of chalcedony ± adularia ± sulfides (py>sp) ± selenides (nm>>ag)			
II main ore stage	a. colloform, crustiform bands; sulfides (py>>sp- ga>cp) > selenides (nm>>ag), electrum, adularia, calcite (bladed and massive), quartz (recrystallized)	b. breccia ± disrupted bands, lithics, xenocrysts	c. colloform, crustiform bands; selenides (nm>>ag) > sulfides (cp>sp- py-ga), electrum, adularia, calcite (bladed and massive), quartz (recrystallized)	d. breccia ± disrupted bands	e. colloform, crustiform bands; sulfides (py>ma-sp- ga-cp) > selenides (nm>ag), electrum, adularia, calcite (bladed and massive), quartz (recrystallized)	f. locally amethystine quartz (N end)
III breccia	a. bladed calcite	b. replacement by white quartz	c. breccia; calcite- rich matrix; lithics, xenocrysts, minor sulfides (py/ma> cp>sp)>>selenides (nm); trace electrum; ± specular hematite ± chloride			
IV bladed calcite replaced by quartz	a. white quartz after bladed calcite; minor remnant calcite; sulfides (py>sp); leucoxene.					
V amethystine quartz	a. amethystine quartz; minor sulfides (py/ma>>sp); trace electrum and illite	b. clastic dike/phreatic breccia				
VI drusy quartz, massive calcite	a. coarse-grained, brownish to clear crystalline quartz	b. interstitial calcite	c. cross-cutting veinlets with pyrite- clay ± carbonate			

abbreviations: ag—aguilarite; cp—chalcopyrite; ga—galena; ma—marcasite; nm—naumannite; py—pyrite; sp—sphalerite

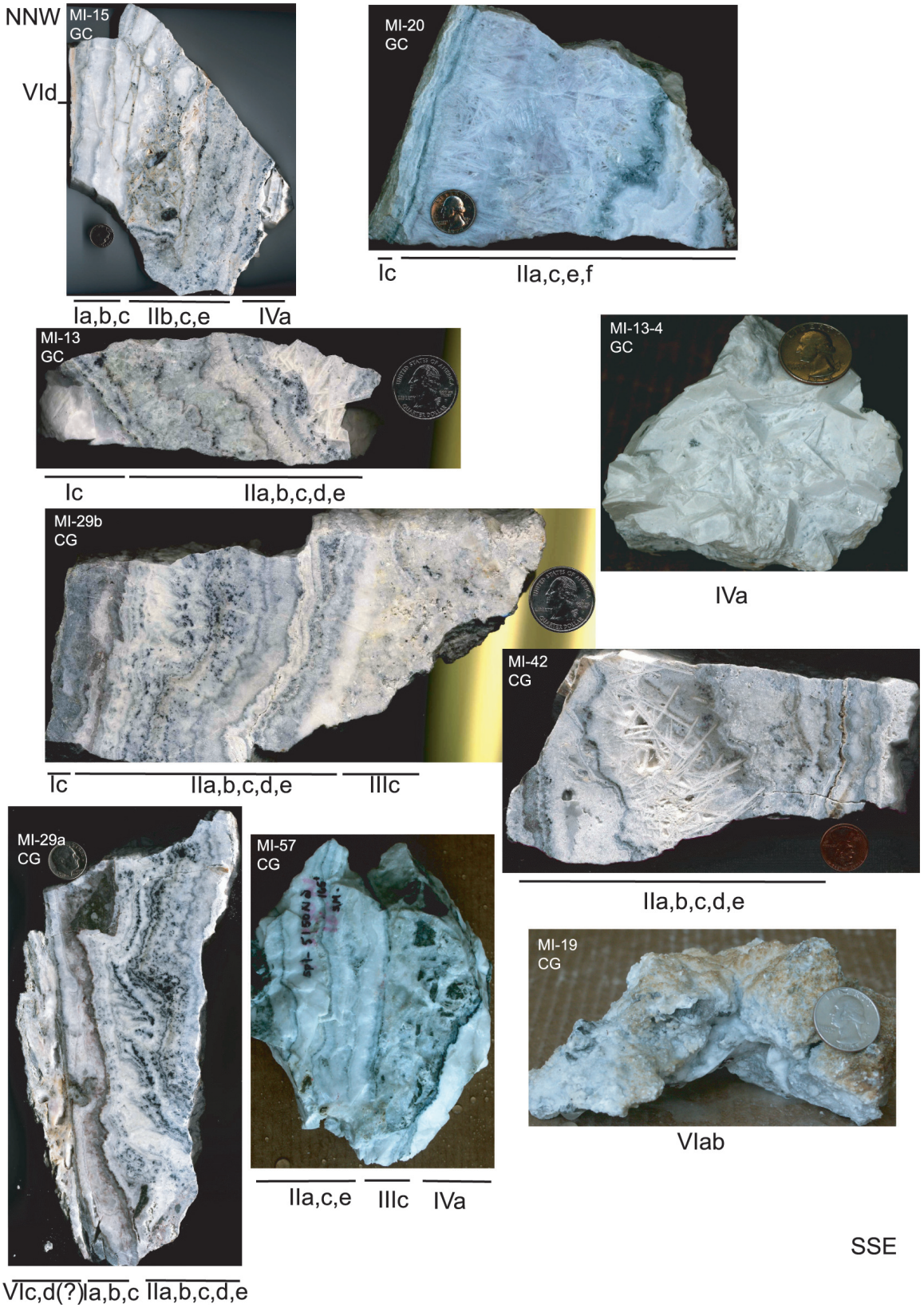

Figure 12. Representative samples of stages of Colorado Grande (CG) and Gold Crown (GC) veins, arranged from NW portion of the vein system at top of page to S portion at bottom of page. Sample number, vein, and stages/substages are notated on photographs.

Geology and locations of drill holes are shown in Figures 4a and 4b. Although the older trace element analyses utilized less thorough digestion techniques compared to new data, they reveal vertical and lateral geochemical zonations associated with the CG and GC veins.

Correlation matrix

A correlation matrix for major, minor and trace element data for 83 samples from core in section 1400 N (Appendix A) was constructed using statistical analysis tools in the computer program EXCEL. These data include wall rock but no high-grade vein material; the matrix does not include Au analyses. Results are useful in assessing the behavior of typical pathfinder elements as well as immobile elements; the latter are described in more detail in mass balance calculations below. Positive correlations that resulted in $r^2 > 0.5$ are summarized in Table 4. Ag-Se and Fe-Ti are the most strongly positively correlated ($r^2 > 0.9$). Very strong positive correlations exist for As-S and S-Sb ($0.8 \le r^2 < 0.9$); and K-Pb and K-Tl ($0.7 \le r^2 < 0.8$). Moderately positive correlations exist for As-Mo, Hg-S, Hg-Sb, Sb-Tl ($0.6 \le r^2 < 0.7$), and As-Hg, Bi-Mo, K-Zn, Al-Fe, and Al-Ti ($0.5 \le r^2 < 0.6$). Negative correlations that resulted in $r^2 < 0.5$ are also summarized in Table 4. Negative correlations exist for K-Ca, Fe-K, K-Mg ($-0.7 \le r^2 < -0.6$), and Zn-Ca, and Mg-Zn ($-0.6 \le r^2 < -0.5$).

TABLE 4. RESULTS OF CORRELATION MATRIX FOR MAJOR AND TRACE ELEMENTS (WITHOUT Au AND HIGH-GRADE VEIN MATERIAL), BY DEGREE OF CORRELATION (r^2 FACTOR), SECTION1400 N, BASED ON NEW ICP-MS DATA. INCREASING POSITIVE CORRELATION WITH INCREASING VALUES OF r^2; INCREASING NEGATIVE CORRELATION WITH DECREASING VALUES OF r^2.

Negative Correlations				Positive Correlations				
$-0.9 \le r^2 < -0.8$	$-0.8 \le r^2 < -0.7$	$-0.7 \le r^2 < -0.6$	$-0.6 \le r^2 < -0.5$	$0.5 \le r^2 < 0.6$	$0.6 \le r^2 < 0.7$	$0.7 \le r^2 < 0.8$	$0.8 \le r^2 < 0.9$	$0.9 \le r^2 < 1.0$
Co–La	Pb–Ca	Ca–Ce	Pb–Al	Al–Fe	Al–Co	Al–Mg	As–S	Ag–Se
Co–Pb	Rb–Ca	K–Ca	U–Ca	Al–Ti	As–Mo	Al–Ni	Ce–Zn	Ce–La
	Ce–Co	La–Ca	Zn–Ca	Al–V	Ba–Ce	Al–Sr	Co–Fe	Ce–Nb
	Ce–Mg	Nb–Ca	Cd–Co	As–Hg	Ca–Fe	Ca–Co	Co–Mg	Fe–P
	Ce–Sr	Th–Ca	Cd–Mg	Al–Tl	Ca–Mg	Ca–Mn	Co–Mn	Fe–Ti
	Ce–V	Tl–Ca	Cd–Sr	Ba–K	Ca–P	Ca–V	Co–Ni	Fe–V
	Co–K	Ce–Fe	Co–Tl	Ba–La	Ca–Sr	Ce–Pb	Co–P	K–Rb
	Co–Na	Ce–Ni	Cr–Ta	Ba–Nb	Ca–Ti	Ce–Ta	Co–Sr	La–Nb
	Co–Th	Ce–P	Fe–Rb	Ba–Th	Cd–Ce	Ce–Th	Co–Ti	Mg–Ni
	La–K	Co–Ta	K–Mn	Ba–Y	Cd–Ta	Cu–Li	Co–V	P–Ti
	La–Sr	Fe–K	Mg–Ta	Ba–Zn	Cd–Zn	Fe–Sr	Fe–Mn	P–V
	La–V	Fe–La	Mg–Tl	Bi–Mo	Ce–K	K–La	La–Pb	Ti–V
	Mg–Pb	Fe–Nb	Mg–U	Ca–Ni	Ce–Rb	K–Nb	La–Ta	
	Nb–V	Fe–Pb	Mg–Zn	Cd–Pb	Ce–Y	K–Pb	La–Th	
	Ni–Pb	Fe–Th	Mn–Nb	Cd–Rb	Cr–Ni	K–Ta	Mg–Sr	
	P–Pb	K–Mg	Mn–Th	Cd–Th	Cu–Te	K–Th	Mn–P	
	Pb–Ti	K–Ni	Mn–Tl	Cr–Mg	Fe–Mg	K–Tl	Mn–Ti	
	Pb–V	K–P	Ni–Ta	Fe–Ni	Hg–S	La–Rb	Mn–V	
	Th–V	K–Sr	Ni–Tl	K–U	Hg–Sb	La–Y	Nb–Ta	
		K–Ti	Ni–Y	K–Zn	Hg–Tl	La–Zn	Nb–Th	
		K–V	Ni–Zn	Li–Te	La–U	Mn–Sr	Nb–Zn	
		La–Ni	P–Rb	Mg–P	Mg–Mn	Nb–Pb	Pb–Th	
		La–P	P–Ta	Nb–Tl	Mg–V	Nb–Rb	S–Sb	
		La–Ti	Rb–Ti	Ni–V	Nb–U	Ni–Sr	Sr–V	
		Mg–Nb	Sr–Th	Pb–U	Nb–Y	P–Sr	Ta–Th	
		Mg–Rb	Sr–Zn	Rb–U	Pb–Rb	Rb–Tl		
		Mg–Th	Ti–V	U–Y	Pb–Ta	Sr–Ti		
		Nb–Ni		Y–Zn	Rb–Tl			
		Nb–Sr			Rb–Th			
		Nb–Ti			Rb–Zn			
		Ni–Rb			Sb–Tl			
		Ni–Th			Ta–Y			
		P–Th			U–Zn			
		Rb–Sr						
		Rb–V						
		Sr–Th						
		Ta–V						
		Th–Ti						

Mass balance calculations

Changes in chemical compositions of the main lithologies due to alteration have been assessed with isocon diagrams. These diagrams represent a graphical method of solving equations used to determine mass gains and losses during alteration (Gresens, 1967; Grant, 1986). In these plots, a least altered sample, or average composition of several least altered samples, has been plotted for each of the main lithologies present at Midas (rhyolite, felsic volcaniclastic, and basalt/mafic). The concentrations are plotted on both the x and y axes establishing a baseline, or line of constant mass, from which changes in concentrations of elements can be assessed. Concentrations of a variety of chemical components are plotted along the x-axis for the least altered sample, and along the y-axis for altered samples; in this case, all concentrations are shown in parts per million (ppm) on a log scale. Concentrations of immobile elements and oxides in altered rocks, particularly those that demonstrate a high degree of correlation, are used to establish isocons—lines connecting points of equal concentration (Grant, 1986). The isocon is the best fit of a straight line through these points, and is drawn by visual inspection. The isocon can be used to assess changes in mass due to changes in volume.

Assuming that alteration is pervasive, a volume factor (F_v) is determined by examining ratios of what are generally thought to be immobile elements and oxides such as Al_2O_3 (or Al), Fe_2O_3 (or Fe), TiO_2 (or Ti), Zr, Y, and Nb in unaltered to altered samples (Gresens, 1967; Grant, 1986; Leitch and Lentz, 1994). The volume factor F_v is the ratio of the volume of altered rock to the volume of least altered (parent) rock (V_a/V_l) and equals the ratio of the mass of altered rock to the mass of least altered rock (M_a/M_l) times the ratio of density (or specific gravity) of the least altered rock to the density of the altered rock (S_l/S_a). Variation in specific gravity is generally negligible, so M_a/M_l can be estimated with the inverse immobile element weight (X) ratio, X_l/X_a. F_v can be estimated by examination of the ratios of immobile components such as Al, Ti, Zr, and Y. Changes in the concentration of immobile elements provide a means of assessing changes in mass and/or volume, and are used to generate an isocon. An increase in volume will yield a decrease in concentration (mass) of immobile components, and a decrease in volume will yield an increase in concentration (mass) of immobile components. Increases in volume can occur with hydration, sulfidation, veining, and/or carbonation, whereas decreases in volume can occur with leaching (Leitch and Lentz, 1994). Ultimately apparent losses or gains of more mobile components are assessed relative to isocons, if a valid isocon exists.

Hand specimen and petrographic observations of analyzed samples can be used to verify or rule out apparent variations in volume. In this study, the percentage of veining versus replacement or pervasive alteration was recorded for samples, as described in the section on petrography and in Tables 2a–b, and Figures 8a and 8b. Because the isocon method does not work well for veined samples (Grant, 1987), samples that contain more than 10 volume percent veining were noted, and ultimately discarded from the final isocon diagrams. Densities of all samples were determined using an air-comparison pyncnometer. Densities did not vary more than 0.1 % and, therefore, have been ignored for the purposes of mass balance considerations; any perceived changes in mass would be due to changes in volume.

The selection of a least altered parent rock is critical to the construction and interpretation of the isocon diagrams. Variability within original compositions can effect the construction of isocons, and interpretation of changes in mass. For the mafic rocks at Midas, a least altered basalt was generated from an average of six analyses of weakly propylitized basalts in the area (least altered basalts available; Appendix A). As shown in Figures 5a and 5b, compositions range from tholeiitic to weakly calc-alkaline. Two of the analyses represent replicate analyses of the same rock and show little variation. To assess the effect of variability in the composition of the protolith on isocon diagrams, chemical components of the six least altered samples were plotted versus those of the averaged, least altered basalt (Fig. 13a). A gray bar parallel to the line of constant mass marks the maximum range of values for highly correlated immobile elements. This bar is compared to potential isocons in the following diagrams, and demonstrates the effect of variation within the least altered sample on the interpretation of changes in mass and volume with alteration. Vertical gray lines mark the ranges of all other components, and are included on subsequent plots of altered basalts for comparison. Major oxide and trace element data (Appendix A) were utilized to generate isocon diagrams for mafic and felsic rock types.

Mafic rocks: In Figures 13b and 13c, oxides and selected trace elements in altered mafic rocks (Tbg) have been plotted relative to the least altered standard basalt (described above). Samples were dominantly pervasively altered. One potassically altered sample contained greater than 10 volume percent veinlets (open symbols), and was not incorporated in the construction of isocons. The diagram for moderately to intensely propylitically altered mafic rocks of unit Tbg (Fig. 13b) shows that TiO_2, Zr, and total iron as Fe_2O_3 are relatively immobile. A correlation matrix for these data indicates that Fe_2O_3-TiO_2 ($r^2 > 0.9$), Fe_2O_3-Zr, and TiO_2-Zr ($0.8 \leq r^2 < 0.9$) are strongly correlated; Al_2O_3 does not show a strong correlation with the other immobile elements, suggesting that Al_2O_3 is mobile. An isocon connecting Fe_2O_3, TiO_2, and Zr shows an apparent overall mass increase ranging from 30 to 75 volume percent, requiring decreases in volume of 25 to 70 volume percent. The "isocon" lies within the range of concentrations of immobile elements in the original least altered samples. The variability in immobile elements can be explained by variable compositions of the least altered basalts rather than a change in mass and/or volume. In addition, hand specimen and petrographic observations do not provide evidence of significant decreases in volume such as leaching; and highly veined samples that could represent increases in volume were removed from the isocon analysis.

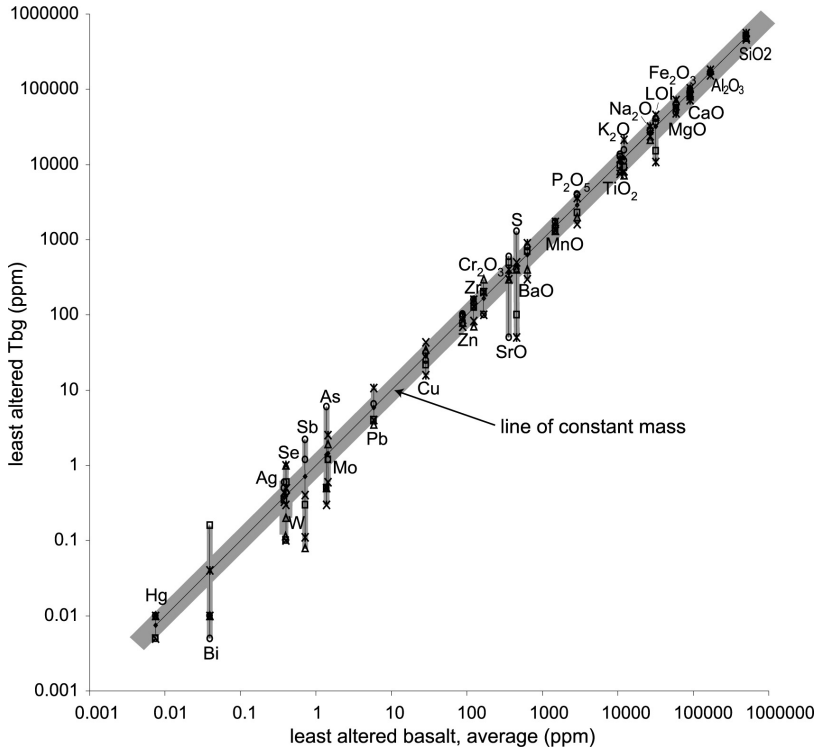

Figure 13a. Major oxides and selected trace and minor elements of 6 least altered (weakly propylitized) basalts (Tbg) from Midas district (y-axis) vs. least altered average basalt of the 6 samples (x-axis). Diagram demonstrated variability of components within least altered host rocks. Vertical gray bars mark range of values for each component, and gray bar parallel to line of constant mass approximates maximum variation in immobile elements in least altered rocks.

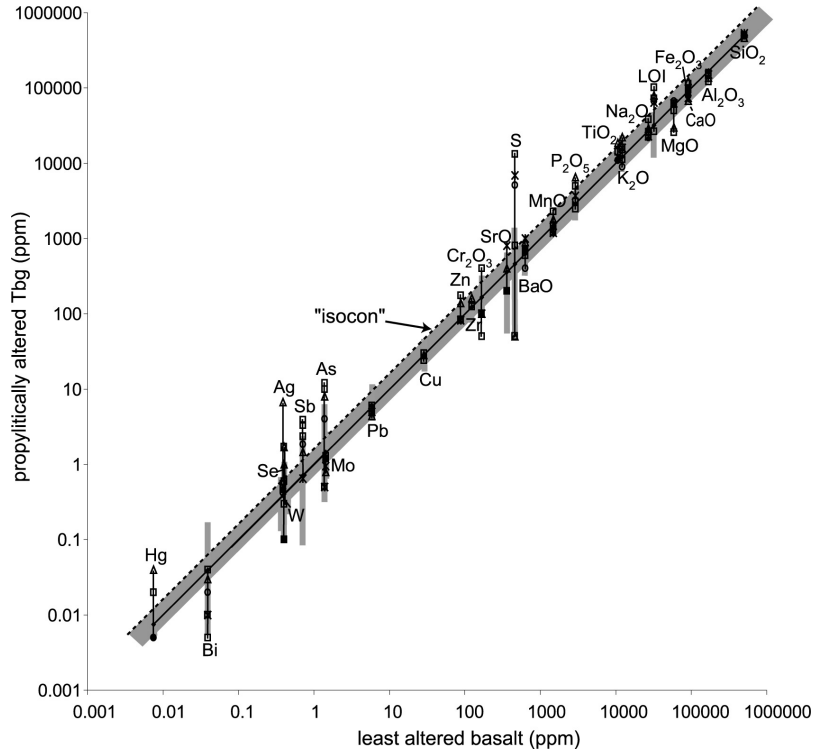

Figure 13b. Major oxides and selected trace and minor elements in moderately to intensely propylitically altered basalts (Tbg) (y-axis) vs. least altered average basalt (x-axis). Dashed line is apparent isocon determined from change in immobile elements; isocon lies within variation associated with host rock compositions.

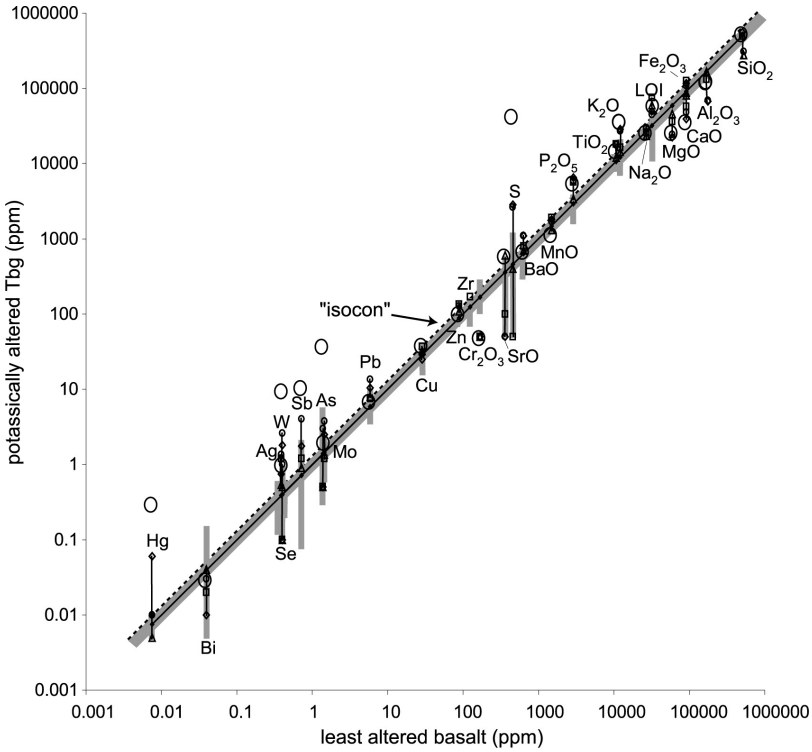

Figure 13c. Major oxides and selected trace and minor elements in potassically altered basalts (Tbg) (y-axis) vs. least altered average basalt (x-axis). Dashed line is apparent isocon determined from change in immobile elements; isocon lies within variation associated with host rock compositions. Open symbols are values for potassically altered Tbg with >10 vol% veining.

Without any significant mass or volume change accompanying alteration, concentrations of other components in altered rocks can be compared to the ranges of values in the least altered rocks marked with vertical lines. MgO displays slight losses, P_2O_5, and SrO show weak gains, and Cr_2O_3 shows both. Sulfur and volatile elements (shown as LOI, or loss on ignition, on Figs. 13a–c) exhibit the largest gains. Of the trace elements, Ag, As, Sb, Se, and Hg show gains. Plots generated with elemental geochemical data showed similar gains and losses.

The diagram for moderately to intensely potassically altered mafic rocks (Tbg; Fig. 13c) shows that total iron as Fe_2O_3, TiO_2, and Zr are still relatively immobile. A correlation matrix for these data indicates that Fe_2O_3-TiO_2 ($0.8 \leq r^2 < 0.9$) are the most strongly correlated; an incomplete set of Zr data precluded assessment of correlation with the other immobile elements. The placement of the isocon from the previous diagram (Fig. 13b) appears valid for this diagram; again it lies within the range of original basalt compositions, and no mass or volume changes are required. When compared to the ranges of concentrations in least altered basalts, CaO, MgO, and Cr_2O_3 show losses. K_2O, volatile elements, S, Hg, As, Sb, Ag, W, Pb, and Mo show gains. The veined sample (shown with open symbols) shows increased gains in Hg, W, Sb, As, and S, suggesting that these elements were deposited, at least in part, in open fractures and veins. Plots generated with elemental geochemical data showed similar gains and losses.

Felsic rocks: Isocon diagrams were constructed for rhyolites of units Tlt, Tjb, and Trf using both sets of geochemical data. Major oxides and elemental analyses yielded similar results. Figures 14a and 14b display isocon diagrams generated with elemental analyses (Appendix A). In isocon diagrams using major oxides, results were similar to those for mafic rocks; SiO_2 showed little change with increasing intensity of alteration. Because unaltered to weakly altered samples of rhyolites of units Tlt and Tjb were not available, a relatively fresh sample of the red rhyolite (Trf) was used as a proxy for the least altered protolith. The previous diagrams for basalts demonstrated the potential compositional variation in protolith for that rock type. In lieu of availability of additional analyses for unaltered rhyolites in the Midas district, a similar range of original compositions was used to approximate potential variation in composition of the felsic protolith of units Tlt and Tjb. Study of hand specimens and thin sections support the contention that these rocks are somewhat variable; e.g., contain locally abundant mafic inclusions and clasts. In addition to including the gray bar of compositional variation, an analysis of fresh to weakly propylitically altered red rhyolite was plotted versus the fresh sample (Fig. 14a). Vertical gray lines mark the ranges of all components, relative to the fresh sample, and are included on the isocon diagram for units Tjb and Tlt.

The isocon diagram for potassically altered rhyolites of units Tjb and Tlt (Fig. 14b) includes samples that are pervasively

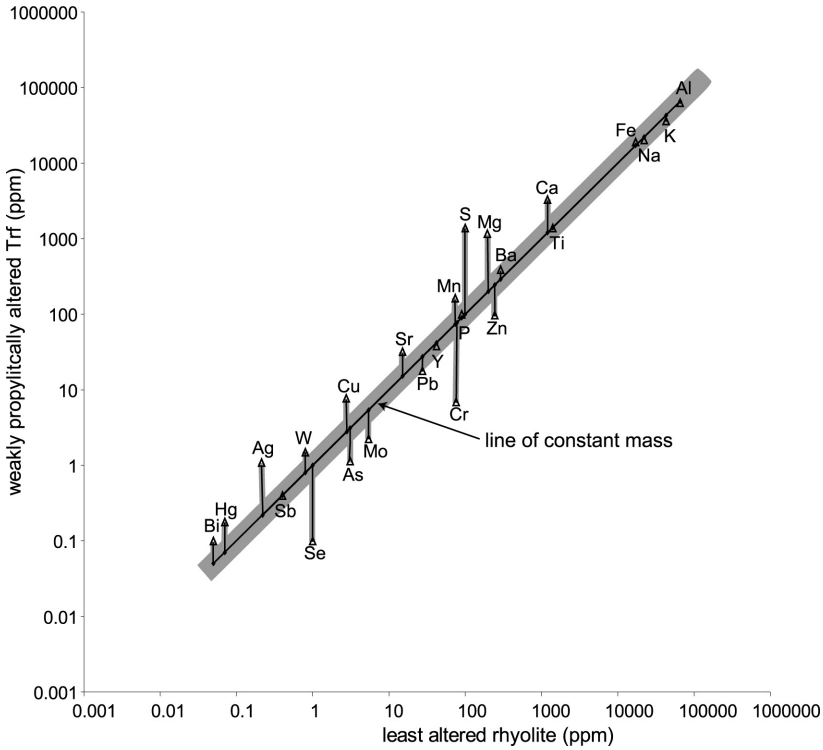

Figure 14a. Selected major, trace, and minor elements in weakly propylitically altered rhyolite (Trf) (y-axis) vs. least altered rhyolite (Trf) from Midas district (x-axis). Vertical gray bars mark range of values for each component, and gray bar parallel to line of constant mass approximates maximum variation in immobile elements in least altered rock (obtained from mafic rocks, Fig. 13a; see text for further explanation).

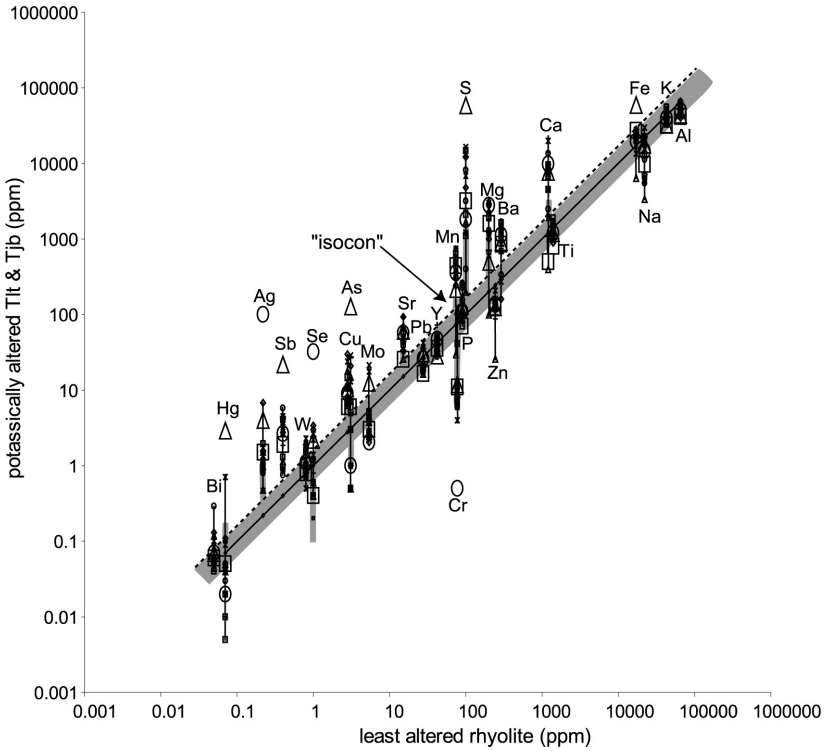

Figure 14b. Selected major, trace, and minor elements in potassically altered rhyolite (Tlt and Tjb) (y-axis) vs. least altered rhyolite (x-axis). Dashed line is apparent isocon determined from change in immobile elements; isocon lies within variation associated with host rock compositions. Open symbols are values for potassically altered Tjb and Tlt with >10 vol% veining.

altered (small filled symbols), and several samples that contain more abundant veining (>10 vol%; open symbols). Within the pervasively altered samples (>10% veined samples not included), Fe-Ti and Y-Al are relatively well correlated ($0.5 \leq r^2 < 0.6$), although the pairs lie above and below the line of constant mass. An isocon between the pairs would roughly coincide with the line of constant mass. The "isocon" lies within the estimated range of concentrations of immobile elements in the original least altered sample, and the variability in immobile elements can be explained by variable compositions of the protolith. If this estimated range is reasonable, then it is also reasonable to conclude that there has been no significant mass or volume change accompanying pervasive alteration. Therefore, concentrations of other components in pervasively altered rocks are compared to the ranges of values in the weakly-altered rhyolite marked with vertical lines. Barium, Mg, S, Sr, Cu, Se, P, W, Sb, Ag, and Bi show gains; Na, Fe, Zn, and Cr show losses. Calcium, As, and Mo show gains and losses. Samples containing greater than 10 volume percent veining exhibit changes in all elements similar to less-veined rocks. Iron showed a strong gain in one sample, and the magnitude of gains in S, Se, As, Sb, and Hg are greater than samples with less than 10 volume percent veining.

Unaltered or weakly altered samples of the felsic volcaniclastic units Tep and Tes were not available. Therefore, a propylitically to argillically sample of unit Tep was used to generate a line of constant mass for these rocks. The range of compositions for basalts was used as a best estimate for the compositional range of these samples (gray bar). In the diagram for moderately to intensely potassically altered units Tep and Tes (Fig. 15a), an isocon has been drawn using Al, Fe, and Ti in pervasively altered samples (small symbols). A correlation matrix for these data indicates that Al-Fe, Fe-Ti ($0.8 \leq r^2 < 0.9$), and Ti-Al ($0.7 \leq r^2 < 0.8$) are strongly correlated. The isocon lies slightly below the estimated range of concentrations of immobile elements in the original least altered samples, and may indicate a slight loss in mass and/or increase in volume. It may reflect argillic alteration in the least altered rock. Changes in concentration are compared to this isocon. Sulfur, Al, Ti, Mg, P, Sr, Cr, Cu, Sb, W, Ag, Bi, and Hg, show gains, whereas Fe, K, Na, Ca, Ba, Mn, Zn, Y, Pb, As, Mn, and Se show both gains and losses. In a plot of argillically altered samples of units Tep and Tes (Fig. 15b), an isocon has been drawn using Al, Fe, Ti, and Y in pervasively altered samples. As for other alteration types, these elements show a relatively high degree of correlation. Sulfur, Al, Fe, K, Ti, Mg, P, Y, Pb, Cu, Sb, W, Ag, Hg show gains relative to this line. Sodium, Ca, Ba, Mn, Zn, Sr, Cr, Mo, As, Se, and Bi show both gains and losses. Although the samples exhibit argillic alteration, this alteration type is typically an overprint on previously altered samples. Three of the samples located along the surface trace of the Colorado Grande vein were potassically altered prior to argillization. The other two samples exhibited characteristics of earlier propylitic and potassic alteration. Therefore, the gains and losses may have occurred during more than one stage of alteration.

Variations in major oxides and trace elements in mafic and felsic host rocks

Because geochemical variations in host rocks with <10 volume percent veining generally are not due to changes in mass or volume, as determined through mass balance calculations, variations in major and trace element concentrations generally reflect absolute gains and losses of elements that accompanied alteration. As would be expected from the distribution of alteration types (Figs. 6 and 7) and mass balance considerations described above, major oxides and trace elements (from core samples from section 1400 N) show variations with distance from the CG vein and subsidiary hanging wall structures (Fig. 16). Mafic rocks represent a relatively homogeneous lithology across this transect; felsic lithologies are more variable and include densely welded and glassy tuffs and flows of unit Tjb in the footwall, and moderately to weakly welded tuffs of unit Tep 3, and carbonaceous siltstones of unit Tep 2 in the hanging wall (Fig. 4a). Samples are located between the 5000 ft level (1520 m) and 6000 ft level (1830 m), and from 930 ft (280 m) NE to 300 ft (90 m) SW of the CG vein. These samples include wall rocks, but not high-grade vein material. Geochemical analyses are included in Appendix A.

In mafic rocks (Tbg), major oxides show increases in SiO_2, K_2O, Fe_2O_3, MnO, BaO, P_2O_5 and decreases in Al_2O_3, CaO, and MgO as the CG vein is approached (Fig. 16a); trace elements show increases in Se, Mo, Zn, Pb, Ag, and S (Fig. 16b). In the peripheral potassic zone, NE of the vein (Fig. 7a), major oxides also show increases in Na_2O, K_2O, TiO_2, P_2O_5, MnO, BaO, and decreases in SiO_2, Al_2O_3, Fe_2O_3, and MgO with variable CaO; trace elements show increases in As, Sb, Hg, Tl, Mo, Se, Ag, and S.

In felsic host rocks, variations in major oxides and trace elements may be due to alteration and variations in original host rock lithology. Increases in SiO_2 in the footwall coincide with rhyolite of the June Belle formation (Tjb); relative decreases in the hanging wall correspond with volcaniclastic rocks of the Elko Prince formation (Tep). Increases also occur in the peripheral potassic zone, NE of the CG vein (Fig. 16c). Increases in Na_2O in the footwall and decreases in the hanging wall as the vein is approached show trends that are the opposite of K_2O which decreases in the footwall and increases in the hanging wall towards the vein. Slight increases in CaO as the vein is approached are present in the hanging wall. Slight increases in MgO towards the vein are present in the hanging and footwalls. Increases in P_2O_5, MnO, and BaO occur in the hanging wall and decreases in the footwall as the vein is approached. Trace elements show increases in As, Tl, and Mo in the hanging wall and decreases in the foot wall as the vein is approached (Fig. 16d). A relatively steady increase in Zn begins within 100 ft (30 m) of the vein in the hanging wall and continues at least 300 ft (91 m) into the foot wall (Fig. 16d); maximum values correspond with the intense potassic zone in the hanging wall and the potassic zone in the foot wall (Fig. 7a). Increases in Se occur at

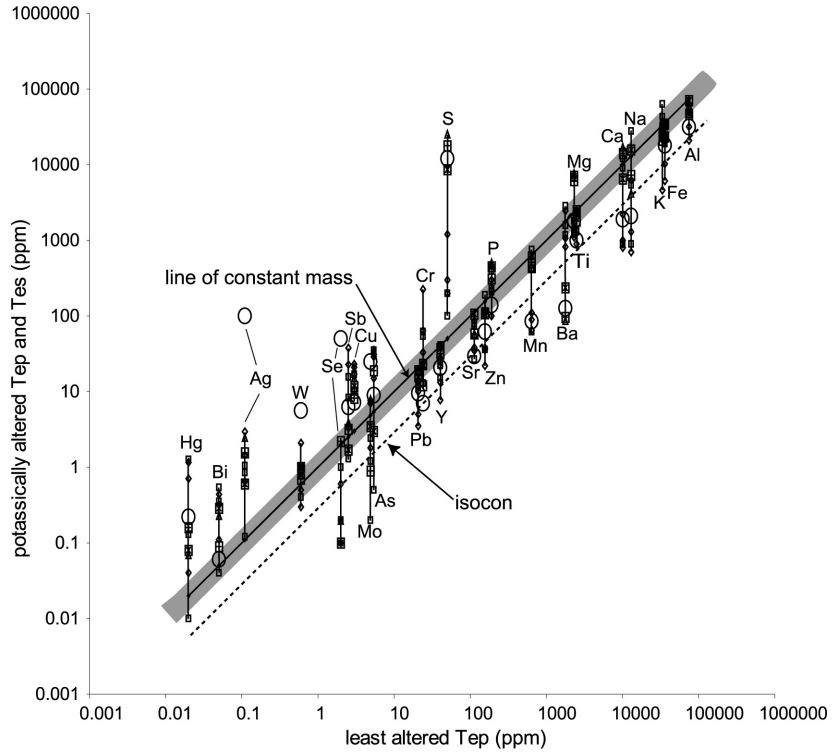

Figure 15a. Selected major, trace, and minor elements in potassically altered felsic volcaniclastic rocks (Tep and Tes) (y-axis) vs. least altered felsic volcaniclastic rock (Tep) from Midas district (x-axis). Dashed line is isocon determined from change in immobile elements; isocon lies outside of approximated variation associated with host rock compositions (gray bar). Gains and losses in elements measured from isocon.

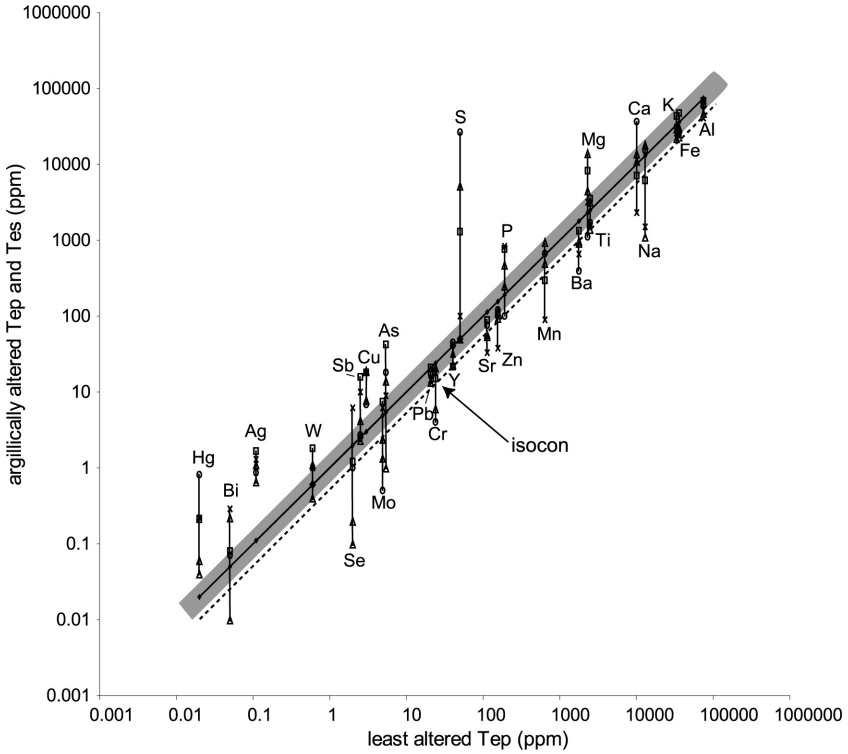

Figure 15b. Selected major, trace, and minor elements in argillically altered felsic volcaniclastic rocks (Tep and Tes) (y-axis) vs. least altered felsic volcaniclastic rock (Tep) from Midas district (x-axis). Dashed line is isocon determined from change in immobile elements; isocon lies slightly outside of approximated variation associated with host rock compositions (gray bar). Gains and losses in elements measured from isocon.

approximately 800 ft (240 m) NE of the vein within the peripheral potassic zone (Fig. 7a), and accompany increases in As, Hg, Sb, Zn, and S (Fig. 16d). The values of Se are relatively low, ~ 1 ppm, but represent an increase of almost ten times the values of samples closer to the CG vein. No increases in Se are present near the CG vein.

Variations in major and trace elements in sections 1400 N and 2600 N

Geochemical analyses for core from sections 1400 N and 2600 N, provided by Franco-Nevada, demonstrate that trace elements are zoned with respect to the CG and GC veins. Figures 17a–h are down-hole plots of geochemical analyses transferred onto geologic cross sections for 1400 N and 2600 N. The data have been smoothed using a running average of three samples; ranges of absolute values for raw data are indicated. Figures 18 and 19 are plots of geochemical analyses for vein intercepts plotted versus depth for each vein.

Ore grade veins extend from the 6000 ft level (1830 m), several hundred feet (~75 m) below the present-day surface, to at least the 4600 ft level (1400 m; Figs. 4a–b). The CG vein reaches ore grades of at least 0.25 opt (troy ounces per short ton) Au and 1.11 opt Ag between the 5400 and 5700 ft levels, and the GC vein approaches ore grades with grades of 0.23 opt Au and 0.11 opt Ag at the 6000 ft level (1830 m; Fig. 17a). Plots of vein intercepts for the CG vein in the 2600 N section versus elevation (Fig. 18a) show a sharp increase in Au and Ag and decrease in Ag:Au at the ~5400 ft level (1645 m). Similar plots of vein intercepts for the GC vein (Fig. 19a) show a sharp increase in Au and Ag at the ~6000 ft level (1830 m) with a decrease in Ag:Au, and fluctuations in both grades and ratios with increasing depth.

Typical pathfinder elements including Hg and As are moderately to highly enriched and form haloes above the tops of ore-grade veins. The highest values of Hg occur in the GC vein above ore-grade precious metals (Figs. 17c and 19b) with a maximum unsmoothed value of 35 ppm. These values decrease with depth along the vein. New ICP-MS data for core samples in section 1400 N show Hg haloes adjacent to the main veins that decrease in concentration laterally and with depth. The highest values of As occur in the CG vein and silicified faults in the hanging wall, above the level of ore-grade precious metals (Figs.17d and 18b). In both 1400 N and 2600 N, As anomalies along the main veins form haloes above ore-grade precious metals, and slightly below the highest Hg anomalies (Fig. 18b and 19b). In 1400 N, As is enriched near the present-day surface along the Colorado Grande fault, and within silicified siltstones along a hanging wall fault at slightly deeper levels. Several other weak anomalies at greater depth lie within and adjacent to peripheral potassic zones several hundred ft (~75 m) NE of the CG. Within veins Sb is weakly anomalous (to 22 ppm) slightly below the highest values of As, and just above, or coincident with, ore grade in the veins (Figs. 18b and 19b). Molybdenum anomalies are somewhat similar to those of As, and appear to be associated with hanging wall faults as well as the main veins (Fig. 17e). Molybdenum also appears variably enriched within the main veins at depth, and close to the present day surface within a potassically to argillically altered cap. Like the pathfinder elements and Mo, K exhibits enrichment near the present-day surface. It is also concentrated in the main veins, in haloes around the main veins, and within peripheral potassic zones (Fig. 17f).

Base metals exhibit variable enrichment and depletion in veins, and do not show marked increases with depth. The highest values of Cu occur in the main veins (Fig. 17g). Copper is more abundant in mafic rocks (Tbg) than other rock units. The highest values of Zn (886 ppm) occur within the GC vein approximately 300 ft (~91 m) below the surface, slightly below the zone of anomalous precious metals, in section 2600 N (Figs. 17h and 19c). In this zone, the vein is hosted by mafic rocks (Tbg), and is not ore-grade. Beneath this Zn anomaly, grades of precious metals increase dramatically in felsic host rocks. Overall, Zn appears to form haloes adjacent to the main veins; within veins the highest values are above the level of high-grade ore (Figs. 17h, 18c, and 19c). Zn is commonly depleted within the main ore-grade portion of veins, and enriched in adjacent wall rocks.

Geochemical variations in drill hole MKC-202

A nearly complete set of pulps from drill hole MKC-202 provided the opportunity to assess a more continuous set of samples surrounding the CG vein using more sensitive geochemical techniques. The hole was collared 1500 ft (457 m) NE of the CG vein, at the 5930 ft level (1807 m); it dips 63° SW, and extends approximately 2425 ft (740 m), crossing the vein at the 4200 ft level (1280 m; Fig. 4a). Thirty-nine samples of pulps from the hole were analyzed using tri-acid digestion and ICP-MS analytical techniques described previously; results are included in Appendix A. Resultant geochemical anomalies in this hole are similar to those described for older geochemical data for section 1400 N described above. Anomalies in the hanging wall occur in the peripheral potassic zone between the 5000 ft (1520 m) to 5300 ft (1620 m) levels. In this zone, marked increases in Se, As, Sb, Hg, Tl, S, Zn, Pb, Mo, W, Ca, and a very weak increase in Ag are accompanied by decreases in Mg, Na, Ca, Mn, and Fe. Closer to the CG vein, a Ag-Hg anomaly forms a halo above increased Se, As, Tl, Sb, Ag, S, Ca, and decreased Fe, and Mn. The presence of the CG vein (4200 ft level or 1280 m) is marked by increased Ag, Se, Sb, Tl, Fe, Mn, Cu, Mo, As, Hg, S, and W in the wall rocks. As, Hg, S, and W display weaker increases than anomalies in the shallower peripheral potassic zone. Overall, Ag, Pb, Zn and Mo show increased concentrations with depth, and towards the CG.

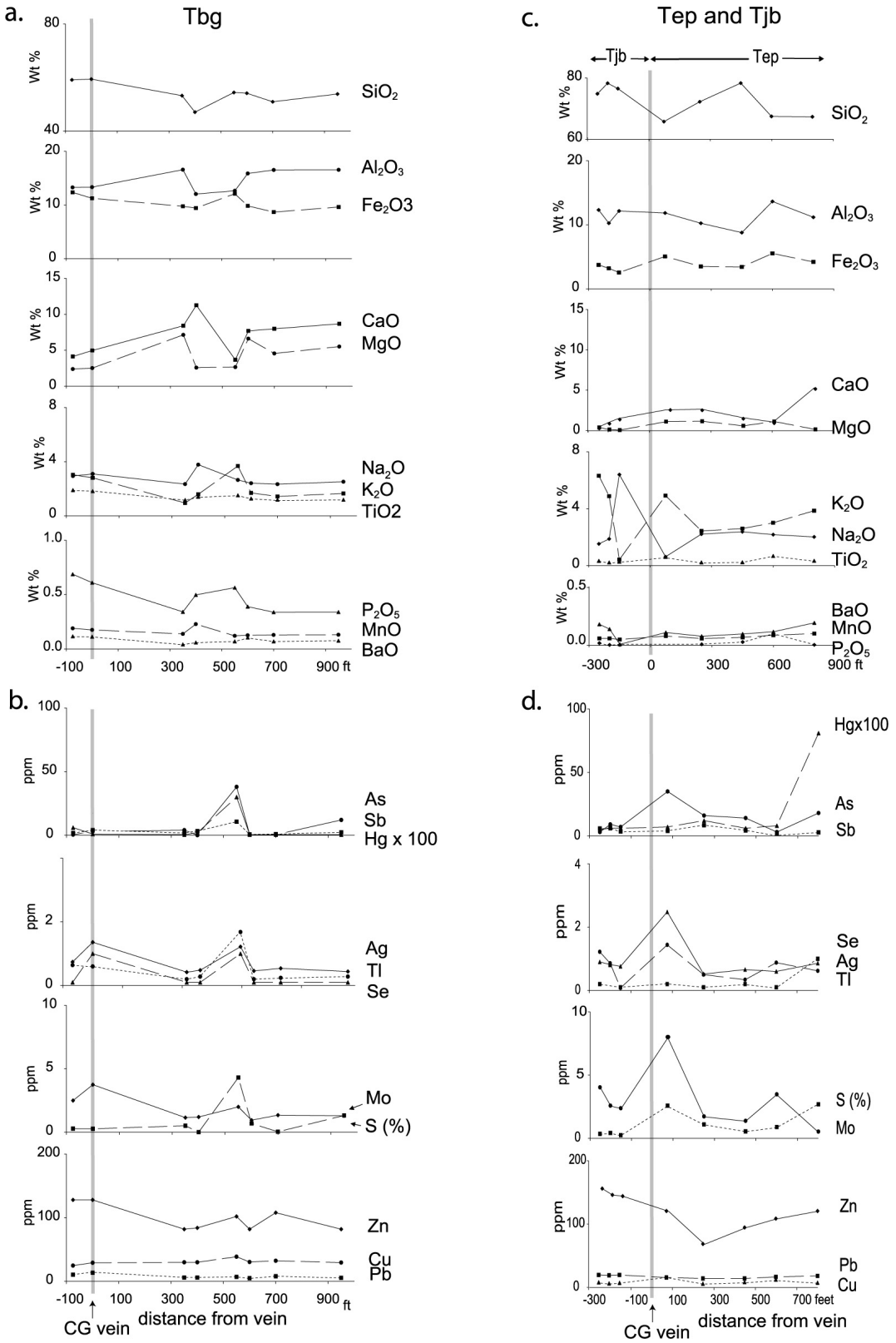

Figure 16. Plots of major oxides and trace elements in host rock samples between 5000 and 6000 ft elevation vs. distance from CG vein, 1400 N. a) Major oxides in Tbg; b) trace elements in Tbg; c) major oxides in Tep and Tjb; d) trace elements in Tep and Tjb. Location of Colorado Grande (CG) vein—gray vertical line.

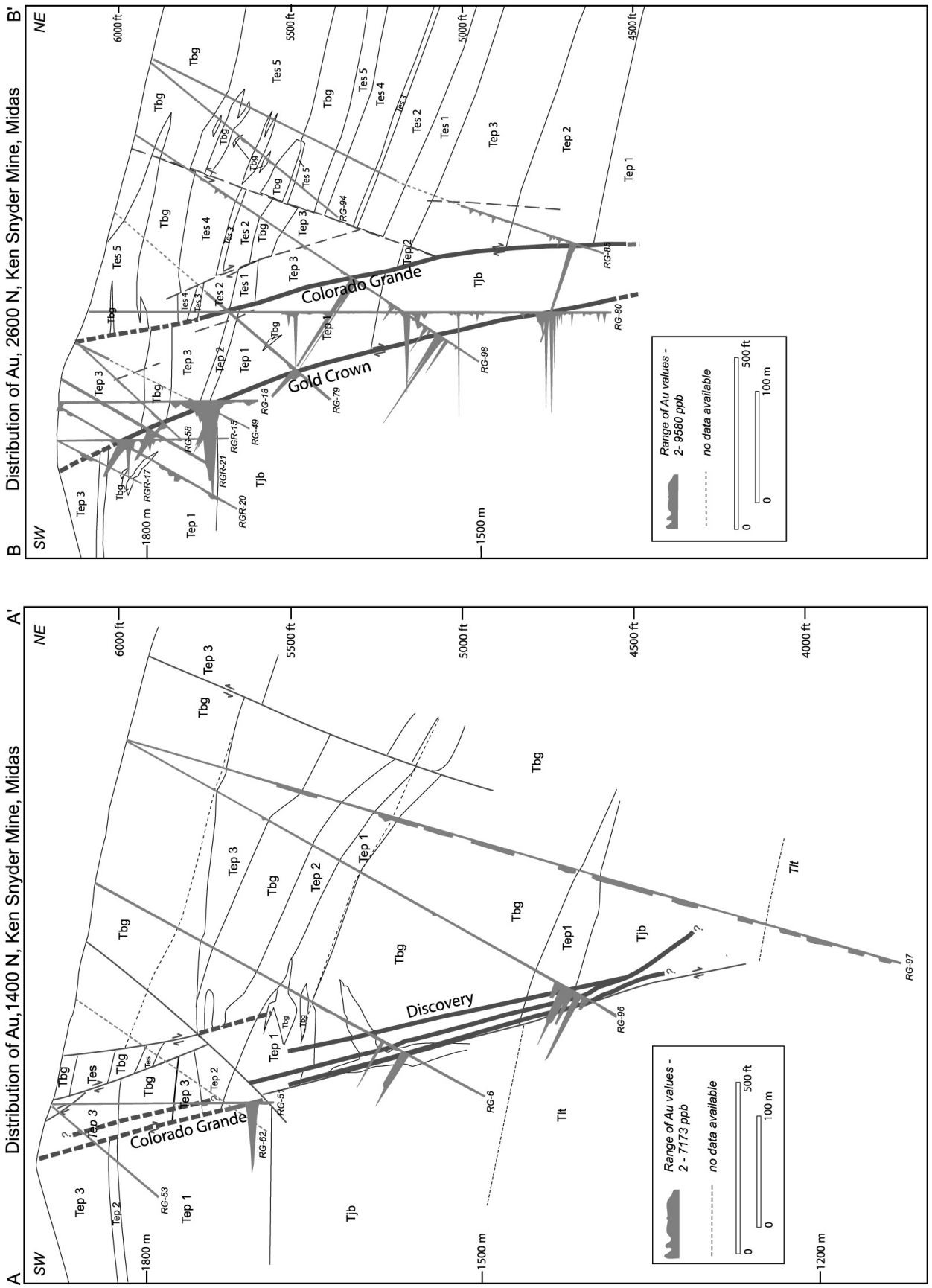

Figure 17a. Distribution of Au in core in cross sections, 1400 N and 2600 N (locations shown on Fig. 3). Data smoothed using running averages of three samples; range of data indicated on figures.

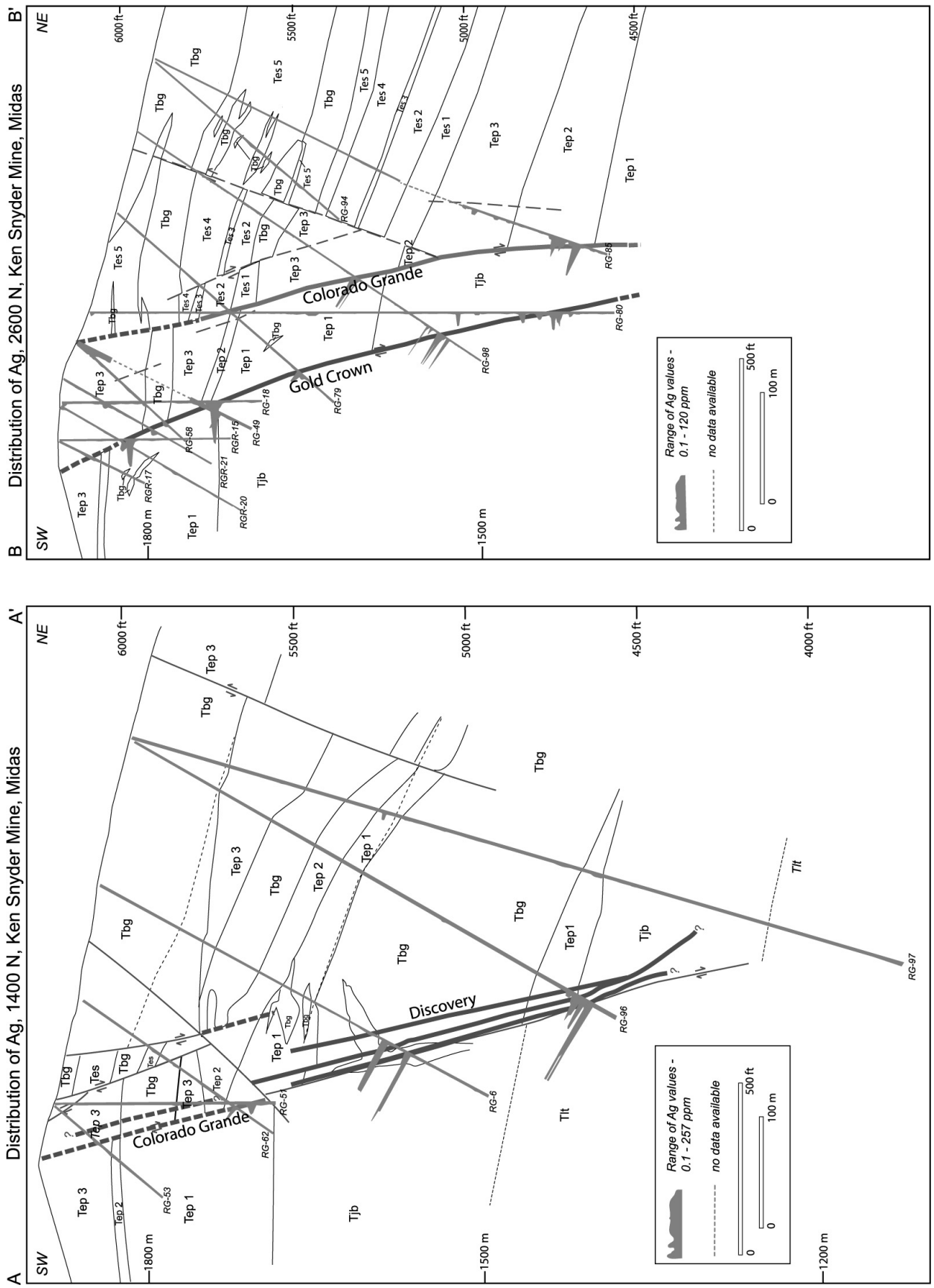

Figure 17b. Distribution of Ag in core in cross sections, 1400 N and 2600 N (locations shown on Fig. 3). Data smoothed using running averages of three samples; range of data indicated on figures.

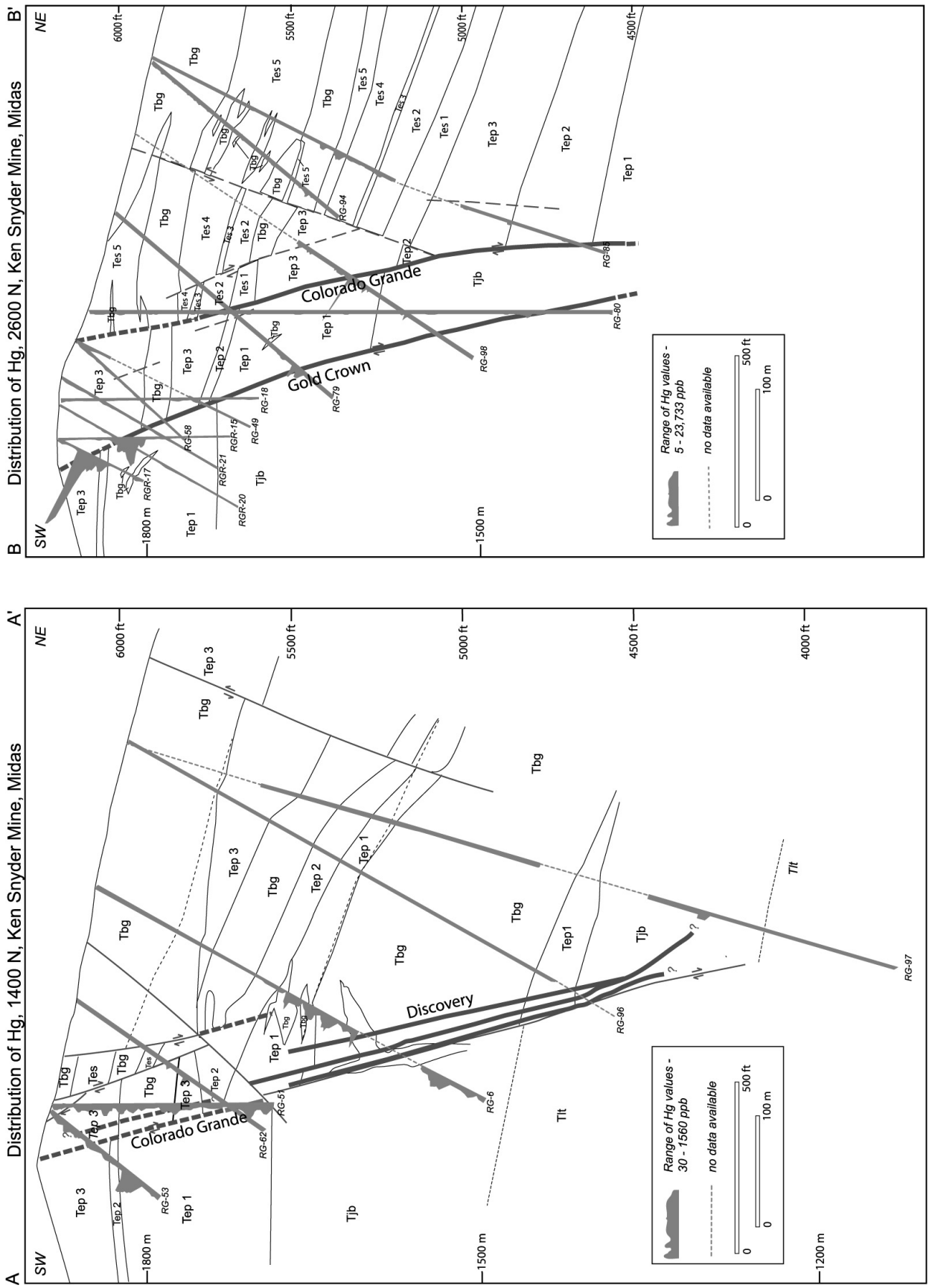

Figure 17c. Distribution of Hg in core in cross sections, 1400 N and 2600 N (locations shown on Fig. 3). Data smoothed using running averages of three samples; range of data indicated on figures.

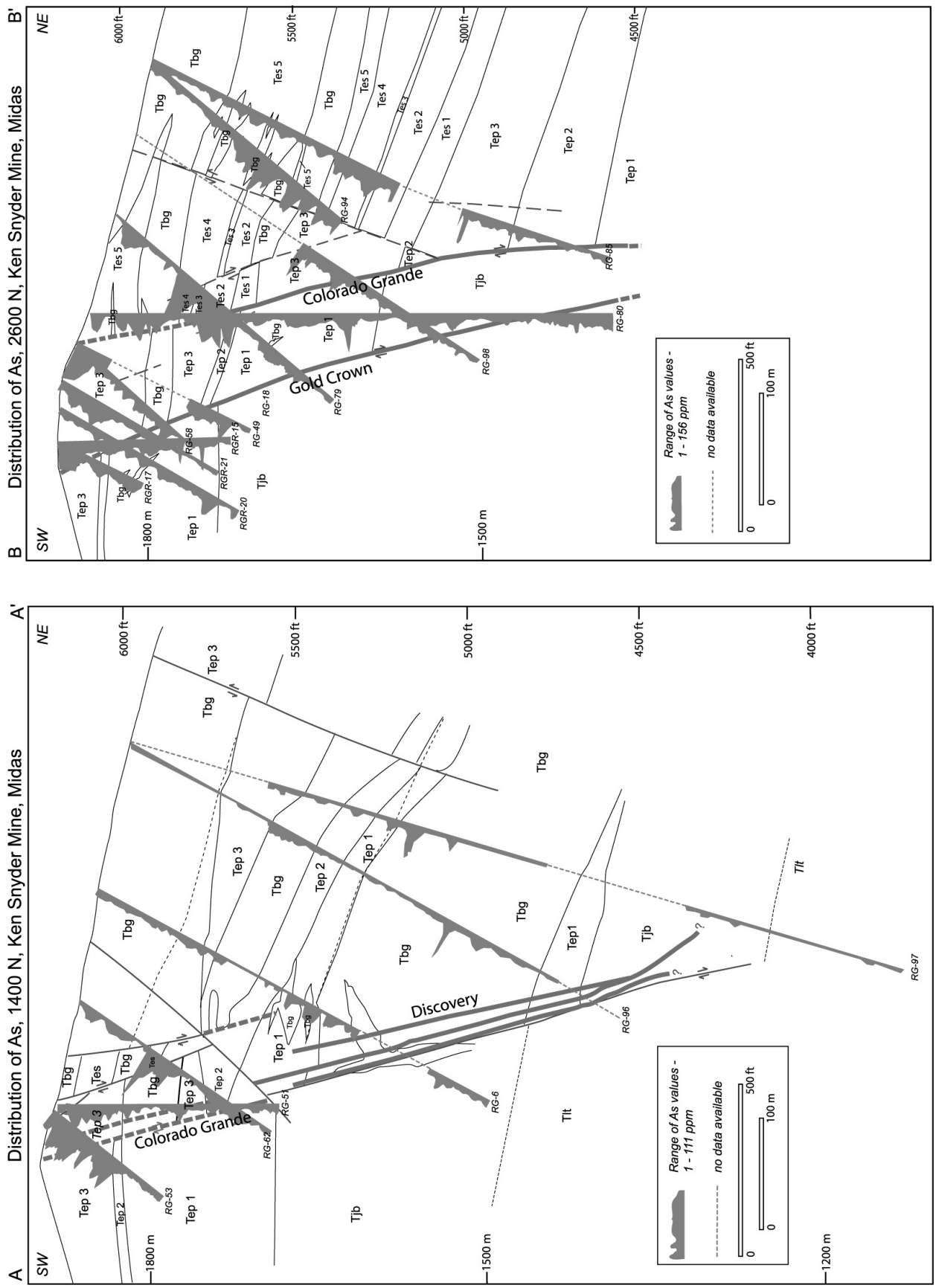

Figure 17d. Distribution of As in core in cross sections, 1400 N and 2600 N (locations shown on Fig. 3). Data smoothed using running averages of three samples; range of data indicated on figures.

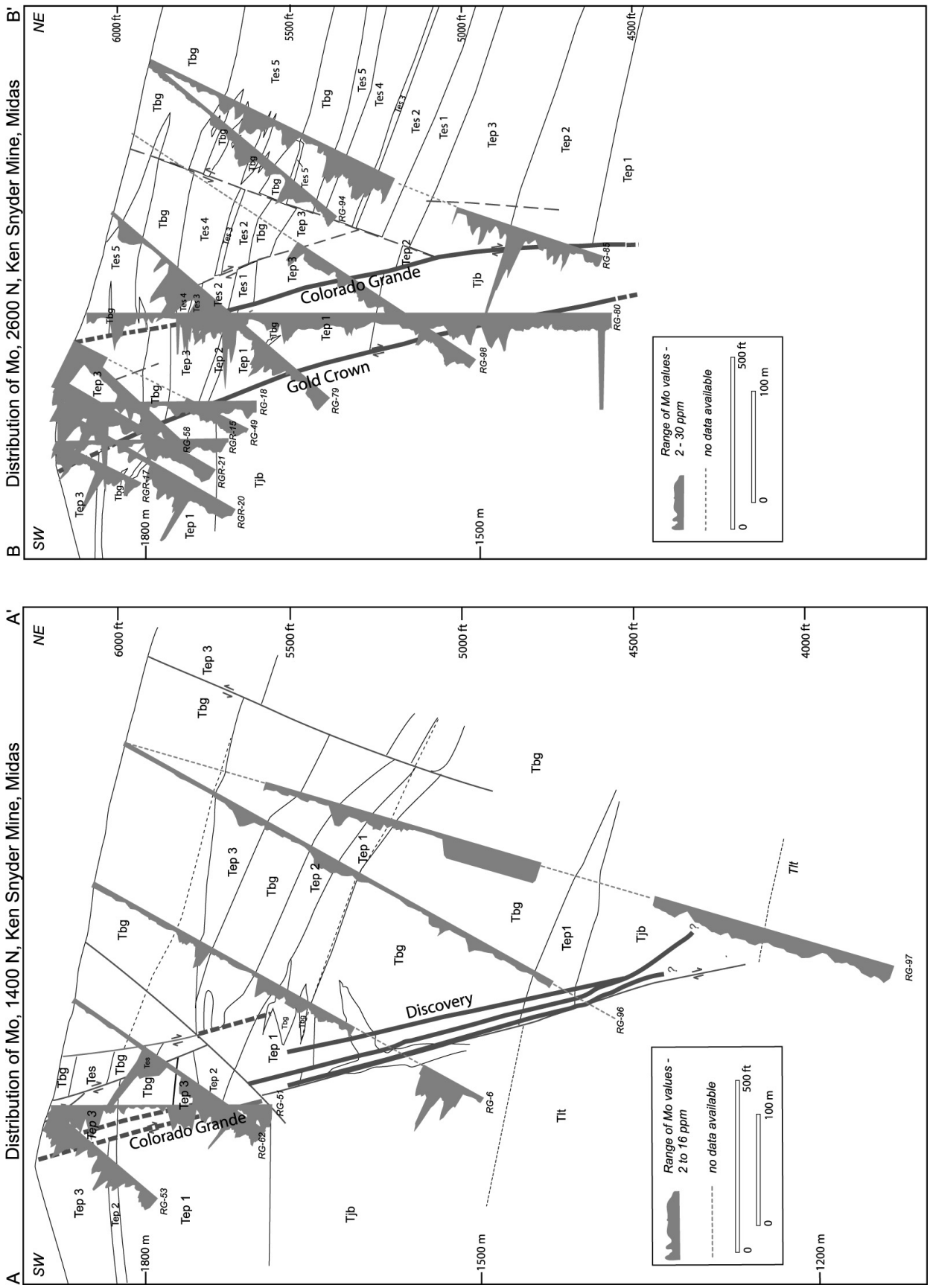

Figure 17e. Distribution of Mo in core in cross sections, 1400 N and 2600 N (locations shown on Fig. 3). Data smoothed using running averages of three samples; range of data indicated on figures.

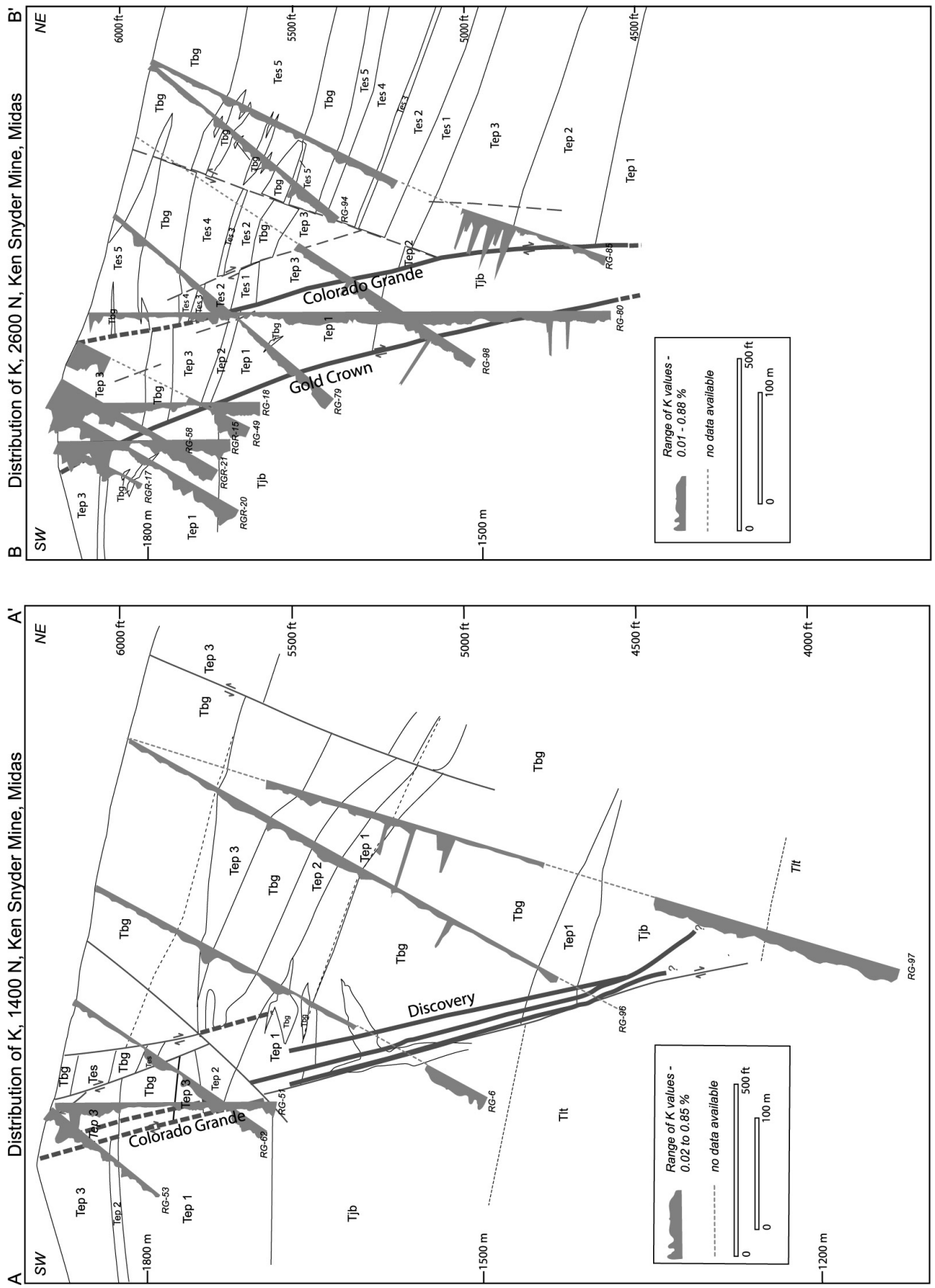

Figure 17f. Distribution of K in core in cross sections, 1400 N and 2600 N (locations shown on Fig. 3). Data smoothed using running averages of three samples; range of data indicated on figures.

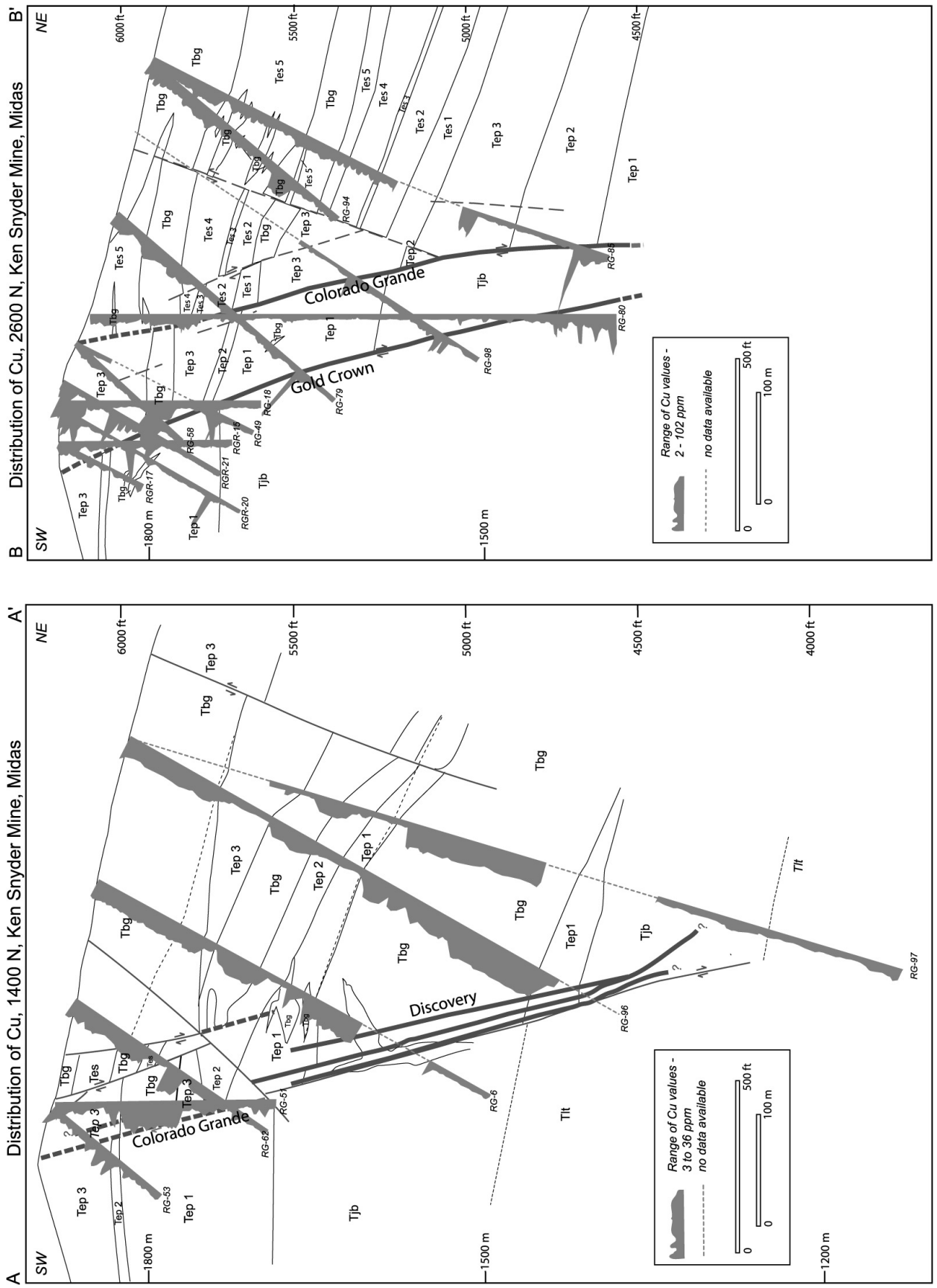

Figure 17g. Distribution of Cu in core in cross sections, 1400 N and 2600 N (locations shown on Fig. 3). Data smoothed using running averages of three samples; range of data indicated on figures.

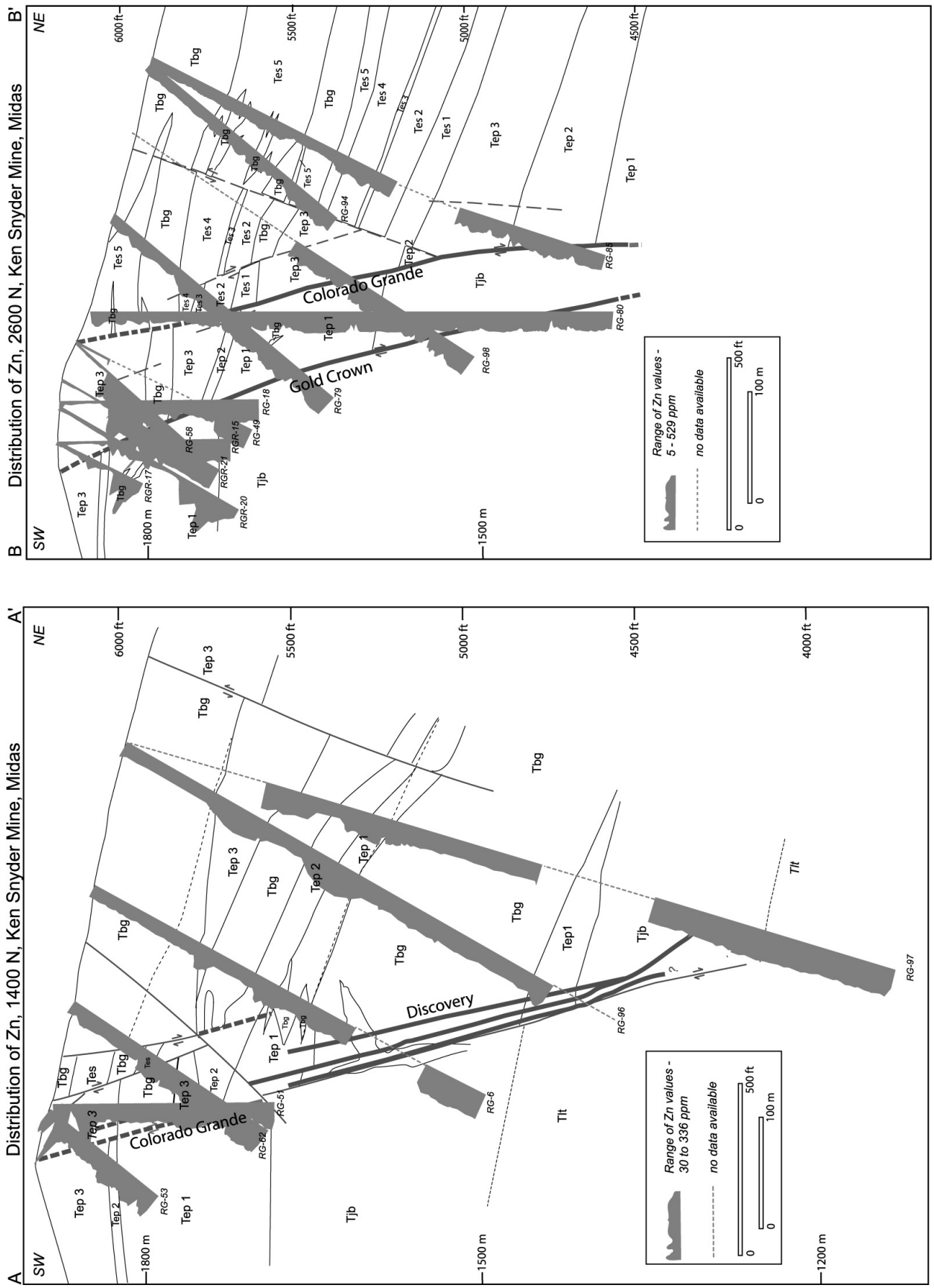

Figure 17h. Distribution of Zn in core in cross sections, 1400 N and 2600 N (locations shown on Fig. 3). Data smoothed using running averages of three samples; range of data indicated on figures.

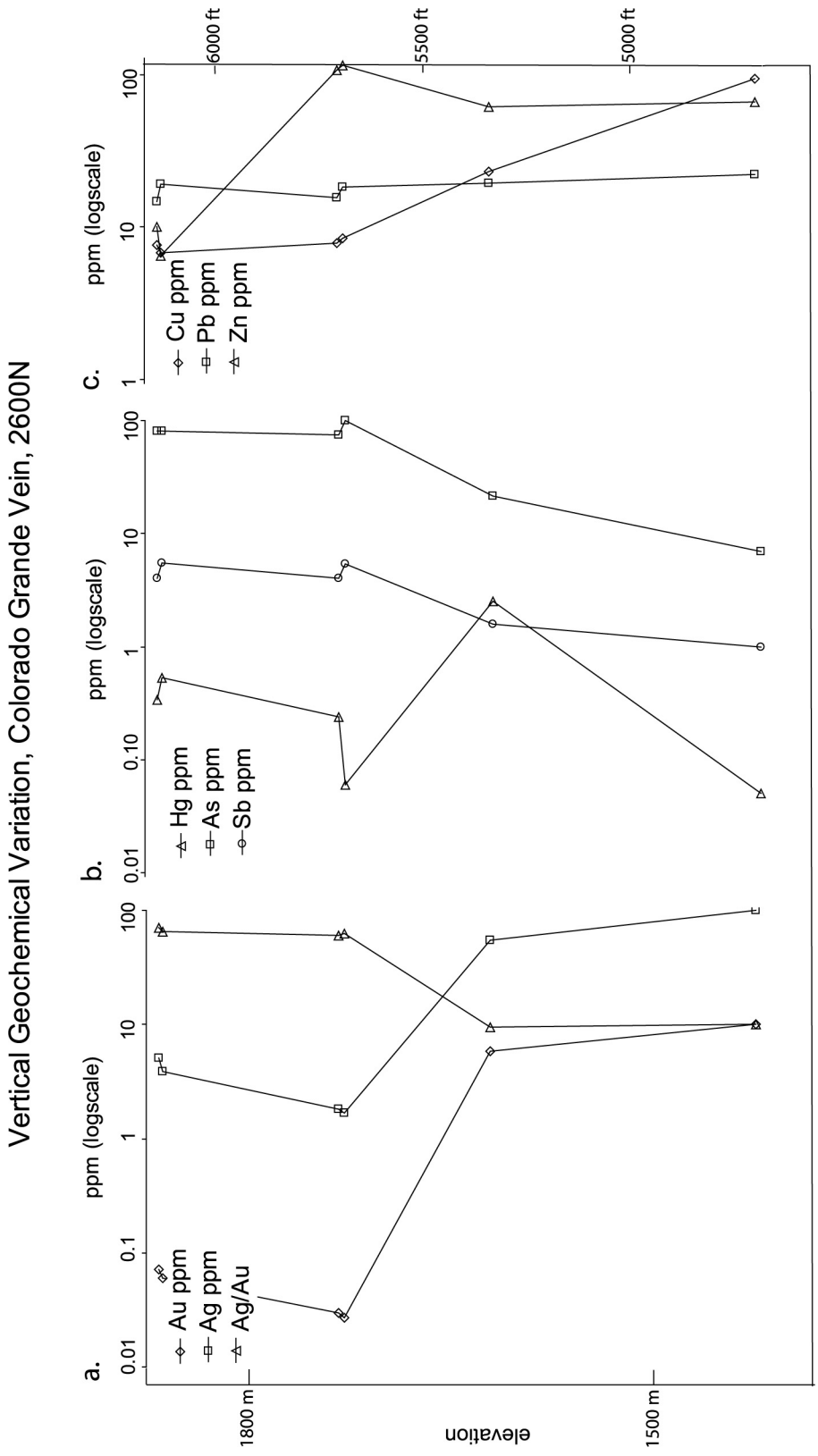

Figure 18. Colorado Grande vein intercepts vs. elevation, 2600 N. Elements include a) Au, Ag, and Ag/Au; b) Hg, As, and Sb; and c) Cu, Pb, and Zn. Geochemical analyses from Franco-Nevada.

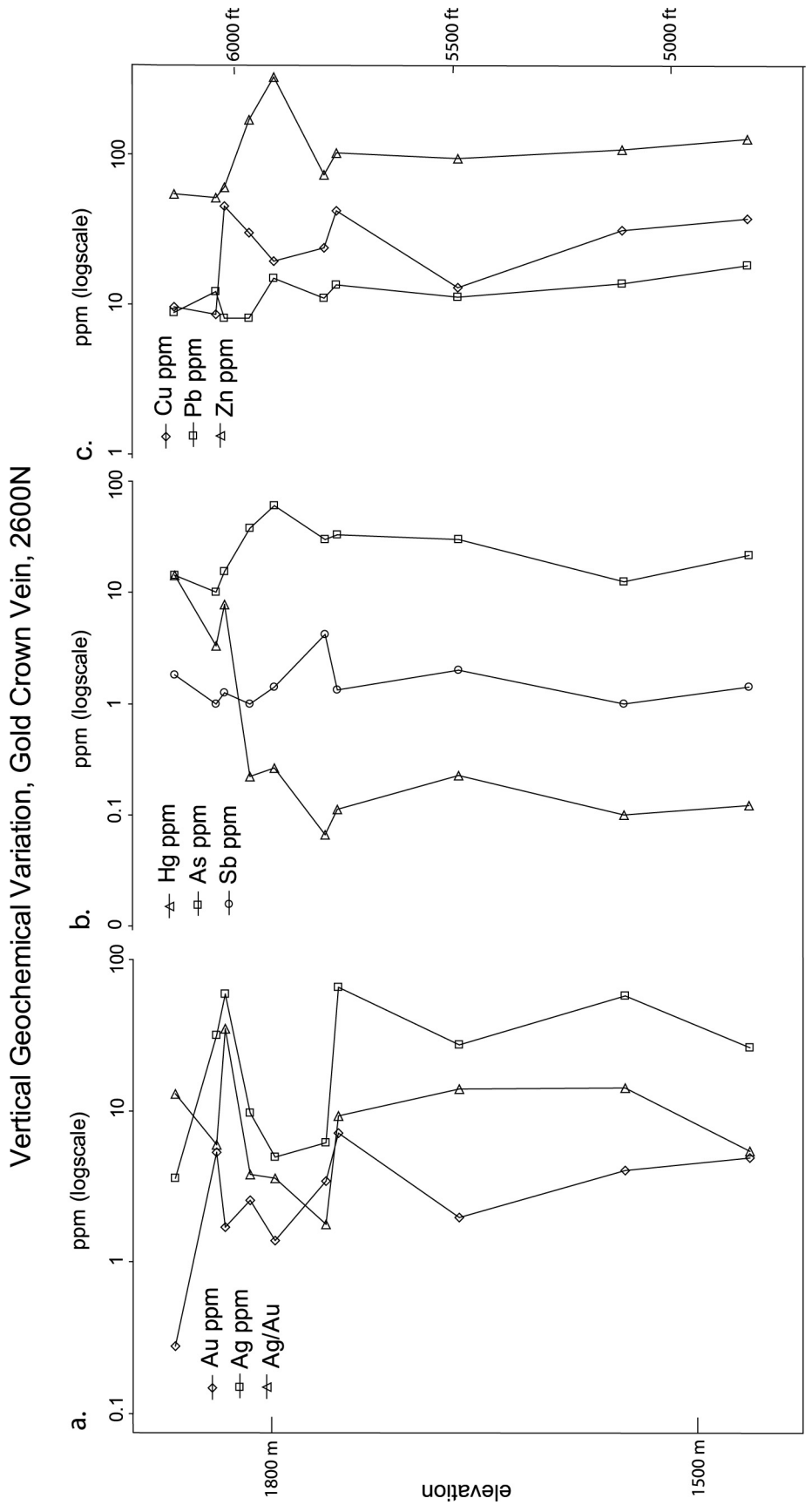

Figure 19. Gold Crown vein intercepts vs. elevation, 2600 N. Elements include a) Au, Ag, and Ag/Au; b) Hg, As, and Sb; and c) Cu, Pb, and Zn. Geochemical analyses from Franco-Nevada.

Surface transect across Colorado Grande vein

A suite of five rock chip samples was collected from exposures of the hanging wall, CG vein, and footwall in a road cut at approximately 600 N (Section C–C′, Fig. 3) where the location of the vein was well-constrained from earlier mapping and sampling (P.M. Goldstrand, unpublished mapping, 1999). In outcrop, the rocks are deeply weathered. Petrographic work confirms that weak argillic alteration has overprinted potassic alteration. Despite the supergene weathering and argillic overprint, these samples exhibit variations in trace elements similar to those observed in core described above. Increases in Ag, As, Tl, Sb, S, Mo, K, and Hg occur at the marked location of the vein. The highest values of Se occur in the hanging wall 20 ft (6 m) east of the vein. Increases in Cu, Fe, Co, Ni, V, and Cr occur 50 ft (15 m) into the footwall coincident with mafic rocks (Tbg), and reflect the influence of lithology on anomalies. Zinc is depleted within the vein and enriched in the wall rocks.

HYDROTHERMAL MINERAL GEOTHERMOMETRY

Delineation of paleoisotherms using temperature-sensitive minerals can be used to establish pathways of paleofluid flow (Hedenquist et al., 2000). Knowledge of the paleohydrology is particularly important in epithermal systems where locations of the main veins or upflow zones are unknown. The main upflow zones of active systems are usually in the hottest, most permeable portions, and are reflected in upward sloping, closely spaced isotherms. Boiling within these zones may result in deposition of precious metals (Simmons and Browne, 2000). Temperature-sensitive minerals such as clays and calc-silicates are commonly used to establish the thermal structure of fossil and active hydrothermal systems (Steiner, 1968; Browne and Ellis, 1970; Horton, 1985; Reyes, 1994; Simmons and Browne, 2000; Simpson et al., 2001). The distribution of these minerals at the Ken Snyder mine is summarized in Tables 2a–b, and shown in Figures 7a–b and 8a–b. More detailed discussion of these minerals and comparison to other low-sulfidation systems is presented here.

Clays

In many low-sulfidation hydrothermal systems, illite is located in the hottest portions of the system; it grades outwards through illite/smectite (I/S) to smectite in cooler distal portions (Steiner, 1968; Browne and Ellis, 1970; Horton, 1985; Simmons and Browne, 2000; Simpson et al., 2001). However, at Midas, clays do not demonstrate this type of zonation over a broad zone (Leavitt et al., 2000). Illite is present in trace amounts, and is restricted to the main vein zones, adjacent wall rocks, and locally within the banded veins. In contrast, smectite, commonly Ca-montmorillonite, is widely distributed, and persists close to the main veins where temperatures of the hydrothermal fluids were likely ≥200ºC, suggesting montmorillonite was metastable in this zone. Although smectite is generally stable to ~200ºC, its extended stability at higher temperatures may be due to relatively high Ca/K (Deer et al., 1975) and/or silica concentrations in the fluids (Reed, 1997). The abundance of K associated with the main veins argues against K-depleted fluids at this stage. However, outside of the main structures, and during earlier and later stages of alteration, smectite stability may have been enhanced by Ca derived from alteration of the mafic rocks. In the Broadlands-Ohaaki geothermal system, measured temperatures of hydrothermal water do not show a good correlation with the compositions of interlayered clays, and reaction kinetics are thought be the likely cause, rather than temperature or lack of K (Simmons and Browne, 2000).

Reconnaissance analyses of clays for this study suggest that compositions of chlorites vary with distance from upflow zones. Qualitative SEM analyses show a shift in Mg:Fe ratios from approximately 3:1 in propylitically altered basalts, ~1000 ft (300 m) from the main veins, to 3:2 in volcaniclastic rocks, 150 to 300 ft (45 to 90 m) from the main veins, to 1:2 in potassically altered rhyolites adjacent to the main veins. The latter rocks contain emerald-green chamosite, a Fe-rich chlorite. Microprobe analyses confirm that emerald-green chlorites at Midas are Fe-rich, and compositions may vary with distance from the main veins (Appendix C). Similar compositional shifts in chlorite have been described for the Topia district (Loucks et al., 1988). At the Golden Cross epithermal deposit, thermally unstable chlorites give way to thermally stable chlorite with depth and proximity to veins (Simpson, 1996). Transitions from smectite to chlorite (rather than illite) with increased temperature have been documented in mafic volcanic-hosted hydrothermal systems. In geothermal systems in Iceland hosted by basalt, smectite is replaced by mixed-layer clay minerals and swelling chlorites between 200º to 230ºC (Kristmannsdottir, 1978; Arnórsson et al., 1983; Hutcheon et al., 1994); chlorites are the dominant sheet silicate above 240ºC (Kristmannsdottir, 1978). In a study of the Newberry Volcano in Oregon, a progression of smectite to randomly interstratified chlorite-smectite (C/S) to ordered interstratified C/S to chlorite takes place over a temperature range of about 150º to 265ºC in mafic volcanic rocks. Electron microprobe analyses indicate that the Mg:Fe composition of the mixed-layer C/S was approximately 2:1, and shifted in the chlorites to approximately 0.8:1 (Bargar and Keith, 1999).

Along the main veins, illite is more common at levels above approximately the 5250 ft level (1600 m), though still present only in trace amounts, and is joined by Fe-rich chlorite at depth. A vertical zonation from illite to chlorite-illite with depth has been described for other epithermal systems including Golden Cross (de Ronde and Blattner, 1988) and Hishikari (Isawa, et al., 1990). Similar zonations are observed in active low-sulfidation systems such as Palinpinon (Reyes, 1990; Reed, 1994), and the New Zealand geothermal fields where illite and chlorite is the typical clay assemblage above ~220ºC (Browne, 1978). The homogeneous nature of host rocks in the New

Zealand examples suggests that temperature is the primary control on this transition (Browne, 1978; de Ronde and Blattner, 1988). An additional control may be fluid composition and the abundance of Fe relative to K. Close to the main faults at the Ken Snyder mine, bulk rock geochemistry indicates an increase in Fe within the intense potassic alteration zone.

The utility of chlorite composition as a geothermometer has not been proven (de Caritat et al., 1993; Jiang et al., 1994; Hutcheon, 1994). In general, compositional changes in chlorite/smecites are discontinuous, not well known, nor easily determined with XRD analytical procedures compared to those of the I/S group (Moore and Reynolds, 1997). Compositional changes are not clearly related to changes in temperature, and could also be due to changes in fO_2 (Hutcheon et al., 1994) or host-rock composition (Cathelineau and Nieva, 1985; Bevins et al., 1991). Although causes of variable chlorite compositions remain unclear, the presence of Fe-rich chlorites seems to provide an empirical means of locating the upflow zone and relative depth within the potassic zone at Midas.

Calc-silicates

Within propylitic assemblages at Midas, calc-silicate minerals demonstrate increasing temperatures of alteration towards the main veins. Epidote and prehnite indicate temperatures of 250ºC (Browne and Ellis, 1970; Browne, 1978; Reyes, 1990; Simmons and Browne, 2000). The epidote isograds drape over the major veins, evidence that the veins were deposited in the hotter upflow zones (Reyes, 1990; Reed, 1994).

In addition to temperature, calc-silicates provide evidence of the CO_2 content of the fluids (Henley and Hedenquist, 1986). At Midas prehnite occurs in intense propylitic zones at depth, and in potassic alteration zones at shallower levels; in both areas it is ≥ 500 ft (150 m) from the main veins. Prehnite forms under extremely low concentrations of CO_2, and relatively high concentrations of Ca^{2+}. At higher concentrations (> 0.01 molar at 200ºC) calcite would be the stable phase rather than prehnite (Simpson, 1996). Prehnite may have formed from fluids depleted in CO_2 as a result of boiling (Browne and Ellis, 1970). An alternative explanation is that the prehnite formed from CO_2-depleted fluids unrelated to those that formed the main veins. Prehnite has not been observed closer than ~500 ft (150 m) adjacent to the main veins where fluids were enriched in CO_2 during formation of ore.

PALEOSURFACE AT MIDAS

Recognition of the paleosurface of an epithermal system is an important tool in understanding the pathways of fluid flow during the formation of high-grade veins, as well as in understanding the locus of metal deposition. Surface gradients, faults, geologic contacts, and lithologic permeabilities controlled hydrothermal fluid flow. The combination of geologic reconstructions, data from fluid inclusions, geochemistry, and patterns of alteration provide evidence for the location of upflow and outflow zones, and areas most likely to host high-grade ore.

Geologic reconstructions

A NE-SW striking district-wide geologic cross section, which includes section 2600 N (Fig 7b), shows that the paleosurface was approximately 1000 ft (~310 m) above the present-day surface, and located at the 7200 ft level (2200 m) near the intersection of the GC and CG faults. The top of productive high-grade mineralization formed from 1200 ft (370 m; Gold Crown vein, 2600 N) to 1600 ft (~490 m; Colorado Grande vein, 1400 N) below the paleosurface. As described above, the shallowest portion of the epidote isograd coincides with the tops of high-grade veins and the isograd deepens to the south along the vein (Figs. 7a–b). No data are available to indicate trends further north. The paleodepths of the epidote isograds are similar to depths of epidote isograds mapped in active, low-sulfidation geothermal systems in the Philippines (Reyes, 1990) and probably represent isotherms of approximately 240° to 250°C. The depth/temperature relationship indicated by the presence of epidote is consistent with the depth/temperature relationship (geotherm) described for low-sulfidation epithermal systems elsewhere, assuming hydrostatic conditions (Buchanan, 1981). However, the deepest levels of boiling and precious metal horizons are significantly deeper than those shown in generalized models of an epithermal system under hydrostatic conditions (e.g., Buchanan, 1981). This increased depth of the boiling/metal horizons may be due to high dissolved gas contents in the fluids (Hedenquist and Henley, 1985; Cooke and Simmons, 2000), and/or to pressures greater than hydrostatic (Buchanan, 1981).

Fluid inclusions

Several studies of fluid inclusions from quartz-adularia-calcite veins from the Midas district and Ken Snyder mine have been carried out, the results of which are summarized here. These studies show that GC and CG veins formed at minimum temperatures ranging from approximately 200º to 260ºC; salinities generally were low, indicating a dominance of meteoric water.

Blair (1991) conducted a study of fluid inclusions from 22 sections from 7 veins from throughout the Midas district; only 9 sections contained inclusions large enough for study. Temperatures of homogenization (T_h) ranged from 192º to 314ºC, with a mode of 240ºC. T_h of 12 inclusions in quartz from the GC vein ranged from ~220º to 260ºC; salinities ranged from 0.35 to 1.05 weight percent NaCl equivalent (wt.% NaCl eq.). Coexisting liquid-rich and vapor-rich inclusions indicate that boiling took place. The calculated depths of formation were 1100 ft (340 m) for the GC vein, and 1540 ft (470 m) for the Amethyst vein, ~300 ft (90 m) south of the CG vein. These results indicate a paleowater table elevation at the ~ 7200 ft level (2200 m) in the

GC area, and 6990 ft level (2130 m) in the Amethyst vein area; these indicate a southward deepening of the water table in the district. Temperatures determined by Smith (1997; Goldstrand and Schmidt, 2000) were similar. Six fluid inclusions from the Colorado Grande vein indicated temperatures ranging from 220º to 260º C, with an average T_h of 246±15º C; salinities ranged from 6 to 26.4 wt.% NaCleq., with the latter measurement potentially erroneous.

J.L. Mauk and M.P. Simpson (unpublished report, 2002) examined 19 vein samples from the Midas district, including veins at the Ken Snyder mine. The district-wide average T_h for 10 quartz veins ranged from 199° to 266°C. T_h ranged from 203° to 234°C for fluid inclusions from 3 samples of quartz from the GC and CG veins; salinities ranged from <0.2 to 2.9 wt.% NaCl eq. T_h ranged from 179° to 246ºC for a single calcite crystal from the CG vein, and contained pure water. T_h ranged from 124° to 161°C for rare inclusions from late amethyst in the CG vein (probably Stage V). The elevations of the paleowater table were estimated using calculated formation pressures and depths. Formation depths were determined using the hydrostatic boiling point for depth curves of Haas (1971), and required the assumption that fluids were boiling. Mauk and Simpson's study shows that the paleowater table sloped from north to south from a high point at the ~7935 ft level (2420 m), approximately 2 km NNW of the Ken Snyder mine at the Miners Gold prospect (1535 ft or 470 m of erosion), to a low at the ~6200 ft level (1890 m) in the vicinity of the Snow White vein and southern CG. A surface sample of the GC vein close to the intersection with the CG vein yielded an elevation for the water table of 7190 ft (2190 m) that seemed to be anomalously high relative to the overall southward slope of the paleowater table. The elevations and overall slope of the paleowater table are similar to those determined from Blair's data. This slope is based on the assumption that either the water table geometry stayed constant through the lifetime of the vein, or that the samples taken were from the same stage. Because all fluid inclusions studied by Mauk and Simpson were secondary, the authors urged caution in interpreting the data. However, in general, their temperatures are consistent with those determined by Blair (1991) and Smith (1997).

Paleohydrology

The combined evidence from secondary minerals, geologic reconstructions, and fluid inclusions indicate that the GC fault was the area of maximum upflow near its intersection with the CG vein. The distribution of alteration minerals, particularly epidote, shows that temperatures decrease away from this intersection. Fluid inclusion data from surface samples of the GC vein at this location indicate that the paleowater table was at the ~7200 ft level (2200 m), the same elevation as the paleosurface estimated from geologic reconstruction; in other words, the water flowed out onto the surface probably forming a hot spring in this area. At this location, the top of ore grades in the GC vein is 600 ft (180 m) higher than in the CG vein. The paleowater table, tops of ore-grade veins, and the epidote isograd all dip away from this upflow zone. As described by Rhys (unpublished report, 2002), a component of N-S left-lateral fault movement during mineralization, as observed along the CG fault, simultaneously produced extensional movement along the GC fault. Therefore, the GC conduit was highly permeable, allowing for maximum upflow of hydrothermal fluids. In contrast, the Colorado Grande fault experienced local retardation of ascending fluids.

EVOLUTION OF THE HYDROTHERMAL SYSTEM

Characterization of hydrothermal alteration and ore paragenesis shows that the Midas hydrothermal system evolved from regional deuteric alteration through progressively hotter stages of alteration culminating in formation of high-grade veins. Table 5 summarizes mineral and chemical changes accompanying alteration. During early deuteric alteration, the presence of chlorite and calcite along shallow-dipping fractures and veinlets suggests that fluid flow was dominantly lateral. Chemical reactions were largely isochemical, but included an influx of volatiles including CO_2 (e.g., formation of calcite from plagioclase) and H_2O (e.g., formation of chlorite from ferromagnesian minerals). As the hydrothermal system developed, H_2S-bearing fluids and increased water:rock reactions resulted in moderate propylitic alteration (Table 2). Steeply-dipping cross-cutting veinlets indicate that fluid flow along fractures had a stronger vertical component than did the earlier deuteric fluids. The presence of chlorite and pyrite suggests temperatures ≥ 200°C (Arnórsson et al., 1983). Additional CO_2 and H_2O produced greater quantities of calcite, smectite, and chlorite. Addition of S caused sulfidation of ferromagnesian minerals, particularly along faults and fractures. Typical pathfinder elements including Ag, As, Sb, and Hg were likely transported as bisulfide complexes, and deposited with S (Henley and Hedenquist, 1986). The slight increase in Zn may reflect transport by sulfide complexes, or hydroxy-carbonate complexes (Henley and Hedenquist, 1986), and precipitation after sulfidation (e.g., sphalerite rims on pyrite). The transition to intense propylitic with the formation of epidote ± prehnite indicates an increase in temperature to between 240º to 250°C. Cross-cutting veinlets suggest that intense propylitic alteration locally overprinted moderate propylitic alteration.

Potassic alteration corresponds to increased abundance of adularia, as replacement of feldspars and groundmass in both mafic and felsic rocks, possibly coincident in time with later stages of propylitic alteration. The presence of epidote ± prehnite within the potassic zone suggests that temperatures of fluids were similar to those in intense propylitic zones. Both mafic and felsic volcaniclastic rocks show an increase in K content; rhyolites of Tjb and Tlt show a slight loss or no change in K. Zinc is moderately correlated with K ($0.5 \leq r^2 < 0.6$), and reflects the increased abundance of sphalerite in potassically altered rocks

TABLE 5. SUMMARY OF MINERAL AND GEOCHEMICAL CHARACTERISTICS OF ALTERATION.

Lithology/Units	Alteration	Elements enriched	Elements depleted	Main alteration minerals	Analyses
Mafic/basalt Tbg	Propylitic	S, volatile elements, P, Zn, As, Sb, Ag, Hg ± Sr, Cr, Pb, Se	Mg ± Ca, Sr, Cr	chlorite, calcite, pyrite, smectite, ± epidote, quartz, albite	9
	Potassic	K, S, volatile elements, P, Pb, As, Sb, W, Ag, Se, Hg	Ca, Mg, Cr ± Na, Sr	chlorite, adularia, smectite ± illite, pyrite/marcasite, quartz	7
	Argillic	S, Hg, Sb, W ± P, Y	Ca, Mg, Sr, Cr ± Al, K	smectite, calcite, kaolinite, pyrite, ± chlorite	2
Felsic/rhyolite Tlt, Tjb, Trf	Potassic	S, Ba, Mg, Mn, P, Sr, Cu, Se, W, Sb, Ag, Bi ± Ca, Mo, As	Na, Fe, Zn, Cr ± Ca, As, Mo	adularia, quartz, pyrite/marcasite, smectite/illite, chlorite ± sericite	16
	Potassic/ >10% veining	S, Fe, Ba, Mg, Mn, Sr, Cu, Sb, Ag ± Ca, Se, Mo, As, Hg	Na, Zn, Cr ± Ca, Mo, As, Se, Hg	adularia, quartz, pyrite/marcasite, smectite/illite, chlorite ± sericite, selenides	3
Felsic/ volcaniclastic Tep, Tes	Potassic	S, Al, Ti, Mg, P, Sr, Cr, Cu, Sb, W ± Fe, K, Na, Ca, Ba, Mn, Zn, Y, Pb, As, Mo, Se	± Fe, K, Na, Ca, Ba, Mn, Zn, Y, Pb, As, Mo, Se	adularia, quartz, pyrite/marcasite, smectite/illite, chlorite ± sericite, selenides	9
	Potassic/ >10% veining	S, Al, Fe, K, Ti, Mg, P, Zn, Y, Pb, As, Mo, Cu, Sb, Se, W, Ag, Bi, Hg	Na, Ca, Ba, Mn	adularia, quartz, pyrite/marcasite, smectite/illite, chlorite ± sericite, selenides	1
	Argillic	S, Al, K, Mg, Ti, P, Y, Pb, Cu, W, Ag, Hg ± Na, Ca, Ba, Mn, Zn, Sr, Cr, As, Mo, Se, Bi	± Na, Ca, Ba, Mn, Zn, Sr, Cr, As, Mo, Se, Bi	smectite, kaolinite ± carbonate, pyrite, chlorite	5

(Table 5). The appearance of trace amounts of illite and feldspars rimmed with adularia within the narrow, intense potassic zone along the main faults reflects larger gains in K (or depletions in other elements). Upflow and boiling zones in basalt-hosted geothermal systems in both mafic (e.g., Iceland, Kristmannsdottir, 1978), and felsic volcanic-hosted geothermal systems (e.g., Wairakei thermal area, New Zealand, Steiner, 1968; Broadlands-Ohaaki geothermal field, Simmons and Browne, 2000) show increases in K that may be due to deeply derived chloride-rich fluids (Henley and Hedenquist, 1986; Cooke and Simmons, 2000; Simmons and Browne, 2000).

Silicic alteration is more abundant and laterally widespread near the present-day surface, and likely formed from cooling of ascending hydrothermal fluids supersaturated with silica (Berger and Eimon, 1983; Silberman and Berger, 1985; Cooke and Simmons, 2000). At Midas the fluids ascended along fractures and faults and migrated laterally along permeable horizons such as bedding. This type of silicification may be related to formation of sinters preserved to the east of the main Midas vein where fluids flowed out onto the paleosurface. At the Eastern Star prospect, 5 km east of the Ken Snyder mine, an intrusive or hydrothermal vent breccia that contains rounded fragments of Paleozoic cobbles, chalcedony, and angular volcanic rocks within a rhyolite matrix (Bentz et al., 1983; LaPointe et al., 1991) is silicified and cut by banded Au-quartz veins that are the same age as main-stage mineralization at Midas (Leavitt et al., 2004). This area is underlain by the unit Tts, which was deposited before and during hydrothermal activity at Midas. The clasts of chalcedony indicate that silicification preceded main-stage vein formation, and may have been coincident with the silicic-potassic alteration of wall rocks adjacent to the main stage veins.

Veins formed during multiple episodes of boiling, brecciation, and deposition of variable quantities of bladed calcite, silica (commonly amorphous during precious metal events), and adularia along with precious metals and selenides. Stage II vein deposition encompasses the majority of ore-grade mineralization. Bladed calcite, adularia, and amorphous silica (now recrystallized) are present within the veins over almost the entire vertical extent of the vein observed for this study, ranging from the ~4600 ft level (1400 m) to the present-day surface at the 6200 ft level (1890 m). Periodic influxes of oxygen- and Fe-rich waters produced bands rich in amethystine quartz, and pyrite oxidized to hematite in adjacent wall rocks, likely between episodes of boiling. These fluids may have mixed with ascending silica- and gold-rich waters resulting in formation of both adularia and kaolinite (Reed, 1994), suggesting that kaolinite within the main veins was not due to a late-stage argillic overprint.

Abundances of pyrite increase towards the main and subsidiary faults to 20 volume percent in wall rocks. In marked

contrast, the main-stage veins contain relatively little sulfide (≤ 5 vol%). Late-stage pyrite-lined fractures cut veinlets associated with alteration that preceded the main veins, as well as the main veins. The effect of the episodic influx of H_2S-bearing fluids and role of sulfidation as a potential cause of mineralization is not clear.

Late cross-cutting veins and fractures were variably filled with montmorillonite, kaolinite, framboidal pyrite, minor crystalline quartz, carbonate, jarosite, and hematite, and extend to the lowest levels for which samples are available. The pyrite is similar texturally to pyrite in late-stage veins at Creede (Plumlee and Rye, 1992; Reed and Plumlee, 1992). This late-stage alteration resulted from fluids of lower pH than earlier hydrothermal fluids, and minerals were deposited at lower temperatures than the main veins, probably <200°C, and possibly <120°C (de Ronde and Blattner, 1988). The fluids may represent near-surface, steam-heated waters that percolated downwards as the system cooled (de Ronde and Blattner, 1988; Reed and Plumlee, 1992). This stage of alteration coincided with collapse of the hydrothermal system (Simmons and Browne, 2000). Shallower, argillic alteration of volcaniclastic rocks may have formed from these steam-heated waters (Henley and Hedenquist, 1986; Simmons and Browne, 2000), or later during supergene weathering of sulfides and production of acidic meteoric waters. Argillically altered subsidiary faults, containing abundant smectite and anomalous pathfinder elements as well as Ag and Mo, may have formed during hotter phases of the hydrothermal system, and resulted from increased water:rock interactions along the faults (Reed, 1994).

COMPARISON TO OTHER LOW-SULFIDATION HYDROTHERMAL SYSTEMS

The spatial and temporal patterns of alteration at Midas are similar to those described for many other volcanic-hosted precious-metal, epithermal systems (Buchanan, 1981; Berger and Eimon, 1983; Silberman and Berger, 1985; Cooke and Simmons, 2000; Hedenquist et al., 2000). Propylitic assemblages are similar to those described for many Miocene low-sulfidation epithermal systems in Nevada including Buckskin-National (Vikre, 1985), Sleeper (Nash et al., 1995), the Comstock Lode (Hudson, 2003), and Mule Canyon (John et al., 2003). The presence of epidote marks a change to more intense propylitic alteration at the Comstock Lode (Hudson, 2003) and Round Mountain (Sander and Einaudi, 1990) and corresponds to increased temperatures of alteration (=250°C) closer to the main ore zones. The apparent lack of chlorite and epidote in propylitic assemblages at Mule Canyon (John et al., 2003) indicates lower temperatures of alteration. In systems hosted by felsic rocks, propylitic alteration is not easily distinguished or recognized. At Midas, recognition of propylitized rhyolites and volcaniclastic felsic rocks was hampered by later overprints of argillic alteration. At Round Mountain, replacement of sanidine by adularia was the key feature used to recognize propylitic alteration in felsic tuffs (Sander and Einaudi, 1990). There, the propylitic assemblage includes quartz-adularia-albite-chlorite-calcite-pyrite±epidote. Adularization of sanidine survived subsequent alteration overprints.

The potassic assemblage at Midas (Tables 2b and 5) is similar to the propylitic-a assemblage (chlorite-albite-quartz-illite-pyrite-K feldspar±epidote±calcite) that borders the Comstock Lode (Hudson, 2003), and the potassic assemblage described at Round Mountain (quartz-adularia-calcite-white mica-pyrite-rutile). At Round Mountain this assemblage may include chlorite at depth (Silberman and Berger, 1985). It is also similar to an intermediate alteration zone containing illite-montmorillonite-quartz-pyrite close to the Bell vein at Buckskin-National (Vikre, 1985). The adularia-smectite alteration assemblage at Mule Canyon (John et al., 2003) is roughly equivalent to the potassic assemblage at Midas. At Sleeper, a rhyolite-hosted intermediate narrow zone between outer argillic and inner silicified ore contains quartz-sericite; mafic rocks are locally altered to quartz-sericite-pyrite (QSP; Nash et al., 1995). This QSP alteration zone may be the approximate equivalent of potassic alteration at Midas. The presence of adularia in assemblages at Midas and Round Mountain indicate hydrothermal fluids of higher pH than those at Buckskin-National and Sleeper. The presence of kaolinite in the zone of intense potassic alteration adjacent to main-stage veins at Midas is similar to an assemblage adjacent to the Bell vein at Buckskin-National (Vikre, 1985) that contains kaolinite-quartz-illite-pyrite.

Shallow silicic alteration that blossoms outwards at shallow levels at Midas is similar to zones of silicic alteration above the ore body at Sleeper (Nash et al., 1995), Round Mountain (Sander and Einaudi, 1990), and Buckskin-National (Vikre, 1985). This zone grades upwards, and locally laterally, into sinters at Buckskin-National, and possibly Round Mountain (Silberman and Berger, 1985). At Midas overlying sinters have been removed through erosion, but sinters from lateral flow and outflow are preserved to the east. Argillic alteration containing smectite±kaolinite is commonly found at shallower levels of these systems as well. Examples include Hishikari (Isawa, et al., 1990), Sleeper (Nash et al., 1995), and Buckskin-National (Vikre, 1985) and Midas; the argillic assemblage may have formed from steam-heated waters (Henley and Hedenquist, 1986; Simmons and Browne, 2000). In other systems including Sleeper (Nash et al., 1995) and Mule Canyon (John et al., 2003), argillic alteration forms a halo around inner potassic assemblages.

Sulfidation is common in some of these deposits and increases in intensity towards the main veins and subsidiary structures. Increased iron sulfide (pyrite ± marcasite) contents towards faults and fractures are described for Buckskin-National (Vikre, 1985), Hishikari (Isawa et al., 1990), Sleeper (Nash et al., 1995), and Mule Canyon (John et al., 2003). Preferential sulfidation of magnetite versus ilmenite is present in basalts at Mule Canyon (John et al., 2003). Increases in the iron sulfide content are also associated with hydrothermal breccias

at Sleeper that are peripheral to the high-grade veins; the breccias comprise low-grade ore. In all of these deposits, there appears to be a discontinuity between the sulfide content of wall rocks adjacent to ore, which is typically at a maximum for a system, and the high-grade gold veins that are relatively iron sulfide-poor. Although increasing iron sulfide contents provide a vector to mineralized faults, the effect of sulfidation on Au-rich fluids, if any, is not known. The relative lack of iron sulfides in veins may be due to a lack of iron, and/or changes in conditions of deposition.

Geochemical changes that accompany alteration at Midas are similar to most other low-sulfidation deposits with the exception of propylitic alteration which shows a range of geochemical behaviors. At Round Mountain propylitic alteration is generally isochemical (Sander and Einaudi, 1990). At Mule Canyon, where mafic volcanic rocks host propylitic alteration, gains in S, CO_2, and $H_2O \pm Hg \pm As$, and variable losses in Mg and Na are observed (John et al., 2003); these changes are similar to those observed at Midas. The lack of chemical changes at Round Mountain may reflect the influence of host rock; Fe-bearing phases may be necessary for sulfidation and consequent mild enrichment in pathfinder elements. Potassic alteration generally is accompanied by additions of S, CO_2, and H_2O; variable additions of K and Fe; and variable losses in Na, Ca, and Mg at Round Mountain, Mule Canyon, Sleeper, Buckskin-National (Vikre, 1985; Sander and Einaudi, 1990; Nash et al., 1995; John, et al., 2003), and Midas. Lead and Mo show weak increases with potassic alteration and quartz-adularia veins at Mule Canyon (John, et al., 2003). At Midas, Mo shows an association with potassic and argillic alteration. At Sleeper, Mo is more commonly associated with Au than base metals, but does not form any notable haloes beyond ore zones (Nash et al., 1995). Similar to Midas, base metals are most enriched in ore, but may form lower-grade haloes around the main ore zones.

Lithologic controls on the distribution of trace elements are apparent within the bimodal-hosted systems including Midas and Sleeper. At Sleeper, increases in Fe, Ti, P, Cr, and V reflect the presence of mafic host rocks (Nash et al., 1995). Increases in W with potassic alteration in mafic and felsic lithologies at Midas are not commonly described for low-sulfidation systems. Haloes of Hg, As, Sb and Tl are common at shallow levels, above or peripheral to ore. At Buckskin-National, Hg-bearing sinter formed above the main veins. At Sleeper, As forms a halo around the main ore body. At Midas, Hg is present in sinters and opalized sediments preserved to the east of the deposit.

A temporal progression of alteration assemblages from propylitic to potassic alteration is common in low-sulfidation epithermal deposits (Buchanan, 1981), and has been described at Round Mountain (Sander and Einaudi, 1990), Mule Canyon (John et al., 2003), Sleeper (Nash et al., 1995), and possibly Buckskin-National (Vikre, 1985). Intense potassic alteration containing kaolinite adjacent to the main ore zones may be slightly later than potassic alteration and main-stage mineralization, or may be coeval with main-stage mineralization, and reflects stability of kaolinite with adularia due to silica saturation of hydrothermal fluids (Reed, 1994). At Midas, a slight increase in base metals, particularly Zn, occurs during potassic alteration, prior to main-stage mineralization. Base metals are present in the early stages of banded ore at Buckskin, and deposition of pyrite-sphalerite is roughly coeval with deposition of electrum-silver selenides (Vikre, 1985). At Mule Canyon, minor base metal sulfides are present in hydrothermal breccias; the timing of these breccias relative to higher-grade Au-rich banded vein ore and alteration is not well constrained. Silicification and deposition of sinter occur during early and late stages of these systems. At Midas, silicification and sinter formation appear to have preceded main-stage veins, and is similar to the timing of early silicification at Sleeper (Nash, et al., 1995). Late-stage silicification ± sinter formation took place after formation of ore at Buckskin-National (Vikre, 1985) and Round Mountain (Sander and Einaudi, 1990). Stibnite-bearing veins formed after high-grade Au-quartz veins at the Buckskin-National and Sleeper deposits; however, this temporal relationship has not been identified at Midas or Mule Canyon (John et al., 2003).

The temporal progression of alteration may reflect changes in temperature and pressure associated with tectonic or hydraulic events. At Round Mountain, temperatures of alteration reached a maximum of 260° to 265° C during intense propylitic alteration, declined to below 200°C during potassic alteration and deposition of Au along fractures, to ≤180° C during late-stage alteration (Sander and Einaudi, 1990). At Buckskin-National, the earliest alteration event was coeval with formation of barren quartz veins at temperatures of 250° to 295° C under lithostatic conditions. After rupture of the overlying rhyolite, temperatures of fluids ranged from 100° to 255° C, and boiling accompanied precipitation of precious metals at ~250°C. After additional brecciation and tectonic movement, chalcedonic silica, Hg, and Sb were deposited at ≤ 200° in veins, and Hg-bearing sinters formed on the surface at ~100° C (Vikre, 1985).

Although ore extends over a vertical distance of at least 450 m, Midas, as well as the other low-sulfidation epithermal systems in northern Nevada described above, does not exhibit an increase in base metals with depth, a feature commonly observed in other epithermal systems (Buchanan, 1981; Silberman and Berger, 1985). The lack of zonation may indicate that only the upper portion of the system was studied, and that base metals may be present at greater depth. Like many hot-spring systems (Silberman and Berger, 1985), Midas shows an increase in pathfinder elements (Hg, As, and Sb), a decrease in Ag/Au, and locally abundant silica above ore zones towards the paleosurface.

CONCLUSIONS

Zonation of alteration assemblages shows increases in temperatures and water:rock interactions toward the main veins. Mineral isograds within the relatively widespread propylitic

zone are subparallel to veins, and provide vectors to ore. Cross-cutting veinlets within altered rocks suggest a temporal evolution from moderate propylitic alteration to potassic alteration. Silicic-potassic alteration temporally and spatially coincided with the initial stage of vein formation. Fluids that caused propylitic alteration evolved from CO_2-bearing waters, possibly deuteric in origin, to H_2S- and CO_2-bearing waters ranging in temperature from <200°C to 250ºC. During potassic alteration, the addition of K and variable amounts of base metals along deep-seated faults probably resulted from addition of deeply-derived alkali-chloride waters at temperatures between ~200°C to 250ºC (e.g., de Ronde and Blattner, 1988; Simmons and Browne, 2000; Cooke and Simmons, 2000). Boiling that accompanied deposition of the main veins was possibly triggered by a sudden change in pressure. Geologic reconstructions, secondary mineral isograds, and fluid inclusions indicate that the southern end of the GC fault (close to the intersection with the CG fault) was the location of the central upflow zone. The paleowater table sloped away from a high at this location.

Mercury and arsenic haloes overlie the shallowest portions of productive veins and broaden towards the present-day surface. Within veins, vertically-zoned anomalies of Hg, As, and Sb give way to slight base-metal enrichment with depth. Enrichment in K along the main faults extends to the present-day surface. Similar to K, enrichment in Se and precious metals, particularly Au, is restricted to permeable zones in which evidence of boiling is usually present. Unlike K, precious metals are variably present at shallower levels; Se is present in relatively low concentrations. Laterally-zoned geochemical haloes show progressive increases in pathfinder elements and minor base metals with increases in water-rock interaction as the veins are approached. Although obscured by an overprint of supergene weathering and argillic alteration, surface exposures demonstrate a lateral zonation of alteration assemblages and geochemical anomalies similar to those at greater depth.

ACKNOWLEDGEMENTS

Initial funding for this study was provided by a grant from Franco-Nevada Mining Corporation, facilitated by Ken Snyder. Additional funding was provided by the University of Nevada, Reno; Newmont Mining Corporation; student grants from the Society of Economic Geologists and the Geological Society of America; and the Woman's Auxiliary to the American Institute of Mining, Metallurgical and Petroleum Engineers, Inc. Without the core, geologic logs, and geochemical data provided by Franco-Nevada Mining Corporation, this study would not have been possible. Continued access to the deposit provided by Normandy Mining and Newmont Mining Corporation enhanced the scope and results of this project. Discussions with Don Hudson were helpful in interpreting clay analyses. John McCormack kindly provided microprobe analyses of chlorites. Unconditional support from my husband, children, and pets made this project possible.

REFERENCES

Arnórsson, S., Gunnlaugsson, E., and Svavarsson, H., 1983, The chemistry of geothermal waters in Iceland. II. Mineral equilibria and independent variables controlling water compositions: Geochimica et Cosmochimica Acta, v. 47, p. 547–566.

Bargar, K.E., and Keith, T.E.C., 1999, Hydrothermal mineralogy of core from geothermal drill holes at Newberry volcano, Oregon: U.S. Geological Survey Professional Paper 1578, 81 p.

Bentz, J.L., Tingley, J.V., Smith, P.L., and Garside, L.J., 1983, A mineral inventory of the Elko Resource Area: Nevada Bureau of Mines and Geology Open-File Report 83-9, p. 1–6.

Berger, B.R., and Eimon, P.I., 1983, Conceptual models of epithermal precious-metals deposits, *in* Shanks, W.C. III, ed., Cameron Volume on Unconventional Mineral Deposits: Society of Mining Engineers, p. 191–205.

Bevins, R.E., Robinson, D., and Rowbotham, G., 1991, Compositional variations in mafic phyllosilicates from regional low-grade metabasites and application of the chlorite geothermometer: Journal of Metamorphic Geology, v. 9, p. 711–721.

Blair, K.R., 1991, Geology of the Gold Circle district, Elko County, Nevada: Unpubl. M.Sc. thesis, University of Arizona, Tucson, 85 p.

Blakely, R.G., and Jachens, R.C., 1991, Regional study of mineral resources in Nevada—insights from three-dimensional analysis of gravity and magnetic anomalies: Geological Society of America Bulletin, v. 103, p. 795–803.

Browne, P.R.L, 1978, Hydrothermal alteration in active geothermal fields: Annual Review of Earth and Planetary Science, v. 6, p. 229–250.

Browne, P.R.L, and Ellis, S.J., 1970, The Ohaaki-Broadlands hydrothermal area, New Zealand: mineralogy and related geochemistry: American Journal of Science, v. 269, p. 97–131.

Buchanan, L.J., 1981, Precious metal deposits associated with volcanic environments in the southwest, *in* Dickinson, W.R., and Payne, W.D., eds., Relations of tectonics to ore deposits in the Southern Cordillera: Arizona Geological Society Digest, v. XIV, p. 237–262.

Carlson. R.W., and Hart, W.K., 1987, Crustal genesis on the Oregon Plateau: Journal of Geophysical Research, v. 92, p. 6191–6206.

Casteel, M.V., Schmidt, K, Goldstrand, P., Bernard, J., and Sandberg, J., 1999, Geologic setting of the Ken Snyder gold and silver mine, Elko, County, Nevada, *in* Kizis, J.A., Jr., ed., Low-sulfidation gold deposits in northern Nevada, 1999 spring field trip guidebook: Geological Society of Nevada Special Publication, n. 29, p. 213–220.

Cathelineau, M., and Nieva, D., 1985, A chlorite solid solution geothermometer, the Los Azufres (Mexico) geothermal system: Contributions to Mineralogy and Petrology, v. 91, p. 235–244.

Christiansen, R.L., and Yeats, R.S., 1992, Post-Laramide geology of the U.S. Cordilleran region: Geological Society of America, Geology of North America, v. G-3, p. 261–406.

Cleverly, J.S., 1997, A geological and mineralogical investigation of a selenium rich, volcanic hosted, epithermal gold-silver deposit, the Midas District, Nevada: University of Leicester University, Unpubl. M.Sc. thesis, 98 p.

Cooke, D.R., and Simmons, S.F., 2000, Characteristics and genesis of epithermal gold deposits, *in* Hagemann, S.G., and Brown, P.E., 2000, Gold in 2000: Reviews in Economic Geology, v. 13, p. 221–244.

de Caritat, P., Hutcheon, Il, and Walshe, J.L., 1993, Chlorite geothermometry: a review: Clays and Clay Minerals, v. 41, p. 219–239.

Deer, W.A., Howie, R.A., and Zussman, J., 1975, An Introduction to the Rock-forming Minerals: Longman Group Limited, London, 528 p.

de Ronde, C.E.J., and Blattner, P., 1988, Hydrothermal alteration, stable isotopes, and fluid inclusions of the Golden Cross epithermal gold-silver deposit, Waihi, New Zealand: Economic Geology, v. 83, p. 895–917.

Dong, G., Morrison, G., and Jaireth, S., 1995, Quartz textures in epithermal veins, Queensland—classification, origin, and implication: Economic Geology, v. 90, p. 1841–1856.

Glen, J.M.G., and Ponce, D.A., 2002, Large-scale fractures related to inception of the Yellowstone hotspot: Geology, v. 30, p. 647–650.

Goldstrand, P.M., and Schmidt, K.W., 2000, Geology, mineralization, and ore controls at the Ken Snyder gold-silver mine, Elko county, Nevada, *in* Cluer, J.K., Price, J.G., Struhsacker, E.M., Hardyman, R.F., and Morris, C.S., eds., Geology and ore deposits 2000: the Great Basin and beyond: Geological Society of Nevada Symposium Proceedings, May 15–18, 2000, p. 265–287.

Grant, J.A., 1986, The isocon diagram—a simple solution to Gresens' equation for metasomatic alteration: Economic Geology, v. 81, p. 1976–1982.

Gresens, R.L., 1967, Composition-volume relationships of metasomatism: Chemical Geology, v. 2, p. 47–65.

Haas, J. L., 1971, The effects of salinity on the maximum thermal gradient of a hydrothermal system at hydrostatic pressure: Economic Geology, v. 66, p. 940–946.

Hedenquist, J.W., Arribas, A.R., and Gonzalez-Urien, E., 2000, Exploration for epithermal gold deposits, *in* Hagemann, S.G., and Brown, P.E., 2000, Gold in 2000: Reviews in Economic Geology, v. 13, p. 245–277.

Hedenquist, J.W., and Henley, R.W., 1985, Hydrothermal eruptions in the Waiotapu geothermal system, New Zealand: Their origin, associated breccias, and relation to precious metal mineralization: Economic Geology, v. 80, p. 1640–1668.

Henley, R.W., and Hedenquist, J.W., 1986, Introduction to the geochemistry of active and fossil geothermal systems, *in* Henley, R.W., Hedenquist, J.W., and Roberts, P.J., eds., Guide to the active epithermal (geothermal) systems and precious metal deposits of New Zealand: Monograph Series on Mineral Deposits, n. 26, p. 1–22.

Henry, C.D., Elson, H.B., McIntosh, W.C., Heizler, M.T., and Castor, S.B., 1997, Brief duration of hydrothermal activity at Round Mountain, Nevada, determined from $^{40}Ar/^{39}Ar$ Geochronology: Economic Geology, v. 92, p. 807–826.

Hooper, P.R., Binger, G.B., and Lees, K.R., 2002, Ages of the Steens and Columbia River flood basalts and their relationship to extension-related calc-alkalic volcanism in eastern Oregon: Geological Society of America Bulletin, v. 114, p. 43–50.

Horton, D.G., 1985, Mixed-layer illite/smectite as a paleotemperature indicator in the Amethyst vein system, Creede district, Colorado, USA: Contributions to Mineralogy and Petrology, v. 91, p. 171–179.

Hudson, D.M., 2003, Epithermal alteration and mineralization in the Comstock district, Nevada: Economic Geology, p. 367–385.

Hutcheon, I., de Caritat, P., and Abercrombie, H.J., 1994, Clay minerals—equilibrium models and temperature indicators, *in* Lentz, D.R., ed., Alteration and alteration processes associated with ore-forming systems: 1994 Waterloo GAC Annual Meeting, Geological Association of Canada Short Course Notes, v. 11, p. 43–67.

Irvine, T.N., and Baragar, W.R.A., 1971, A guide to the chemical classification of the common volcanic rocks: Canadian Journal of Earth Sciences, v. 8, p. 523–548.

Izawa, E., Urashima, Y., Ibaraki, K., Suzuki, R., Yokoyama, T., Kawasaki, K., Koga, A., and Taguchi, S., 1990, The Hishikari gold deposit: high-grade epithermal veins in Quaternary volcanics of southern Kyushu, Japan: Journal of Geochemical Exploration, v. 36, p. 1–56.

Jiang, W-T., Peacor, D.R., and Buseck, P.R., 1994, Chlorite geothermometry?—contamination and apparent octahedral vacancies: Clays and Clay Minerals, v. 42, p. 497–517.

John, D.A., 2001, Miocene and early Pliocene epithermal gold-silver deposits in the northern Great Basin, western United States: Characteristics, distribution and relationship to magmatism: Economic Geology, v. 96, p. 1827–1853.

John, D.A., Hofstra, A.H., Fleck, R.J., Brummer, J.E., and Saderholm, E.C., 2003, Geologic setting and genesis of the Mule Canyon low-sulfidation epithermal gold-silver deposit, north-central Nevada: Economic Geology, v. 98, p. 425–463.

John, D.A., and Wallace, A.R., 2000, Epithermal gold-silver mineral deposits related to the northern Nevada rift, *in* Cluer, J.K., Price, J.G., Struhsacker, E.M., Hardyman, R.F., and Morris, C.S., eds., Geology and ore deposits 2000: the Great Basin and beyond: Geological Society of Nevada Symposium Proceedings, May 15–18, 2000, p. 155–175.

Kristmannsdottir, H., 1978, Alteration of basaltic rocks by hydrothermal activity at 100–300ºC: Mortland, M.M., and Farmer, V.C., eds., International Clay Conference: p. 359–369.

LaPointe, D.D., Tingley, J.V., and Jones, R.B., 1991, Mineral resources of Elko County, Nevada: Nevada Bureau of Mines and Geology Bulletin 106, p. 162–168.

Leavitt, E.D., 2001, Hydrothermal alteration and geochronology of the Colorado Grande Vein, Ken Snyder Mine, Elko County, Nevada: Ralph J. Roberts Center for Research in Economic Geology Annual Research Meeting 2000, Feb. 7–8, 2001, Program and Reports, 15 p.

Leavitt, E.D., 2002, Evolution of a Miocene, low-sulfidation epithermal gold-silver deposit associated with the northern Nevada rift, Midas, Nevada [abs.]: http://www.segweb.org/StudentGrants.htm.

Leavitt, E.D., Goldstrand, P., and Arehart, G., 2000, Hydrothermal alteration associated with the Colorado Grande vein, Ken Snyder Mine, Elko County, Nevada [abs.]: Geological Society of America Abstracts with Programs, v. 32, n. 7, p. A-251.

Leavitt, E.D., Spell, T.L., Goldstrand, P.M., and Arehart, G.B., 2004, Geochronology of the Midas low-sulfidation epithermal gold-silver deposit, Elko County, Nevada: Economic Geology, v. 99, p. 1665–1686.

Le Bas, M.J., Le Maitre, R.W., Streckeisen, A., and Zanettin, B., 1986, A chemical classification of volcanic rocks based on the total alkali-silica diagram: Journal of Petrology, v. 27, p. 745–750.

Leitch, C.H.B., and Lentz, D.R., 1994, The Gresens approach to mass balance constraints of alteration systems: methods, pitfall, examples, *in* Lentz, D.R., ed., Alteration and alteration processes associated with ore-forming systems: 1994 Waterloo GAC Annual Meeting, Geological Association of Canada Short Course Notes, v. 11, p. 161–192.

Loucks, R.R., Lemish, J., and Damon, P.E., 1988, Polymetallic epithermal fissure vein mineralization, Topia, Durango, Mexico: Part I. District geology, geochronology, hydrothermal alteration, and vein mineralogy: Economic Geology, v. 83, p. 1499–1528.

Ludington, S., Cox, D.P., Moring, B.C., and Leonard, K.W., 1996, Cenozoic volcanic geology of Nevada: Nevada Bureau of Mines and Geology Open-File Report 96-2, p. 5-1 to 5-10.

Moore, D. M., and Reynolds, R.C., Jr., 1997, X-Ray Diffraction and the Identification and Analysis of Clay Minerals: Oxford University Press, New York, NY, 378 p.

Nash, J.T., Utterback, W.C., Trudel, W.S., 1995, Geology and geochemistry of Tertiary volcanic host rocks, Sleeper gold-silver deposit, Humboldt County, Nevada: U.S. Geological Survey Bulletin 2090, 63 p.

Plumlee, G., and Rye, R., 1992, Mineralogic, isotopic and other characteristics of the fringes of diverse hydrothermal systems: the perithermal environment [abs.]: Proceedings of the 1992 V.M. Goldschmidt Conference, p. A84–A85.

Ponce, D.A., and Glen, J.M.G., 2002, Relationship of epithermal gold deposits to large-scale fractures in northern Nevada: Economic Geology, v. 97, p. 3–9.

Reed, M.H., 1994, Hydrothermal alteration in active continental hydrothermal systems, *in* Lentz, D.R., ed., Alteration and alteration processes associated with ore-forming systems: 1994 Waterloo GAC Annual Meeting, Geological Association of Canada Short Course Notes, v. 11, p. 315–337.

Reed M.H., 1997, Hydrothermal alteration and its relationship to ore fluid composition, *in* Barnes, H.L., ed., Geochemistry of Hydrothermal Ore Deposits, 3rd ed.: John Wiley and Sons, New York, NY, p. 303–365.

Reed, M.H., and Plumlee, G., 1992, Collapse of acid waters into boiling hydrothermal systems and the origin of late stage pyrite and related kaolinite, *in* Kharaka, Y., ed., Water-Rock Interactions: Proceedings of the Seventh International Symposium on Water-Rock Interaction, p. 1083–1086.

Reyes, A.G., 1990, Petrology of Philippine geothermal systems and the application of alteration mineralogy to their assessment: Journal of Volcanology and Geothermal Research, v. 43, p. 279–309.

Sander, M.V., and Einaudi, M.T., 1990, Epithermal deposition of gold during transition from propylitic to potassic alteration at Round Mountain, Nevada: Economic Geology, v. 85, p. 285–311.

Silberman, M.L., and Berger, B.R., 1985, Relationship of trace-element patterns to alteration and morphology in epithermal precious-metal deposits, *in* Berger, B.R., and Bethke, P.M., eds., Geology and Geochemistry of Epithermal Systems: Reviews in Economic Geology, v. 2, p. 203–232.

Simmons, S.G., and Browne, P.R.L., 2000, Hydrothermal minerals and precious metals in the Broadlands-Ohaaki geothermal system: implications for understanding low-sulfidation epithermal environments: Economic Geology, v. 95, p. 971–999.

Simpson, M.P., 1996, Hydrothermal alteration in the Empire zone of the Golden Cross epithermal Au-Ag deposit, Waihi, New Zealand: Unpubl. M.Sc. thesis, The University of Auckland, New Zealand, 133 p.

Simpson, M.P., Mauk, J.L., and Simmons, S.F., 2001, Hydrothermal alteration and hydrologic evolution of the Golden Cross epithermal Au-Ag deposit: Economic Geology, v. 96, p. 773–796.

Smith, C.N., 1997, Au-Ag-Se phase stability in a hishikari-type epithermal vein system at Midas, Elko County, Nevada [abs.]: Geological Society of America Abstracts with Programs, v. 29, n. 6, p. 207.

Steiner, A., 1968, Clay minerals in hydrothermally altered rocks: Clays and Clay Minerals, v. 16, p. 193–213.

Stewart, J.H., and Carlson, J.E., 1976, Cenozoic rocks of Nevada: Nevada Bureau of Mines and Geology Map 52, scale 1:1,000,000.

Vikre, P. G., 1985, Precious metal vein systems in the National District, Humboldt County, Nevada: Economic Geology, v. 80, p. 360–393.

Wallace, A.R., 1993, Geologic map of the Snowstorm Mountains and vicinity, Elko and Humboldt counties, Nevada: U.S. Geological Survey Miscellaneous Investigations Series Map I-2394, scale 1:50,000.

Wallace, A.R., 2003, Geology of the Ivanhoe Hg-Au district, northern Nevada: Influence of Miocene volcanism, lakes, and active faulting on epithermal mineralization: Economic Geology, v. 98, p. 409–424.

Wallace, A.R., McKee, E.H., Zoback, M.L., and Zimmermann, R.A., 1990, New ages for volcanic rocks, western Elko County, Nevada: Isochron/West, n. 55, p. 3–5.

Zoback, M.L., McKee, E.H., Blakely, R.J., and Thompson, G.A., 1994, The northern Nevada rift: Regional tectono-magmatic relations and middle Miocene stress direction: Geological Society of America Bulletin, v. 106, p. 371–382.

Zoback, M.L., and Thompson, G.A., 1978, Basin and Range rifting in northern Nevada: clues from a mid-Miocene rift and its subsequent offsets: Geology, v. 6, p. 111–116.

APPENDIX A—GEOCHEMICAL ANALYSIS

Method[1]	9301	9341	9302	9303	9304	9305	9306	9307	9308	9309	9310	9311
Sample ID	Al	Sb	Ba	Be	Bi	Cd	Ca	Ce	Cs	Cr	Co	Cu
	%	ppm	ppm	ppm	ppm	ppm	%	ppm	ppm	ppm	ppm	ppm
RG-97-1596	6.66	1.85	1596.5	3.1	0.11	0.14	2.15	161	2	8	1	7.6
RG-97-1740	4.18	1.9	850.8	2.2	0.06	0.28	0.05	89.7	1.1	11	0.6	6
RG-97-2030	5.66	1.15	1515.5	2.35	0.06	0.32	0.12	133	1.15	9	1.4	6.4
RG-96-1137	6.68	6.55	98.5	2.2	0.03	0.22	2.97	61.4	1.1	26	32	36
RG-96-1326	6.19	1.5	76	3.25	0.04	0.16	11.3	51	0.9	19	24.8	23.2
RG-96-1503	5.04	2.65	1134	2.75	0.07	0.36	0.98	122.5	1.1	<1	0.7	9
RG-96-1541	4.03	2.75	929	1.75	0.13	0.3	0.2	88.2	1.05	12	1.1	30
RG-96-1604	5.29	0.95	1219.5	2	0.06	0.34	0.45	125.5	1.45	11	0.8	7.4
RG-6-900	5.67	3.9	162	1.7	0.19	0.34	0.34	82	1.65	14	12.4	11.6
RG-6-985	6.24	4.7	395.5	2.9	0.06	0.26	1.34	84.6	1.05	26	13	19
RG-6-1079	4.45	22.05	917	1.65	0.07	0.28	0.78	93.4	0.9	12	1.4	10.6
RG-6-1153	6.14	4.15	274.5	1.85	0.07	0.4	0.45	139	0.75	10	0.8	11.2
RG-62-207	6.67	0.9	364.5	1.05	0.01	0.1	2.72	41	0.95	90	25.8	24.8
RG-62-340	6.29	14.15	80.5	2	0.07	0.26	3.85	69.6	0.65	25	30.4	36.4
RG-62-553	4.64	3.2	96.5	2.25	0.09	0.36	1.42	103	0.8	12	2.4	8.2
RG-62-559	3.15	6.25	127	1.7	0.06	0.2	0.19	48.9	1.3	7	1.2	7.2
RG-62-571	5.15	4.5	1198.5	2.25	0.05	0.34	0.19	120.5	1.45	6	0.7	10.4
RG-62-600	4.94	3.85	335.5	2.9	0.05	0.38	0.75	117.5	1.75	6	0.6	11
RG-62-653	5.24	3.25	642.8	2.9	0.06	0.34	1.4	122	1.4	7	0.8	11
MUC-82-171	6.14	3.25	701.1	2.6	0.1	0.4	1.98	149	1.05	4	0.5	6.8
MUC-82-191	4.53	4.4	806.8	1.95	0.04	0.28	0.85	108.5	1.1	8	0.5	13.6
MUC-82-347	5.29	4.15	160.5	2.3	0.06	0.32	0.97	118.5	0.8	8	1.5	8.2
MUC-82-489	6.56	3.65	970.3	6.25	0.05	0.1	4.14	76.6	1.4	20	25.6	29.2
RG-97-151	7.79	2.35	204.5	0.8	0.01	0.12	5.28	43.1	0.9	111	30.2	29.6
RG-97-615	9.61	0.9	854	1.1	0.04	0.16	5.36	52.7	3.7	107	31.2	32.4
RG-97-930	6.26	10.65	52.5	1.1	0.03	0.22	2.35	57.4	1.9	26	27.3	38.8
RG-97-1281	5.11	1.55	250	1.95	0.01	0.34	13	50	2.35	20	18.8	29.2
RG-97-2300	6.14	0.95	1643	2.35	0.06	0.34	0.96	165.5	1.1	7	0.7	10.6
RG-96-947	6.12	3.3	676.2	1.3	0.04	0.1	7.3	53.1	1.15	23	17.2	30
RG-6-175	7.7	0.65	686.8	0.95	0.01	0.08	4.77	49.8	1.3	83	27	30.4
RG-6-380	4.74	4.2	917.8	1.5	0.01	0.32	1.11	86.6	0.7	6	1.6	7.8
RG-62-93	8.47	1.85	371	0.8	0.02	0.26	5.18	43.5	0.7	114	31.1	30
MUC-82-111	6.48	5.75	1634.5	1.85	0.06	0.38	0.25	171	0.95	9	1.6	7.4
MUC-82-145	5.43	6.35	1300	1.9	0.05	0.98	0.66	158	1	7	0.4	5.8
MUC-82-222	6.81	3.5	143.5	1.7	0.06	0.34	1	173.5	0.45	6	0.6	6.6
MUC-82-406	6.66	1.75	1177.5	1.85	0.01	0.2	2.55	126.5	0.9	4	17.5	24.8
MUC-82-538	6.88	4.05	1016	2.85	0.03	0.04	3.16	109.5	0.9	5	21.1	29.2
RG-62-253	7.64	15.05	103	1	0.46	0.82	1.33	127	1.85	59	19.7	31.4
RG-62-316	6.27	10.25	73.5	1.9	0.36	0.68	1.98	123	1.3	7	1.7	7.8
RG-97-400	5.84	2.7	391.5	2	0.07	0.52	3.63	134.5	0.45	4	1.5	6.8
RG-96-635	7.1	1.7	237	3.45	0.29	0.26	0.65	117	1.65	23	8.8	11.8
RG-6-600	5.71	8.35	185	1.95	0.1	0.26	1.84	120	0.6	3	0.8	5.2
RG-62-457	6.11	3.9	87	1.85	0.23	0.46	1.71	104.5	1	22	7.7	15.4
RG-97-1962	6.62	0.75	1678	2.1	0.29	0.32	1.36	145.5	5.15	7	1.2	7.6
MI-S-1	9.59	0.3	697.2	0.8	0.16	0.08	5.9	39.9	5.05	187	32.3	22.6
MI-S-61	6.35	0.4	391	2.7	0.1	0.12	0.33	121.5	3.3	7	0.5	7.8

1 ALS Chemex analytical method

Method[1]	9312	9313	9315	9316	9317	9318	9319	9320	9321	9322	9323	9324
Sample ID	Ga	Ge	Fe	La	Pb	Li	Mg	Mn	Mo	Ni	Nb	P
	ppm	ppm	%	ppm	ppm	ppm	%	ppm	ppm	ppm	ppm	ppm
RG-97-1596	23.7	1.05	2.42	81.5	24	35.4	0.23	755	3.85	1	25.6	150
RG-97-1740	20.8	1.7	2.76	47	16.5	37.4	0.16	440	3	1.2	16	70
RG-97-2030	25.15	1.15	2.49	68.5	22.5	27	0.32	335	2.45	1.2	25.5	250
RG-96-1137	18.55	1.4	8.52	28.5	10	38.4	1.25	1135	5.8	10	11.3	2520
RG-96-1326	20.4	2.55	6.53	24.5	10	75.8	1.25	870	0.6	7	6.5	2090
RG-96-1503	20.35	0.9	1.96	63	26	48.6	0.28	360	2.05	0.8	22	110
RG-96-1541	13.5	0.9	1.9	45	35.5	38.8	0.12	240	2.05	1.6	16.1	140
RG-96-1604	21.2	0.95	2.59	66.5	20	35.6	0.2	485	4.25	1.4	24.9	140
RG-6-900	19.05	0.8	4.5	39	16	54	0.82	700	2.7	3.4	16.1	1290
RG-6-985	25.7	0.8	4.51	43	12	56	0.98	780	0.85	7	14.2	880
RG-6-1079	24.1	0.95	6.01	48	30.5	23.4	0.05	220	12.6	1.6	18.5	130
RG-6-1153	21.9	0.7	2.77	69.5	20	19	0.06	270	21.45	1.8	21.6	170
RG-62-207	15.65	0.55	5.35	19	6	46	3.33	755	0.95	38	8.7	1460
RG-62-340	20.35	0.85	8.47	34	13.5	25.2	1.81	1295	7.05	10.4	10	3570
RG-62-553	19	0.55	2.35	51	19	30	0.62	440	0.9	1.2	19.6	310
RG-62-559	8.8	0.9	1.8	24.5	9.5	63.6	0.18	85	25	1.8	12.1	140
RG-62-571	19.5	0.85	2.28	63	19.5	46.2	0.3	355	4	1	22.4	110
RG-62-600	18.65	0.7	2.08	60.5	18.5	26.6	0.13	645	4.15	0.6	22.1	90
RG-62-653	18.4	0.75	2.74	64.5	19.5	30.2	0.18	700	5.4	3.4	25.9	80
MUC-82-171	25.2	0.45	2.29	75.5	24.5	25.2	0.25	745	2.85	0.2	25.7	100
MUC-82-191	17.15	0.6	2.19	57.5	18	32	0.07	290	4	1	21	80
MUC-82-347	25.95	0.55	2.81	60	18.5	38.4	0.1	360	3.75	1.4	20	260
MUC-82-489	23	3.6	6.76	38	10	48	1.36	1305	2.85	6	15.4	2010
RG-97-151	16.85	0.95	5.55	20.5	5.5	18	2.9	835	1.3	43	10.4	1470
RG-97-615	20.5	1.3	5.32	25.5	8	13	3.08	1025	1.35	45	13.2	1640
RG-97-930	24.1	0.7	7.28	28	7	40	1.46	805	2	12	11	2250
RG-97-1281	15.35	0.5	4.71	24.5	5.5	42.6	1.2	1405	1	11.8	8.1	1780
RG-97-2300	21.8	1.1	2.47	80.5	20	38.8	0.2	530	4.35	1.6	29.4	70
RG-96-947	19.5	1.5	5.55	26	6	25	1.42	1355	1.2	11	10.4	2020
RG-6-175	15.7	1.15	5.57	24	5	17.4	3.58	850	0.95	35.8	11.8	1660
RG-6-380	14.3	0.6	2.32	36	13.5	36.8	0.45	495	1.35	1.6	14.2	250
RG-62-93	17.45	1.3	5.55	20.5	6	13.4	4.01	915	1.15	45.4	10.6	1420
MUC-82-111	22.7	0.75	2.49	82.5	19	30	0.29	475	4	2.2	21.9	160
MUC-82-145	21.15	0.9	2.13	61.5	18.5	28.2	0.14	465	2.55	1.4	18.9	60
MUC-82-222	27.65	0.9	1.72	66	19	26.6	0.1	395	2.35	1.2	21.8	90
MUC-82-406	22.65	1.35	7.02	48.5	10.5	52.6	1.3	1315	2.5	2	18.4	2840
MUC-82-538	22.5	2.8	6.52	42	13.5	46.2	1.4	1255	3.75	2.8	19.6	2430
RG-62-253	27	0.8	5.96	47.5	19	47	2.53	1205	80.28	22.6	25.4	1070
RG-62-316	17.75	0.5	2.87	48.5	13.5	19.6	0.83	805	3.85	1.8	20.4	200
RG-97-400	16.3	0.55	2.62	53	17.5	18.6	0.11	665	0.5	1.8	21.7	100
RG-96-635	21.1	1.15	3.45	46	16	45	0.71	600	3.45	5.6	17.2	450
RG-6-600	16.55	0.5	2.3	49	13.5	32.4	0.74	440	1.7	1	11.8	140
RG-62-457	20.6	0.65	3.25	40.5	15	26.8	0.77	630	7.95	5.4	15	510
RG-97-1962	20.15	1.1	2.51	59.5	18	26.2	0.22	430	2.8	1.6	20.7	260
MI-S-1	17	1.15	5.35	20	4	5	4.16	1050	1.2	37.4	9.8	1090
MI-S-61	19.45	1.5	1.92	50	18	10.6	0.11	165	2.25	1.8	30.2	100

1 ALS Chemex analytical method

Method[1]	9325	9326	9327	9328	9329	9330	9331	9332	9333	9334	9335
Sample ID	K	Rb	Ag	Na	Sr	Ta	Te	Tl	Th	Ti	W
	%	ppm	ppm	%	ppm	ppm	ppm	ppm	ppm	%	ppm
RG-97-1596	5.28	184.5	0.5	1.81	92	1.4	<0.05	1.16	10.6	0.17	0.7
RG-97-1740	3.23	118	1.5	0.97	25.4	0.9	<0.05	0.9	5.2	0.08	0.8
RG-97-2030	4.41	130	0.48	1.93	49.2	1.4	<0.05	0.8	7.4	0.14	1.1
RG-96-1137	1.17	36.2	0.26	3.07	302	0.65	<0.05	0.3	2.6	0.98	1.4
RG-96-1326	0.17	6.2	16.8	0.62	141	0.35	0.2	0.04	3.4	0.77	1.2
RG-96-1503	3.97	141.5	>100.0	1.46	56.8	1.2	0.05	1.12	7.8	0.12	1.1
RG-96-1541	4.61	143.5	6.78	0.71	32.6	0.9	0.1	1.18	5.4	0.09	1.9
RG-96-1604	5.54	191.5	1.04	0.69	43.6	1.35	<0.05	1.68	8.6	0.15	0.9
RG-6-900	5.34	211	1.6	0.09	137.5	0.9	0.15	1.66	4	0.49	5.6
RG-6-985	4.06	150.5	1.66	1.31	152	0.85	<0.05	1.3	5.8	0.37	1.7
RG-6-1079	3.28	107.5	4.02	1.78	61.6	1.05	0.05	4.06	5.8	0.12	1.3
RG-6-1153	3.43	117.5	1.74	3	43	1.3	0.05	1.12	5.4	0.12	0.7
RG-62-207	0.98	33.2	0.34	1.33	169.5	0.5	<0.05	0.2	2.6	0.61	0.4
RG-62-340	1.52	51.4	1.8	1.94	203	0.5	<0.05	0.98	3	0.84	2.6
RG-62-553	2.12	77.9	1.56	0.73	57.9	1.05	<0.05	0.72	4.4	0.18	0.7
RG-62-559	2.95	121	>100.0	0.21	29.4	0.65	<0.05	1.1	3	0.1	5.6
RG-62-571	4.62	155	1.36	0.58	35.2	1.25	<0.05	1.26	7.4	0.13	1.2
RG-62-600	5.65	197	0.96	0.55	38.2	1.2	<0.05	1.58	6.2	0.12	1.7
RG-62-653	5.26	197	0.86	0.61	54.7	1.4	<0.05	1.44	7.8	0.15	0.9
MUC-82-171	3.27	123.5	0.86	1.55	64	1.45	<0.05	0.86	7.8	0.13	0.5
MUC-82-191	3.9	137	1.54	1.37	33.4	1.1	<0.05	0.92	7.2	0.11	0.8
MUC-82-347	3.64	131.5	0.9	2.29	93.1	1.15	<0.05	0.98	5	0.16	1
MUC-82-489	2.94	103.5	0.94	2.06	276	0.75	<0.05	0.9	4.8	0.91	2.8
RG-97-151	1.34	41.1	0.44	1.76	310	0.65	<0.05	0.28	2.8	0.65	0.6
RG-97-615	1.27	33.3	0.54	1.85	449	0.9	<0.05	0.24	3.8	0.71	0.5
RG-97-930	3.01	166	1.22	1.91	192.5	0.7	<0.05	1.68	2.2	0.86	9.7
RG-97-1281	0.57	22.2	0.62	2	163	0.5	<0.05	0.14	1.6	0.63	8.6
RG-97-2300	4.82	165.5	0.9	1.29	56.5	1.6	<0.05	0.92	8.2	0.15	1
RG-96-947	1.36	55.5	0.48	2.86	299	0.65	<0.05	0.28	2.6	0.82	1.7
RG-6-175	1.4	33.2	0.46	1.73	329	0.75	<0.05	0.2	3.2	0.71	0.5
RG-6-380	2.19	60.9	0.66	1.8	54	0.8	<0.05	0.34	4.2	0.14	0.4
RG-62-93	0.79	17.4	0.42	1.69	351	0.75	<0.05	0.2	2.4	0.64	0.5
MUC-82-111	5.19	213	0.9	1.12	38.2	1.35	<0.05	1.22	5	0.13	0.7
MUC-82-145	4.16	122	0.82	1.42	29.2	1.25	<0.05	0.86	7.2	0.09	0.8
MUC-82-222	0.37	11	0.76	5.01	34	1.45	<0.05	0.08	6	0.11	0.8
MUC-82-406	2.39	85.9	0.74	2.04	166.5	1.15	<0.05	0.64	4	0.93	1.8
MUC-82-538	2.3	71.3	1.36	2.21	156.5	1.1	<0.05	0.6	3.8	1	2.6
RG-62-253	3.45	175.5	3.16	0.2	91.9	1.65	0.05	1.52	6	0.59	1.1
RG-62-316	5.18	232	1.14	0.31	68.9	1.15	<0.05	2.14	4	0.18	0.8
RG-97-400	3.11	99.1	0.86	1.51	75.5	1.15	<0.05	0.62	6.4	0.17	0.6
RG-96-635	2.38	99.8	0.6	1.57	107	1.15	0.05	0.88	5.2	0.25	1
RG-6-600	2.11	62.5	0.52	1.7	108.5	0.65	<0.05	0.5	4.2	0.08	0.6
RG-62-457	3.85	165	2.48	0.42	59.2	0.95	<0.05	1.44	4.6	0.24	0.8
RG-97-1962	3.95	107	0.8	2.19	65.7	1.35	<0.05	0.7	6.2	0.17	1.6
MI-S-1	0.79	19.9	0.36	2.09	382	0.65	<0.05	0.12	2.6	0.57	0.6
MI-S-61	3.65	173	1.06	2.05	32.4	1.8	<0.05	0.66	16.2	0.14	1.5

1 ALS Chemex analytical method

Method[1]	9336	9337	9338	9339	13	20	16	1380	1381	367
Sample ID	U	V	Y	Zn	As	Hg	Se	S	C	C
	ppm	ppm	ppm	ppm	ppm	ppb	ppm	%	%	%
RG-97-1596	1.8	8	72.8	88	<1	100	0.8	0.24		
RG-97-1740	1.3	7	35.5	124	6	50	0.4	0.32		
RG-97-2030	1.7	11	53	134	<1	40	0.6	0.17		
RG-96-1137	1.3	315	34.9	106	84	590	<0.2	2.4		
RG-96-1326	0.9	289	30.6	88	<1	<10	1.6	0.03		
RG-96-1503	1.8	6	47.5	136	1	20	32.2	0.18		
RG-96-1541	1.1	5	32.1	116	1	40	3.4	0.48		
RG-96-1604	1.5	6	45.6	130	<1	20	0.4	0.21		
RG-6-900	1	83	33.3	98	7	1900	1.6	1.4		
RG-6-985	1.1	109	32.9	112	19	210	2.2	0.78		
RG-6-1079	1.1	7	28.7	126	129	2920	2.2	5.91		
RG-6-1153	1.7	3	40	158	29	40	0.6	1.66		
RG-62-207	0.8	159	22.7	78	<1	<10	<0.2	0.38		
RG-62-340	1.9	295	40.8	104	95	890	<0.2	3.32		
RG-62-553	0.9	14	32	110	19	160	2.2	1.79		
RG-62-559	0.9	6	20.6	62	9	220	50.2	1.21		
RG-62-571	1.6	11	34.8	132	13	90	2.2	0.69		
RG-62-600	1.3	5	33.9	132	7	30	1.2	0.82		
RG-62-653	1.9	8	44.9	140	7	10	2.8	1.24		
MUC-82-171	1.5	4	46.3	140	3	710	1.4	1.36		
MUC-82-191	1.3	3	32.7	116	27	40	2.4	1.21		
MUC-82-347	1.1	4	40	138	21	110	3	1.22		
MUC-82-489	1.3	237	37.4	96	1	<10	1	0.08		
RG-97-151	0.8	189	29.1	82	12	<10	<0.2	1.32		
RG-97-615	1	221	32	108	<1	<10	<0.2	0.04		
RG-97-930	0.9	266	33.8	102	38	300	1	4.31		
RG-97-1281	0.5	211	49.9	74	5	100	0.4	0.71		
RG-97-2300	1.3	4	51.4	158	3	<10	0.2	0.11		
RG-96-947	0.9	291	34.9	84	<1	20	<0.2	<0.01		
RG-6-175	0.9	193	33	82	<1	<10	<0.2	0.69		
RG-6-380	0.4	10	23	94	14	60	0.2	0.52		
RG-62-93	0.7	209	29.5	82	4	<10	<0.2	0.51		
MUC-82-111	0.8	13	27.7	156	3	50	0.2	0.32		
MUC-82-145	1	3	40.2	146	9	60	0.8	0.39		
MUC-82-222	1	3	46.4	144	7	60	<0.2	0.22		
MUC-82-406	1.2	76	46.8	128	<1	60	<0.2	0.28		
MUC-82-538	0.9	212	41.6	128	3	10	1	0.27		
RG-62-253	2.2	131	37.4	152	144	460	<0.2	3.7	0.2	0.5
RG-62-316	1.2	10	35	128	65	150	0.2	2.7	0.5	0.68
RG-97-400	0.5	1	44.9	120	18	810	1	2.66	1.25	1.25
RG-96-635	1.5	52	37.4	108	3	80	<0.2	0.86	0.15	0.3
RG-6-600	0.9	3	29.6	68	16	120	<0.2	1.07	0.45	0.57
RG-62-457	0.9	55	30	120	35	70	0.2	2.55	0.45	0.81
RG-97-1962	1.2	15	47	142	<1	20	0.6	0.04		
MI-S-1	0.6	198	28.5	78	<1	<10	<0.2	0.01		
MI-S-61	2.7	7	38.2	98	2	180	<0.2	0.14		

1 ALS Chemex analytical method

Method[1]	9301	9341	9302	9303	9304	9305	9306	9307	9308	9309	9310
Sample ID	Al	Sb	Ba	Be	Bi	Cd	Ca	Ce	Cs	Cr	Co
	%	ppm	ppm	ppm	ppm	ppm	%	ppm	ppm	ppm	ppm
MKC202 435-500	7.45	1.4	490	2.85	0.03	0.12	5.18	53	1.8	90	32
MKC202 500-505	7.59	1	550	2.4	0.01	0.08	5.84	50.4	5.05	102	33
MKC202 615-620	7.41	0.7	360	1	0.01	0.04	5.74	37.7	2.05	231	35.2
MKC202 655-660	7.56	1	340	0.8	0.01	0.06	5.91	39.6	0.75	222	33.6
MKC202 695-700	8.25	1	350	0.8	0.01	0.08	6.55	39.9	2.3	233	35.8
MKC202 740-745	7.92	0.9	390	0.85	0.01	0.1	6.08	40.7	2.3	230	35
MKC202 755-790	7.57	1.2	260	0.9	0.01	0.08	5.76	34.5	5.8	210	36
MKC202 885-907	7.76	2	1050	2.5	0.06	0.22	1.7	79	1.45	86	26.8
MKC202 930-1005	5.04	4.8	490	2.2	0.1	0.34	1.3	133.5	1.15	146	3.2
MKC202 1005-1015	5.89	3.1	580	2.8	0.03	0.12	6.37	76.5	1.15	39	27.6
MKC202 1055-1070	6.32	3	540	2.45	0.03	0.2	4.78	61.1	0.65	48	28
MKC202 1215-1220	7.13	3	640	1.6	0.04	0.18	4.58	68.4	2.55	42	30.2
MKC202 1265-1279	6.53	1.6	610	1.45	0.01	0.18	4.37	64.4	2.85	53	29.2
MKC202 1279-1281	6.23	1.9	470	2.3	0.06	0.24	3.76	64	3.9	39	31.2
MKC202 1281-1285	6.72	1.6	420	2.7	0.09	0.24	2.83	64.9	4.1	36	31.8
MKC202 1311-1325	5.89	1.6	500	2	0.05	0.18	4.78	60.1	3.65	33	29.2
MKC202 1396-1398	7.09	3.1	490	2.35	0.03	0.22	2.73	93.6	4.3	31	30.6
MKC202 1455-1495	5.58	2.6	1250	2.25	0.1	0.4	0.84	156	2.4	81	4.6
MKC202 1495-1500	5.48	3.1	1470	1.8	0.06	0.24	0.18	145	1.75	74	2.2
MKC202 1500-1505	6.05	3.3	1630	1.95	0.09	0.3	0.16	166	1.55	102	1.6
MKC202 1565-1575	5.81	2.5	1570	3.1	0.08	0.38	0.5	167.5	1.7	78	1.6
MKC202 1575-1580	4.97	2.8	1270	2.95	0.08	0.38	1.42	155	1.9	103	1.4
MKC202 1580-1585	5.04	3.9	1140	2.6	0.09	0.36	0.36	147.5	2.3	111	0.8
MKC202 1585-1595	5.19	4.8	1330	1.9	0.06	0.34	0.12	150.5	1.6	121	1.2
MKC202 1814.3-1815.3	5	5.9	120	2.75	0.06	0.32	0.57	131.5	1.6	110	2
MKC202 1941-1986	5.2	1.7	1390	2	0.09	0.34	1.8	148	1.2	107	1.2
MKC202 2000-2050	5.46	1.4	1190	3.15	0.12	0.34	1.24	181	1.35	92	0.8
MKC202 2095-2100	5.8	1.2	1260	2.15	0.07	0.36	0.17	186.5	1.05	135	0.4
MKC202 2153-2154	4.84	1.5	1020	3.3	0.07	0.3	2.9	152	2.55	56	0.6
MKC202 2165-2175	5.71	1.6	1220	2.95	0.06	0.32	0.24	174.5	4.35	112	0.6
MKC202 2235-2243	5.28	3.5	1200	2.25	0.1	0.3	0.12	155.5	1.3	101	0.8
MKC202 2243-2245	2.7	6.4	420	1.45	0.31	0.14	0.35	42.6	1.35	281	4.6
MKC202 2245-2249	2.73	9.3	420	1.25	0.19	0.14	0.97	39.7	1.2	134	5.4
MKC202 2249-2255	6.09	1.7	1200	2.15	0.17	0.28	0.32	128	1.2	67	7.4
MKC202 2255-2261	6.09	1.7	1080	2.6	0.07	0.26	0.34	124	1.1	84	9
MKC202 2261-2265	6.12	1.7	920	2.7	0.05	0.22	1.07	104.5	1.25	65	13.8
MKC202 2265-2275	5.45	3.1	880	2.75	0.06	0.22	1.99	80	3.25	69	11.4
MKC202 2275-2285	5.57	1.7	1000	3	0.04	0.28	2.12	139.5	1.85	47	7.8
MKC202 2420-2425	5.63	1.7	1570	1.95	0.09	0.4	1.07	153.5	1.05	89	3.4

1 ALS Chemex analytical method

Method[1]	9311	9312	9313	9315	9316	9317	9318	9319	9320	9321	9322	9323
Sample ID	Cu	Ga	Ge	Fe	La	Pb	Li	Mg	Mn	Mo	Ni	Nb
	ppm	ppm	ppm	%	ppm	ppm	ppm	%	ppm	ppm	ppm	ppm
MKC202 435-500	17	21.2	0.9	5.62	24.5	7	84.2	3.56	1065	1.6	38.8	10.8
MKC202 500-505	18	21.4	0.8	5.7	23.5	6	69.8	3.91	1150	1	41.8	10.2
MKC202 615-620	18	20	1	5.49	17	4	46.6	5	1165	1	50.8	8.4
MKC202 655-660	14	18.5	1.2	5.31	18.5	3.5	16.8	4.48	985	1	42.6	8.6
MKC202 695-700	15	18.4	1.3	5.53	18.5	4.5	14	4.51	1110	1.4	46.6	9
MKC202 740-745	15	18.6	1.3	5.66	19	3.5	34.6	4.34	1215	1.4	48.4	9
MKC202 755-790	12	17	0.9	5.18	15.5	3.5	76	4.71	1115	0.8	54.4	7.6
MKC202 885-907	10	26.8	1	5.69	36.5	10	95.2	2.77	830	1.6	28.2	15.8
MKC202 930-1005	9	16.5	1	2.52	53	16	49.2	0.23	285	13.4	4.4	21.6
MKC202 1005-1015	25	31.8	1.2	6.32	29	7.5	81.2	1.72	755	1.8	12.6	10.6
MKC202 1055-1070	25	21.2	0.9	6.72	28	6.5	85	1.84	1410	1.2	12.4	6
MKC202 1215-1220	25	22.5	1.9	7.68	31	8	84.6	2.09	1410	1.4	14	12.4
MKC202 1265-1279	22	21.2	1.5	7.16	29.5	7	51.4	2.28	1400	1.4	13.4	11.2
MKC202 1279-1281	23	25.1	1.2	7.1	29	8.5	67.6	1.86	895	1.2	13.6	12.6
MKC202 1281-1285	23	25.2	1.2	7.34	29	8	72.2	2.37	950	1.4	15	12.6
MKC202 1311-1325	24	22.2	1.1	6.85	27	7.5	60.2	2.04	1240	1.4	13.4	12.4
MKC202 1396-1398	26	29.1	1	7.15	34	8.5	53.6	1.51	995	1.4	13.2	14
MKC202 1455-1495	6	22.8	1	2.87	62	20	62.6	0.54	565	3	3.4	22.4
MKC202 1495-1500	3	21.4	0.9	2.65	58	16.5	60.6	0.31	495	2.4	2.2	17.6
MKC202 1500-1505	7	22.2	0.9	2.85	66	19	49	0.3	470	2.8	2.2	21.4
MKC202 1565-1575	7	25.8	1.2	2.49	68	21.5	44.2	0.19	510	5.2	2.2	26.6
MKC202 1575-1580	11	21.4	1.1	2.06	62.5	19	55	0.2	410	3.6	2.4	23.2
MKC202 1580-1585	6	20.2	0.9	1.78	58.5	18	63.6	0.17	260	4.6	2.4	21.2
MKC202 1585-1595	6	20.7	0.9	2.19	58.5	19.5	37	0.13	335	3.6	2.6	22
MKC202 1814.3-1815.3	8	22.3	1.2	3.39	50	16	57	0.17	215	3.8	2.6	25.6
MKC202 1941-1986	7	20.6	0.9	2.11	58	19.5	45.6	0.2	445	4	4.4	24.8
MKC202 2000-2050	11	24.1	1	2.16	86.5	23	43.2	0.21	490	8.2	2.4	29.2
MKC202 2095-2100	5	25.3	0.9	2.07	87	23	46.4	0.18	340	3.6	2.8	25.6
MKC202 2153-2154	26	21.3	1.2	1.57	60.5	19	55.2	0.26	550	4	2.2	23.4
MKC202 2165-2175	8	22.7	1.2	1.79	68	23	35	0.14	235	3.6	2.2	31.8
MKC202 2235-2243	32	23.8	1.1	2.25	61	20.5	56	0.29	290	4.8	2.2	27
MKC202 2243-2245	362	11.9	0.9	1.49	20.5	15	186	0.26	225	6.2	6.4	8.2
MKC202 2245-2249	265	14.1	0.9	1.99	19	15.5	195	0.38	340	9	4.8	7.6
MKC202 2249-2255	19	24.7	0.9	3.77	51.5	18	57.2	0.71	730	5	4.8	21.2
MKC202 2255-2261	16	26	0.9	3.98	49	16.5	73.6	0.69	805	4.8	6	20.2
MKC202 2261-2265	17	23.7	0.8	4.18	41.5	14	68	0.91	810	3.8	8.2	17.6
MKC202 2265-2275	22	22.2	1.1	3.99	39.5	16	86.8	1.01	660	5.8	6.6	16.6
MKC202 2275-2285	12	24.6	1.2	3.13	55	17	67	0.61	850	4	4.6	23.6
MKC202 2420-2425	30	24.2	1.1	2.75	61	21.5	63.4	0.38	460	8.8	3.6	26.8

1 ALS Chemex analytical method

Method[1]	9324	9325	9326	9327	9328	9329	9330	9331	9332	9333	9334
Sample ID	P	K	Rb	Ag	Na	Sr	Ta	Te	Tl	Th	Ti
	ppm	%	ppm	ppm	%	ppm	ppm	ppm	ppm	ppm	%
MKC202 435-500	1660	1.53	58.2	0.35	2.16	219	0.55	<0.05	0.28	4	0.64
MKC202 500-505	1620	1.37	54.4	0.35	1.31	225	0.5	<0.05	0.24	2.6	0.62
MKC202 615-620	1210	0.74	24.6	0.3	1.55	286	0.35	<0.05	0.1	1	0.52
MKC202 655-660	1280	0.66	19.4	0.25	1.86	346	0.35	<0.05	0.1	0.8	0.54
MKC202 695-700	1280	0.64	15	0.25	1.79	381	0.45	<0.05	0.08	0.8	0.55
MKC202 740-745	1260	0.81	22.4	0.25	1.89	343	0.45	<0.05	0.12	0.8	0.53
MKC202 755-790	1100	0.6	18.8	0.2	2.03	273	0.35	<0.05	0.1	0.4	0.46
MKC202 885-907	1590	2.85	103	0.6	1.75	187.5	0.95	<0.05	0.68	2.8	0.63
MKC202 930-1005	390	2.5	95.2	0.9	2.07	72.9	0.8	<0.05	1	3.8	0.2
MKC202 1005-1015	2490	2.24	82.4	0.7	1.45	160	0.6	<0.05	0.6	1.8	0.8
MKC202 1055-1070	2530	1.78	62.6	0.75	2.22	246	0.25	<0.05	0.4	1.6	0.8
MKC202 1215-1220	2860	1.62	59.4	0.6	2.64	340	0.65	<0.05	0.34	2	1
MKC202 1265-1279	2680	1.78	65.6	0.55	2.54	313	0.6	<0.05	0.4	1.8	0.96
MKC202 1279-1281	2670	1.3	44.8	0.7	1.79	195	0.75	<0.05	0.3	2	0.94
MKC202 1281-1285	2800	1.35	49.6	0.45	0.87	172	0.75	<0.05	0.3	2.2	0.99
MKC202 1311-1325	2570	1.52	50.2	0.7	1.62	231	0.65	<0.05	0.36	1.6	0.92
MKC202 1396-1398	2990	1.54	66	0.4	1.57	295	0.75	<0.05	0.6	2.2	1.06
MKC202 1455-1495	480	2.94	162.5	0.65	1.65	102	0.95	<0.05	1.1	4.6	0.24
MKC202 1495-1500	270	2.63	125.5	0.55	1.9	74.2	0.7	<0.05	1.1	4.8	0.14
MKC202 1500-1505	240	3.23	135	0.65	2.44	72.1	0.9	<0.05	1.16	5.4	0.15
MKC202 1565-1575	230	3.91	192	0.8	1.99	52.1	0.9	<0.05	1.28	5.4	0.17
MKC202 1575-1580	160	3.76	187	2.6	1.46	57.3	0.85	<0.05	1.24	5.4	0.14
MKC202 1580-1585	100	3.8	156	0.95	1.29	70.1	0.75	<0.05	1.44	5.4	0.11
MKC202 1585-1595	170	3.71	149.5	0.65	1.4	47.8	0.75	<0.05	1.46	5.2	0.13
MKC202 1814.3-1815.3	390	2.98	119	1.25	2.05	64.5	0.85	<0.05	1.48	3.6	0.24
MKC202 1941-1986	200	3.83	156	1.3	1.59	56	1.05	<0.05	1.02	4.8	0.16
MKC202 2000-2050	160	3.68	121.5	0.75	1.83	61.3	1.15	<0.05	1.12	6.4	0.14
MKC202 2095-2100	110	4.11	169	0.55	2.07	33.4	1.5	<0.05	1.08	5.2	0.12
MKC202 2153-2154	110	4.09	166	1.25	1.33	73.6	1.3	<0.05	0.98	5.4	0.11
MKC202 2165-2175	120	4.05	169	0.65	2.19	42.8	1.1	<0.05	1.02	7.2	0.14
MKC202 2235-2243	150	3.87	162.5	1	1.47	62.2	0.9	<0.05	1.44	7.2	0.14
MKC202 2243-2245	340	1.97	72.8	5.75	0.3	55.5	0.4	0.2	0.94	2	0.15
MKC202 2245-2249	400	1.77	66.4	5.1	0.5	57	0.4	0.15	1.2	1.8	0.19
MKC202 2249-2255	520	3.56	135	0.85	1.95	103.5	0.8	<0.05	1.34	6	0.3
MKC202 2255-2261	630	3.45	131.5	1.3	1.95	105.5	0.8	<0.05	1.2	4.8	0.33
MKC202 2261-2265	810	2.68	96.4	2.35	2.43	131	0.7	<0.05	0.88	4.8	0.42
MKC202 2265-2275	730	3.03	111.5	2.1	1.33	146.5	0.9	<0.05	1.14	4	0.37
MKC202 2275-2285	540	3.34	108.5	1.15	2.01	105.5	1.2	<0.05	0.88	5.4	0.3
MKC202 2420-2425	320	3.62	116	3.35	1.8	66.2	1	<0.05	0.94	5.6	0.24

1 ALS Chemex analytical method

Method[1]	9335	9336	9337	9338	9339	13	20	16	1380	
Sample ID	W	U	V	Y	Zn	As	Hg	Se	S	As
	ppm	ppm	ppm	ppm	ppm	ppm	ppb	ppm	%	ppm
MKC202 435-500	0.9	1	184	28.2	90	<1	<10	0.2	0.15	0.5
MKC202 500-505	0.5	1	188	29	86	<1	10	0.2	0.05	0.5
MKC202 615-620	0.4	0.4	179	22.8	78	<1	<10	<0.2	0.08	0.5
MKC202 655-660	0.6	0.4	186	23.3	78	<1	<10	<0.2	0.01	0.5
MKC202 695-700	0.5	0.4	191	23.2	82	<1	10	0.2	0.04	0.5
MKC202 740-745	0.5	0.4	183	24.2	82	<1	<10	0.2	0.01	0.5
MKC202 755-790	0.5	0.2	166	19.2	76	<1	<10	0.2	0.02	0.5
MKC202 885-907	3.2	1.2	167	34.5	124	3	180	0.2	0.3	3
MKC202 930-1005	7.2	1.4	28	39	132	31	560	3.2	1.92	31
MKC202 1005-1015	8.5	0.8	236	44.7	116	19	290	1.4	0.95	19
MKC202 1055-1070	1.3	0.8	283	29.6	112	23	80	<0.2	0.51	23
MKC202 1215-1220	1.6	1	321	34.6	124	<1	10	<0.2	0.19	0.5
MKC202 1265-1279	0.9	1	311	33.3	116	<1	<10	0.2	0.1	0.5
MKC202 1279-1281	5.9	1.2	288	38.1	116	1	30	<0.2	0.25	1
MKC202 1281-1285	5.3	1.2	316	37.8	120	<1	10	0.6	0.1	0.5
MKC202 1311-1325	6.8	1	280	30.6	110	<1	40	0.2	0.36	0.5
MKC202 1396-1398	23	1.4	333	38.7	132	<1	340	0.2	0.24	0.5
MKC202 1455-1495	1.2	2	43	44	166	6	280	2	0.54	6
MKC202 1495-1500	1.4	1.6	19	40.3	132	7	370	2.2	0.83	7
MKC202 1500-1505	1	1.4	22	45.8	112	2	140	2.4	0.94	2
MKC202 1565-1575	1.3	1.6	12	46.8	154	<1	90	1	0.25	0.5
MKC202 1575-1580	1.3	1.6	10	45.3	138	<1	140	3.4	0.4	0.5
MKC202 1580-1585	1.3	2	10	43.6	136	11	730	2.8	0.86	11
MKC202 1585-1595	1.4	1.8	11	39.9	144	13	310	2.6	1.03	13
MKC202 1814.3-1815.3	9.6	1.6	18	38.2	142	45	500	4.8	2.75	45
MKC202 1941-1986	1.4	1.6	9	38.3	138	7	30	2.6	0.17	7
MKC202 2000-2050	1.1	1.6	7	51.3	146	5	10	2.6	0.21	5
MKC202 2095-2100	1.3	1	3	40.8	160	<1	60	0.4	0.18	0.5
MKC202 2153-2154	0.9	1.6	4	47.2	118	5	<10	1.4	0.18	5
MKC202 2165-2175	3.3	1.6	3	41.4	156	11	120	1	0.51	11
MKC202 2235-2243	1.6	1.6	9	41.3	144	13	160	2.2	0.88	13
MKC202 2243-2245	1.7	0.8	41	16.9	60	10	290	3	0.38	10
MKC202 2245-2249	1.8	0.8	46	17.3	58	11	210	3	0.55	11
MKC202 2249-2255	1.2	1.6	55	37.6	116	10	120	1.4	0.45	10
MKC202 2255-2261	3.5	1.8	74	36.9	118	9	60	1.2	0.36	9
MKC202 2261-2265	2.4	1.6	112	32.7	108	6	40	0.6	0.23	6
MKC202 2265-2275	2.7	1.6	93	29.8	104	13	50	1.4	0.48	13
MKC202 2275-2285	1.4	1.2	68	39.2	132	<1	10	0.8	0.21	0.5
MKC202 2420-2425	1.6	1.2	28	41.3	154	10	90	2.2	0.27	10

1 ALS Chemex analytical method

Method[1]	594	542	588	590	586	821	593	596	599	597	592	8590	595	475	540
Sample ID	Al2O3	BaO	CaO	Cr2O3	Fe2O3	K2O	MgO	MnO	Na2O	P2O5	SiO2	SrO	TiO2	LOI	TOTAL
	%	%	%	%	%	%	%	%	%	%	%	%	%	%	%
RG-97-151	15.11	0.07	7.92	0.01	8.77	1.51	5.03	0.12	2.3	0.31	49.14	0.02	1.09	7.25	98.56
RG-97-615	16.58	0.07	8.02	<0.01	8.7	1.44	4.57	0.13	2.35	0.34	51.12	0.06	1.2	5.97	100.4
RG-97-930	12.55	0.07	3.64	<0.01	12	3.66	2.64	0.12	2.63	0.56	54	0.06	1.51	5.97	99.28
RG-97-1281	9.77	0.02	19.8	<0.01	7.91	0.69	2.1	0.22	2.62	0.4	40.69	0.05	1.17	12.63	98
RG-97-2300	11.42	0.18	1.43	<0.01	3.73	5.94	0.36	0.07	1.72	<0.01	74.69	0.01	0.29	1.33	101
RG-96-947	12.09	0.06	11.3	<0.01	9.46	1.6	2.59	0.23	3.8	0.5	47.25	0.02	1.42	10.21	100.45
RG-6-175	15.07	0.1	7.3	0.01	9.34	1.61	6.28	0.12	2.29	0.37	51.39	0.08	1.22	6.4	101.4
RG-6-380	8.89	0.1	1.61	<0.01	3.47	2.63	0.72	0.07	2.4	0.03	79.28	0.01	0.24	1.84	101.2
RG-62-93	15.53	0.04	7.88	0.01	9.14	0.89	6.69	0.13	2.2	0.32	49.86	0.02	1.1	6.67	100.4
MUC-82-111	12.18	0.18	0.39	<0.01	3.7	6.24	0.5	0.06	1.51	0.02	73.97	<0.01	0.33	2.17	101.05
MUC-82-145	10.18	0.14	0.97	<0.01	3.19	4.84	0.25	0.06	1.86	<0.01	77.73	<0.01	0.22	1.71	101
MUC-82-222	11.98	0.01	1.47	<0.01	2.52	0.41	0.18	0.05	6.3	<0.01	75.42	<0.01	0.27	1.77	100.35
MUC-82-406	12.55	0.11	3.91	<0.01	11.67	2.87	2.26	0.18	2.78	0.65	55.89	<0.01	1.8	4.97	99.53
MUC-82-538	12.9	0.11	4.81	<0.01	10.88	2.72	2.44	0.17	3	0.59	57.51	<0.01	1.77	4.49	101.3
RG-97-400	10.93	0.19	5.17	<0.01	4.12	3.77	0.26	0.1	1.97	<0.01	65.71	0.01	0.33	5.45	97.81
RG-96-635	13.87	0.12	1.05	<0.01	5.63	3.06	1.27	0.09	2.21	0.1	68.48	<0.01	0.69	5.25	101.7
RG-6-600	10.28	0.08	2.65	<0.01	3.52	2.44	1.28	0.06	2.22	0.01	72.45	<0.01	0.23	5.25	100.4
RG-62-457	11.66	0.11	2.49	<0.01	4.98	4.84	1.21	0.08	0.61	0.1	64.6	<0.01	0.6	7.3	98.47
RG-97-1962	11.34	0.2	1.99	<0.01	3.59	4.47	0.42	0.07	2.89	0.04	74.21	<0.01	0.38	2.29	101.7
MI-S-1	16.81	0.07	8.58	0.02	8.45	0.92	6.08	0.14	2.76	0.23	53	0.05	0.98	1.51	99.48
MI-S-61	11.37	0.05	0.58	<0.01	2.6	4.57	0.26	0.02	2.37	0.01	77.2	<0.01	0.24	2.09	101.3
MI-S-63	9.02	0.15	0.2	0.01	1.35	6.48	0.1	<0.01	0.64	<0.01	78.64	<0.01	0.22	0.94	97.6
MI-S-41	18.08	0.03	10.35	0.01	8.55	0.81	7.15	0.14	2.39	0.16	47.27	0.03	0.77	4.5	100.2
MI-S-45	13.15	0.08	5.77	<0.01	12.68	1.64	3.6	0.19	2.62	0.57	49.27	0.01	1.81	7.54	98.84
MI-S-42-2	16.01	0.07	9.75	0.04	9.84	1.12	6.26	0.15	2.63	0.25	49.83	0.02	1.09	2.65	99.62
MI-S-54	12.32	0.14	4.98	<0.01	12.65	4	1.97	0.14	1.81	0.69	51.21	0.03	1.92	7	98.69
MKK-PG-28	17.01	0.07	9.46	0.01	10.03	1.13	5.51	0.16	2.97	0.39	48.94	<0.01	1.28	3.62	100.5
MKK-PG-29	16.42	0.08	9.04	0.01	10.06	1.56	4.88	0.15	2.88	0.39	49.17	0.06	1.36	4.1	100
MKK-265-1418	12.39	0.36	1.35	<0.01	5.24	5.16	0.4	0.09	3.07	<0.01	67.11	<0.01	0.45	2.61	97.87
MKC-201-4260	11.09	0.15	1.38	<0.01	2.92	3.97	0.25	0.06	3.06	<0.01	74.49	0.01	0.26	1.72	99.2

1 ALS Chemex analytical method

Method[1]	2855	2501	2858	2502	2503	2504	2861	2505	2842	2506	2507	2508	2844	2509	2510	2864	2511	2870	2867
Sample ID	Ba	Ce	Cs	Dy	Er	Eu	Ga	Gd	Hf	Ho	La	Lu	Nb	Nd	Pr	Rb	Sm	Sn	Sr
	ppm	ppm	ppm	ppm	ppm	ppm	ppm	ppm	ppm	ppm	ppm	ppm	ppm	ppm	ppm	ppm	ppm	ppm	ppm
RG-97-1962	1645	128.5	5.2	13.3	8.8	2.2	22	11.6	12	2.8	61	1.4	24	63	16.2	123.5	13.1	4	66.5
MI-S-1	623	39	4.7	4.3	3	1.4	18	4.7	3	1	17.5	0.4	7	22	5.2	19.2	4.7	<1	368
MI-S-61	509	106	3.4	9.1	6.6	0.9	22	7.5	14	2.2	52	1.2	27	52	13.9	170	9.5	2	33.8
MI-S-63	1175	78.5	1.4	9.6	7.2	1.1	16	7.1	12	2.3	37.5	1.2	21	39	10	177	7.8	3	26.1
MI-S-41	287	26.5	0.6	3.2	2.1	1	17	3.2	1	0.7	12	0.3	4	15	3.6	17.8	3.1	<1	307
MI-S-45	600	63	0.4	6.9	4.1	2	20	7.2	4	1.5	28	0.6	9	35.5	8.3	40.2	7.2	1	279
MI-S-42-2	505	39	1.4	4.9	3.2	1.4	18	4.8	3	1	18.5	0.4	7	23	5.3	24.8	5.3	<1	302
MI-S-54	1155	91.5	2.3	8.9	5.2	2.5	21	9.2	7	1.9	42.5	0.7	16	51	12.3	123	10.1	1	290
MKK-PG-28	525	47.5	11.6	5.5	3.5	1.6	19	5.7	3	1.2	22	0.5	8	27	6.5	15.2	5.5	<1	371
MKK-PG-29	614	53.5	6.3	6.3	3.5	1.7	20	6	4	1.3	24.5	0.5	9	31	7.3	28	7	<1	378
MKK-265-1418	2910	123.5	1.1	13	8.1	2.8	24	11.9	12	2.9	59.5	1.4	25	63.5	15.9	118.5	12.9	3	66.4
MKC-201-4260	1195	126	0.8	13	8.6	1.8	20	11.3	13	2.8	61	1.4	24	62	16	91.8	12.3	3	48.5

1 ALS Chemex analytical method

Method[1]	2868	2512	2550	2869	2513	2549	2871	2873	2514	2875	2865	2859	2860	2863	2862	2872	2874
Sample ID	Ta	Tb	Th	Tl	Tm	U	W	Y	Yb	Zr	Ag	Co	Cu	Ni	Pb	V	Zn
	ppm	ppm	ppm	ppm	ppm	ppm	ppm	ppm	ppm	ppm	ppm	ppm	ppm	ppm	ppm	ppm	ppm
RG-97-1962	1.5	2.4	13	0.5	1.3	4	2	79.5	9.1	477							
MI-S-1	<0.5	0.9	2	<0.5	0.4	0.5	1	26	2.9	126							
MI-S-61	1.5	1.6	18	<0.5	1.1	4.5	2	57	7.7	550							
MI-S-63	1	1.6	12	0.5	1.1	4	3	61.5	7.3	460	<1	0.5	10	<5	10	<5	25
MI-S-41	<0.5	0.6	2	<0.5	0.3	0.5	<1	19	2	82.5	<1	39.5	40	80	<5	175	70
MI-S-45	<0.5	1.4	4	<0.5	0.7	1	1	39.5	4	170	<1	31.5	40	15	5	350	140
MI-S-42-2	<0.5	1	3	<0.5	0.4	0.5	<1	28	3	125.5	<1	40	25	30	<5	240	190
MI-S-54	<0.5	1.7	7	<0.5	0.7	2	1	48.5	4.7	262	<1	19	20	<5	5	80	150
MKK-PG-28	<0.5	1	3	<0.5	0.5	0.5	<1	31	3.1	145.5	<1	37.5	30	50	<5	235	105
MKK-PG-29	<0.5	1.2	4	<0.5	0.6	1.5	<1	33.5	3.6	160	<1	36.5	25	35	30	235	105
MKK-265-1418	1	2.3	13	0.5	1.3	4	1	74	8.7	436	<1	1.5	15	<5	10	10	155
MKC-201-4260	1	2.3	13	0.5	1.3	4	3	75.5	9	465	<1	1.5	25	<5	30	15	195

1 ALS Chemex analytical method

Method[1]	XRF06	XRF06	XRF06	XRF06	XRF06	XRF06	XRF06	XRF06	XRF06	XRF06	XRF06	XRF06	XRF06	XRF06	XRF06
Sample ID	SiO2	Al2O3	Fe2O3	CaO	MgO	Na2O	K2O	Cr2O3	TiO2	MnO	P2O5	SrO	BaO	LOI	Total
	%	%	%	%	%	%	%	%	%	%	%	%	%	%	%
MI-S-62	54.81	15.24	9.32	7.17	4.79	3.11	2.14	0.02	1.19	0.16	0.37	0.04	0.09	1.08	99.52
MI-S-106	79.83	9.92	0.68	0.28	0.18	0.75	4.92	0.04	0.32	<0.01	0.03	0.01	0.25	2.15	99.37
MI-S-70	71.51	13.58	2.17	0.71	0.13	2.91	5.56	0.02	0.52	0.02	0.08	0.02	0.24	2.71	100.2
MI-S-55	48.1	13.75	12.29	6.8	2.99	2.9	2.21	0.01	1.86	0.18	0.65	0.04	0.09	7.94	99.8
MI-S-109	74.98	12.34	2.38	0.16	0.03	3.19	5.43	0.02	0.29	0.01	0.03	<0.01	0.04	0.79	99.69
MI-S-69	90.31	0.85	0.93	0.1	0.06	0.09	0.21	0.01	0.51	0.15	0.03	0.01	0.07	4.91	98.24
MI-S-41	48.43	17.81	8.08	10.17	7.01	2.12	0.72	0.03	0.8	0.14	0.2	0.03	0.04	4.39	99.96
MI-S-11	78.95	11.47	0.47	0.23	0.04	3.11	4.95	0.03	0.19	<0.01	0.04	<0.01	0.06	0.32	99.87
NVR-3	47.85	16.22	10.93	11.96	8.44	2.23	0.25	0.05	1.29	0.18	0.16	0.02	0.04	0.16	99.79
MI-S-75	76.29	12	1.12	0.25	0.18	0.49	5.76	0.04	0.39	0.01	0.05	0.01	0.21	2.5	99.3
MI-S-59	73.98	9.99	4.71	0.14	0.25	0.71	5.2	0.01	0.42	0.01	0.06	0.01	0.31	3.62	99.41
MI-S-112	68.73	12.81	5.17	1.41	0.36	1.6	3.84	<0.01	0.43	0.09	0.06	0.01	0.2	4.64	99.36
MI-S-118	65.92	13.76	5.86	0.59	1.05	3.56	3.49	0.01	0.73	0.07	0.13	0.01	0.15	4.14	99.47
NVR-4	73.91	12.44	2.63	0.86	0.06	2.79	5.31	0.01	0.26	0.04	0.06	0.01	0.15	0.51	99.05
NVR-5	71.43	12.6	2.99	1.67	0.16	2.46	5.14	0.01	0.26	0.06	0.04	<0.01	0.07	2.25	99.16

[1] ALS Chemex analytical method, ME

Method[1]	MS81	MS81	MS81	MS81	MS81	MS81	MS81	MS81	MS81	MS81	MS81	MS81	MS81	MS81	MS81	MS81	MS81	MS81	MS81	MS81
Sample ID	Ag	Ba	Ce	Co	Cr	Cs	Cu	Dy	Er	Eu	Ga	Gd	Hf	Ho	La	Lu	Mo	Nb	Nd	Ni
	ppm	ppm	ppm	ppm	ppm	ppm	ppm	ppm	ppm	ppm	ppm	ppm	ppm	ppm	ppm	ppm	ppm	ppm	ppm	ppm
MI-S-62	3	765	59.4	28.7	120	1.8	13	5.7	3.6	1.5	19	6.4	5	1.2	28.4	0.5	3	12	29.1	29
MI-S-106	2	2490	110	0.9	350	3	<5	8	5.1	1.3	14	8.2	12	1.6	55.2	0.8	10	29	44.4	7
MI-S-70	2	2430	145.5	1.3	110	3	8	11.2	7	2.3	23	11.8	20	2.4	74	1.1	7	41	62	<5
MI-S-55	1	739	62.7	30.2	40	1.7	23	7	4.2	1.8	21	7.4	5	1.4	28.1	0.6	<2	12	32.9	13
MI-S-109	1	316	68.3	1	130	2.9	<5	8.8	6.5	0.6	22	6.2	16	2	23.1	1.1	6	36	24.2	6
MI-S-69	1	597	7.9	1.1	100	12.6	<5	0.7	0.5	0.1	2	0.7	8	0.1	2.2	0.1	5	18	3.7	<5
MI-S-41	1	283	26.8	38.2	210	0.6	28	3.2	1.9	0.9	16	3.3	2	0.6	11.8	0.3	2	6	13.2	84
MI-S-11	<1	384	101.5	0.7	190	2.6	<5	8.7	5.5	0.8	25	9.1	14	1.8	49.2	0.9	6	41	46.7	5
NVR-3	1	263	12.8	47.8	350	<0.1	79	3.7	2.3	1.1	17	3.1	2	0.8	6.9	0.4	2	4	8.6	138
MI-S-75	1	2040	128	0.7	230	4.9	<5	9.7	6.2	1.7	19	10.2	14	2.1	66.7	0.9	7	36	53.5	6
MI-S-59	<1	3090	35.3	1.7	80	10.6	9	4	2.7	0.6	12	3.4	7	0.8	17	0.5	3	21	15	<5
MI-S-112	<1	1950	128.5	1.7	40	3.6	<5	12.2	8.1	2.4	24	12.2	13	2.6	65.8	1.3	6	28	60	<5
MI-S-118	<1	1380	113	10.1	50	1.4	8	10.6	6.7	1.9	23	10.4	12	2.2	47.9	1.1	<2	26	46.7	7
NVR-4	<1	1465	258	1.5	180	4	<5	12.8	8.2	1.7	24	14	12	2.7	92.7	1.2	6	34	74.9	6
NVR-5	<1	759	173	1	100	2	<5	13	8.2	1.3	25	14.1	14	2.7	89.2	1.3	5	37	75.8	<5

[1] ALS Chemex analytical method, ME

Method[1]	MS81	MS81	MS81	ME-MS8	MS81	MS81	MS81	MS81	MS81	MS81	MS81	MS81	MS81	MS81	MS81	MS81	MS81	MS61
Sample ID	Pb	Pr	Rb	Sm	Sn	Sr	Ta	Tb	Th	Tl	Tm	U	V	W	Y	Yb	Zn	Zr	Ag
	ppm	ppm	ppm	ppm	ppm	ppm	ppm	ppm	ppm	ppm	ppm	ppm	ppm	ppm	ppm	ppm	ppm	ppm	ppm
MI-S-62	15	7.5	69.3	6.3	2	359	0.8	1	9	<1	0.6	2.6	210	3	32.9	3.4	116	159	0.4
MI-S-106	13	12.6	132.5	8.6	3	107	2.2	1.3	17	<1	0.9	7.1	<5	4	45.7	5.2	12	384	0.35
MI-S-70	23	16.9	142	12.1	5	181	2.9	1.9	25	<1	1.2	6.4	16	4	63.7	7.1	46	655	0.31
MI-S-55	7	8.2	65.9	7.4	1	428	0.8	1.2	5	<1	0.7	1.5	379	6	39.4	4	131	161	6.71
MI-S-109	51	6.7	186.5	5.6	5	14	2.5	1.3	22	<1	1.2	6.2	<5	4	52.5	6.9	201	504	0.22
MI-S-69	9	1	6.7	0.6	3	53.7	1.5	0.1	1	<1	<0.5	1.2	12	6	4.6	0.5	12	245	0.1
MI-S-41	5	3.3	17.6	3	<1	332	<0.5	0.5	2	<1	<0.5	0.7	178	2	18.1	1.8	78	70.6	0.12
MI-S-11	23	12.9	166.5	9.4	3	20.5	3.1	1.5	37	<1	1	5.8	<5	4	42.6	6	15	355	0.25
NVR-3	<5	1.8	1.8	2.6	<1	230	<0.5	0.6	<1	<1	<0.5	<0.5	289	2	22	2.3	73	52.1	0.12
MI-S-75	10	15.2	186.5	10.7	4	83.2	2.6	1.6	21	<1	1.1	8.5	10	4	54.9	6.1	11	465	1.01
MI-S-59	12	4.2	239	3.4	2	78.7	1.1	0.6	8	<1	0.5	2.4	38	5	22.6	2.9	33	164.5	0.12
MI-S-112	20	16.2	135	12.2	4	116	1.8	2	16	<1	1.4	4.4	8	3	68.7	8.4	126	465	0.11
MI-S-118	20	12.3	91.3	10.1	4	99.8	1.7	1.7	15	<1	1.1	3.9	73	4	58.8	6.6	127	393	0.16
NVR-4	31	21.3	184	14.3	5	120	2.7	2.2	33	<1	1.4	6.6	6	5	71.5	7.8	85	384	0.07
NVR-5	29	20.8	194.5	14.5	5	49.3	2.6	2.2	24	<1	1.4	7.7	<5	3	77	8	116	456	0.77

[1] ALS Chemex analytical method, ME

Method[1]	MS61	MS61	MS61	MS61	MS61	MS61	MS61	MS61	MS61	MS61	MS61	MS61	MS61	MS61	MS61	MS61	Hg-CV41	MS61
Sample ID	Al	As	Ba	Be	Bi	Ca	Cd	Ce	Co	Cr	Cs	Cu	Fe	Ga	Ge	Hf	Hg	In
	%	ppm	ppm	ppm	ppm	%	ppm	ppm	ppm	ppm	ppm	ppm	%	ppm	ppm	ppm	ppm	ppm
MI-S-62	8.86	0.3	690	1.5	0.04	4.85	0.15	61.2	29.8	79	1.77	15.8	6.19	20.4	0.21	3.7	0.01	0.076
MI-S-106	5.01	8.3	2360	2.07	0.11	0.15	0.05	105.5	0.6	209	2.83	2.1	0.46	13.9	0.28	10.8	0.6	0.042
MI-S-70	7.24	5.6	2230	3.01	0.01	0.49	0.09	157.5	1.2	61	3.14	9.1	1.5	25.7	0.31	2.3	0.31	0.109
MI-S-55	7.74	8	660	2.84	0.03	4.76	0.16	63.1	31.4	37	1.72	28.4	8.27	22.2	0.24	0.4	0.04	0.088
MI-S-109	6.56	3.1	290	3.57	0.05	0.12	0.07	68.4	0.7	76	2.87	2.8	1.72	24.5	0.23	6.1	0.07	0.118
MI-S-69	0.43	3.6	560	0.79	0.23	0.06	0.14	7.91	0.9	62	12.4	3.5	0.66	2.48	0.07	1	0.85	0.006
MI-S-41	10.9	0.5	270	0.68	0.01	7.1	0.11	28.3	41.9	122	0.69	33.7	5.5	17.7	0.15	2.9	0.01	0.05
MI-S-11	5.82	4.9	360	4.84	0.04	0.17	0.06	105.5	0.5	106	2.72	1.7	0.34	27.9	0.24	4.1	0.38	0.045
NVR-3	10.3	1.5	240	0.33	<0.01	8.77	0.12	14	53	217	<0.05	102.5	7.57	18.8	0.13	2.1	<0.01	0.065
MI-S-75	6.19	25.2	1950	2.97	0.07	0.11	0.04	126.5	0.5	138	4.96	2.3	0.67	20.3	0.35	3.7	0.28	0.065
MI-S-59	5.33	34.9	2860	2.03	0.54	0.09	0.13	33.9	1.5	54	10.35	10.4	3.32	11.85	0.1	2.9	1.27	0.115
MI-S-112	7.48	5.4	1780	3.48	0.05	1.01	0.31	126	1.3	24	3.47	3	3.6	25.1	0.13	2.4	0.02	0.142
MI-S-118	7.99	11.1	1280	3.55	0.2	0.41	0.33	108	10.4	32	1.35	9	4.1	25.6	0.1	0.3	0.13	0.142
NVR-4	7.44	6.4	1440	5.61	0.07	0.66	0.2	265	1.3	95	4.04	4.3	1.86	25	0.15	2	0.01	0.092
NVR-5	7.01	2.2	690	4.94	0.04	1.25	0.67	173	0.6	53	1.9	2.7	2.1	25.4	0.13	5.1	0.01	0.108

[1] ALS Chemex Analytical method, ME

Method[1]	MS61	MS61	MS61	MS61	MS61	MS61	MS61	MS61	MS61	MS61	MS61	MS61	MS61	MS61	MS61	MS61	MS61	MS61	MS61
Sample ID	K	La	Li	Mg	Mn	Mo	Na	Nb	Ni	P	Pb	Rb	Re	S	Sb	Se	Sn	Sr	Ta
	%	ppm	ppm	%	ppm	ppm	%	ppm	ppm	ppm	ppm	ppm	ppm	%	ppm	ppm	ppm	ppm	ppm
MI-S-62	1.83	30.2	13.6	2.85	1165	2.51	2.4	8.3	31.7	1720	10.7	69.7	0.002	<0.01	0.11	1	2.2	368	0.21
MI-S-106	3.86	53.5	28.5	0.07	28	8.65	0.53	21.7	6.4	90	17.7	127	0.005	0.09	7.91	<1	3.4	101	0.7
MI-S-70	4.19	76.7	8.1	0.07	140	6.02	1.99	18.2	3	260	28.8	141.5	0.003	0.29	0.45	1	5.4	171.5	0.1
MI-S-55	1.88	29	60	1.74	1355	0.79	2.17	5.9	12.7	3160	4.4	64.8	<0.002	<0.01	1.46	1	1.7	443	0.09
MI-S-109	4.28	24.7	8.9	0.02	74	5.39	2.21	20.4	3.3	90	27.5	197	0.002	0.01	0.4	1	4.6	15.1	0.44
MI-S-69	0.16	3.2	1.3	0.02	1070	4.18	0.11	8.7	2.6	50	7.6	6.8	<0.002	0.19	0.87	<1	3.3	54.1	<0.05
MI-S-41	0.63	13.1	10.2	4.25	1050	1.92	1.76	6.8	90.6	950	3.5	18.6	0.003	0.04	0.08	1	0.8	370	0.3
MI-S-11	3.83	51.9	13.2	0.01	29	5.78	2.1	27.2	4.7	130	26	172.5	0.003	0.01	5.35	1	3.5	23.1	0.97
NVR-3	0.19	5.8	5.8	5.23	1410	0.99	1.86	2.7	148	800	1.5	2.1	0.003	0.11	<0.05	<1	0.4	253	0.06
MI-S-75	4.53	66.7	23.8	0.06	81	6.81	0.35	14.2	5.8	80	15.7	189	0.007	0.05	7.12	13	4.4	82.5	0.42
MI-S-59	4.26	17.4	95.5	0.14	62	2.43	0.54	6.4	4.4	230	12.4	245	<0.002	0.02	15.7	1	1.9	75.6	0.14
MI-S-112	3.33	63.3	70.4	0.23	642	4.89	1.3	5.2	1	190	20.8	127	<0.002	<0.01	2.52	2	4.3	113	0.09
MI-S-118	3.03	50.2	63.7	0.66	526	1.13	2.81	7.5	6.4	410	20	88	<0.002	<0.01	1.62	2	3.3	103.5	0.07
NVR-4	4.59	95.9	44	0.06	443	5.64	2.63	9.6	5.4	230	31.9	196	0.002	<0.01	0.21	3	4.8	123.5	0.09
NVR-5	4.35	87.7	33.9	0.12	526	4.05	2.2	20.8	2	150	31.4	192	0.003	<0.01	0.13	3	5.5	48.7	0.57

[1] ALS Chemex analytical method, ME

Method[1]	MS61	MS61	MS61	MS61	MS61	MS61	MS61	MS61	MS61	MS61
Sample ID	Te	Th	Ti	Tl	U	V	W	Y	Zn	Zr
	ppm	ppm	%	ppm	ppm	ppm	ppm	ppm	ppm	ppm
MI-S-62	<0.05	8.2	0.72	0.42	2.5	190	0.5	29.1	104	159.5
MI-S-106	<0.05	14.8	0.19	0.79	6.3	3	1.7	39	11	409
MI-S-70	<0.05	20.9	0.29	0.72	5.1	17	1.6	51.9	47	166.5
MI-S-55	<0.05	2.2	1.08	0.5	0.7	344	1.7	28.6	139	11.8
MI-S-109	<0.05	18.2	0.14	0.86	5	5	0.8	42	244	378
MI-S-69	<0.05	1.1	0.29	0.64	1	10	1.6	3.8	8	78.6
MI-S-41	<0.05	2.1	0.47	0.15	0.7	164	0.2	15.6	79	98.3
MI-S-11	<0.05	31	0.11	0.74	3.7	7	1.6	34.2	16	124
NVR-3	<0.05	0.5	0.72	<0.02	0.2	286	0.1	20.7	82	69.4
MI-S-75	<0.05	17.4	0.22	0.99	7.7	9	0.9	48.2	7	226
MI-S-59	<0.05	9.1	0.23	0.57	2	34	0.9	15.4	36	51.7
MI-S-112	<0.05	14.9	0.25	0.59	2.7	6	0.6	40.5	156	97
MI-S-118	<0.05	15.3	0.44	0.59	3.3	71	0.9	43.9	162	14.6
NVR-4	<0.05	37.5	0.11	0.91	5	9	1.8	58.9	106	38.4
NVR-5	<0.05	23.8	0.1	1	4.4	2	0.7	54.5	140	65.6

[1] ALS Chemex analytical method, ME

APPENDIX B—REPRESENTATIVE XRD ANALYSIS

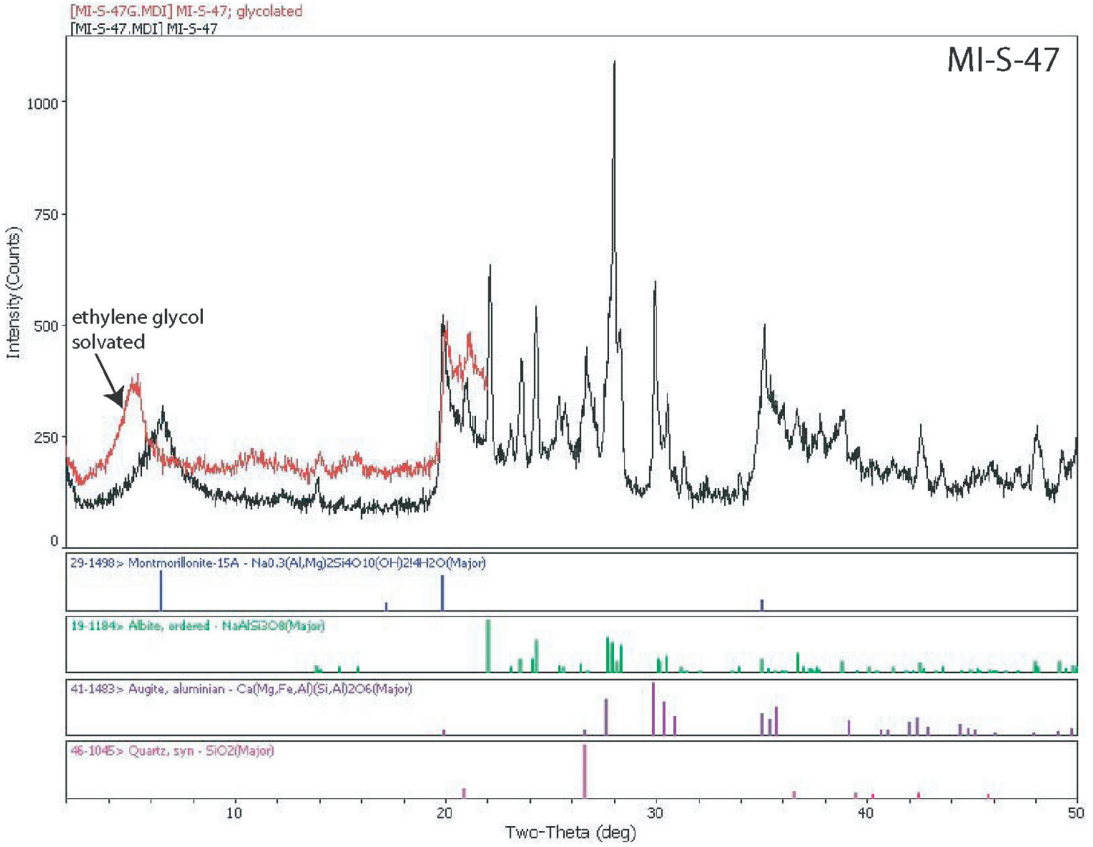

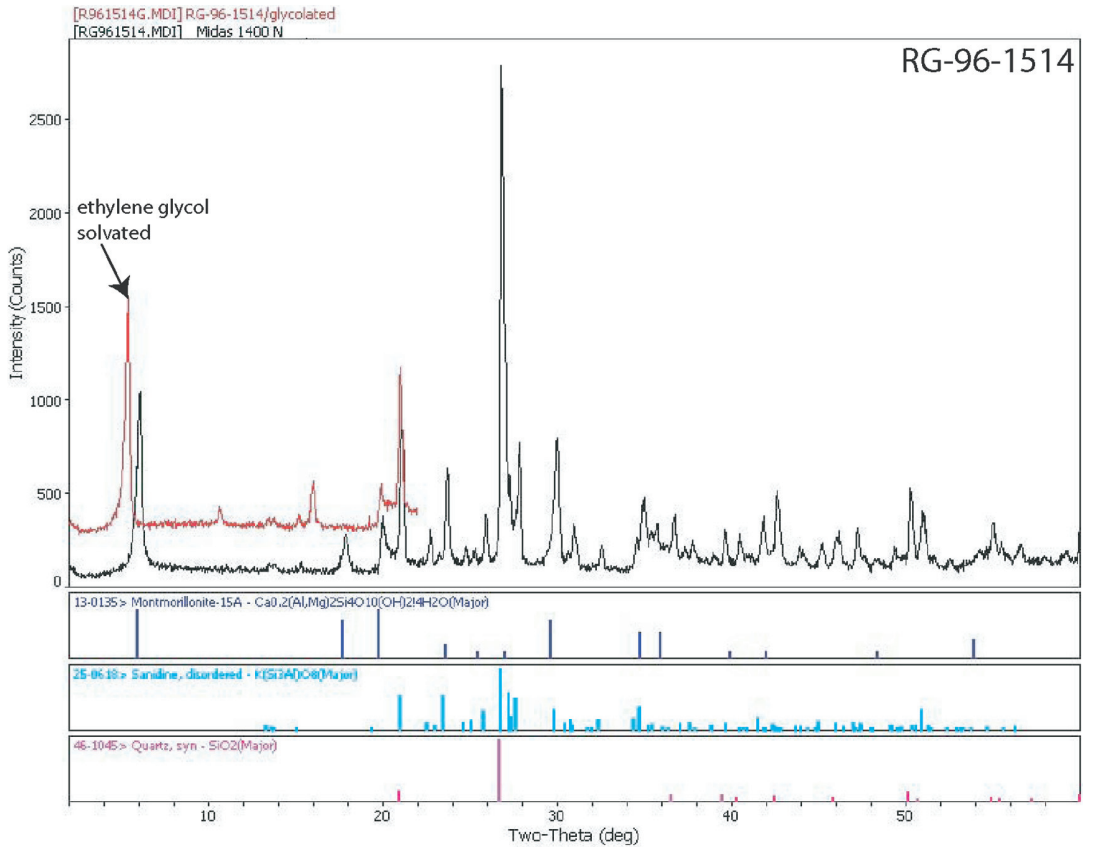

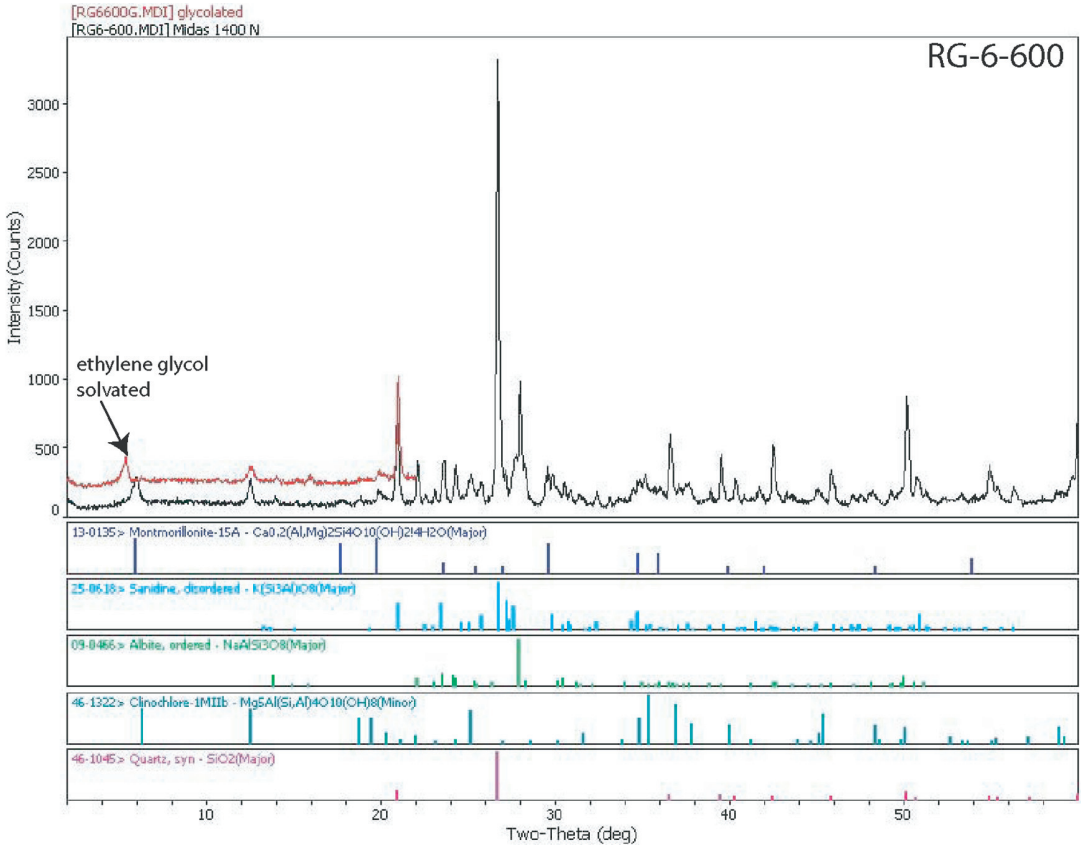
[RG6600G.MDI] glycolated
[RG6-600.MDI] Midas 1400 N
RG-6-600
Intensity (Counts)
ethylene glycol solvated
13-0135> Montmorillonite-15A - Ca0.2(Al,Mg)2Si4O10(OH)2I4H2O(Major)
25-0618> Sanidine, disordered - K(Si3Al)O8(Major)
09-0466> Albite, ordered - NaAlSi3O8(Major)
46-1322> Clinochlore-1MIIb - Mg5Al(Si,Al)4O10(OH)8(Minor)
46-1045> Quartz, syn - SiO2(Major)
Two-Theta (deg)

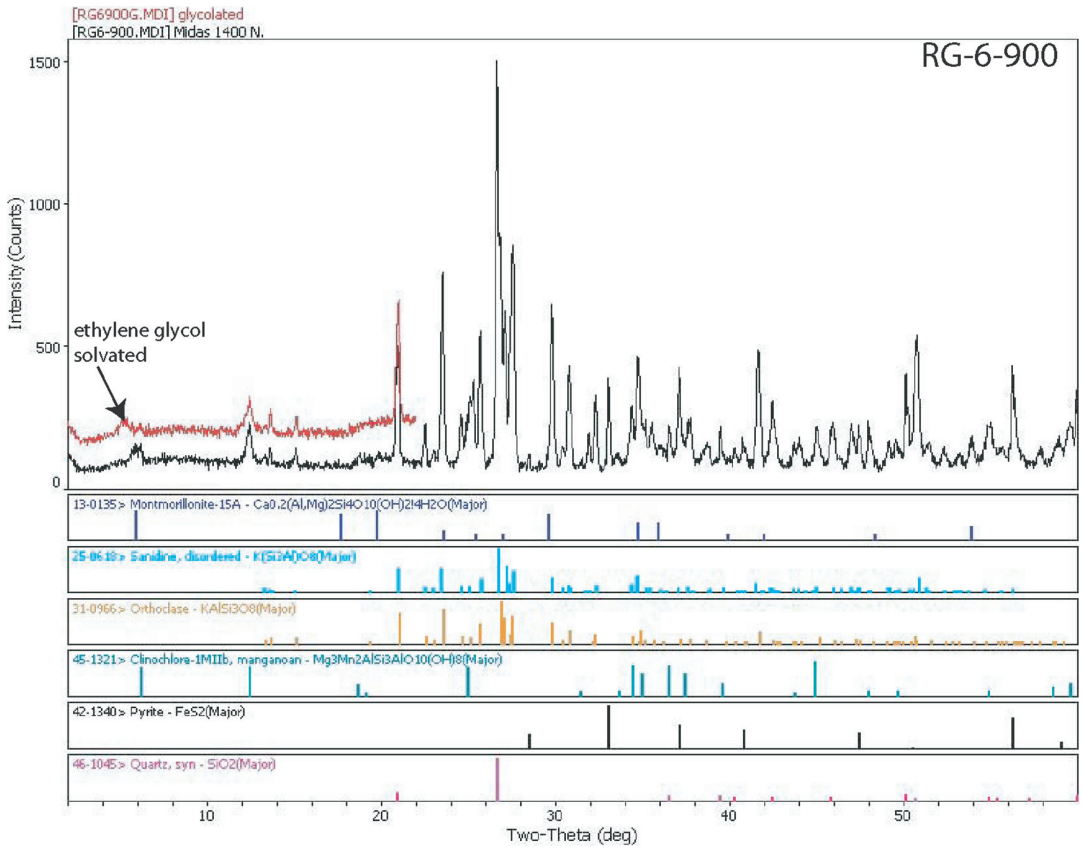
[RG6900G.MDI] glycolated
[RG6-900.MDI] Midas 1400 N.
RG-6-900
Intensity (Counts)
ethylene glycol solvated
13-0135> Montmorillonite-15A - Ca0.2(Al,Mg)2Si4O10(OH)2I4H2O(Major)
25-0618> Sanidine, disordered - K(Si3Al)O8(Major)
31-0966> Orthoclase - KAlSi3O8(Major)
45-1321> Clinochlore-1MIIb, manganoan - Mg3Mn2AlSi3AlO10(OH)8(Major)
42-1340> Pyrite - FeS2(Major)
46-1045> Quartz, syn - SiO2(Major)
Two-Theta (deg)

APPENDIX C—CHLORITE MICROPROBE DATA

RG-97-1962 Vein

	SiO2	Al2O3	CaO	Na2O	K2O	MnO	FeO	TiO2	MgO	O	Total
Average	27.01	14.64	0.13	0.41	0.11	0.38	40.33	0.05	5.68	0.00	88.75
St Dev	0.72	0.68	0.07	0.30	0.12	0.16	1.22	0.05	0.95	0.00	1.83
Max	28.86	15.99	0.30	1.38	0.51	0.81	42.86	0.18	6.94	0.00	92.52
Min	25.46	13.54	0.00	0.00	0.00	0.17	37.43	0.00	3.74	0.00	85.38

Line	SiO2	Al2O3	CaO	Na2O	K2O	MnO	FeO	TiO2	MgO	O	Total
672 G	26.21	15.15	0.13	0.44	0.05	0.30	41.00	0.02	5.21	0.00	88.50
673 G	27.05	14.49	0.16	0.47	0.02	0.20	41.13	0.00	6.94	0.00	90.46
674 G	27.91	14.89	0.10	0.22	0.26	0.41	41.75	0.10	6.23	0.00	91.85
675 G	27.25	13.54	0.03	0.00	0.00	0.25	42.86	0.06	6.44	0.00	90.42
676 G	27.38	14.03	0.19	0.18	0.03	0.47	40.31	0.15	6.19	0.00	88.93
677 G	27.29	14.40	0.11	0.66	0.11	0.33	42.27	0.00	5.71	0.00	90.89
678 G	27.06	13.85	0.20	0.29	0.00	0.81	40.94	0.00	6.48	0.00	89.64
679 G	26.75	13.78	0.16	0.11	0.16	0.22	39.42	0.05	6.39	0.00	87.03
680 G	26.56	14.37	0.15	0.47	0.00	0.47	40.27	0.00	6.61	0.00	88.90
681 G	28.41	14.13	0.00	0.22	0.05	0.42	40.05	0.01	6.53	0.00	89.81
682 G	26.65	13.67	0.30	0.18	0.07	0.17	39.34	0.02	6.13	0.00	86.52
683 G	26.73	13.67	0.17	0.57	0.08	0.41	37.43	0.00	6.32	0.00	85.38
684 G	26.20	13.91	0.16	0.54	0.16	0.36	39.17	0.11	6.33	0.00	86.93
685 G	27.70	14.38	0.22	0.18	0.10	0.53	41.25	0.14	6.69	0.00	91.18
686 G	26.21	14.54	0.25	0.18	0.02	0.70	39.01	0.10	6.49	0.00	87.49
687 G	26.97	14.83	0.15	0.33	0.13	0.62	41.59	0.18	6.25	0.00	91.05
688 G	26.62	13.84	0.14	0.29	0.51	0.33	42.04	0.09	6.47	0.00	90.33
689 G	26.49	14.59	0.08	0.87	0.00	0.64	40.28	0.00	6.41	0.00	89.35
690 G	27.23	14.70	0.10	0.18	0.04	0.36	39.05	0.05	6.02	0.00	87.73
691 G	28.86	14.80	0.00	1.38	0.36	0.39	41.39	0.00	5.34	0.00	92.52
692 G	25.46	15.78	0.10	0.18	0.08	0.47	41.15	0.00	3.74	0.00	86.96
693 G	27.02	15.43	0.08	0.90	0.13	0.44	39.46	0.00	4.23	0.00	87.68
694 G	26.14	15.55	0.22	0.48	0.16	0.22	41.05	0.09	4.31	0.00	88.21
695 G	27.65	15.99	0.16	0.80	0.17	0.17	40.39	0.10	4.41	0.00	89.82
696 G	26.63	15.60	0.13	0.36	0.10	0.17	38.93	0.11	4.55	0.00	86.58
697 G	28.02	15.16	0.15	0.47	0.10	0.28	39.75	0.02	4.43	0.00	88.37
698 G	26.47	15.43	0.00	0.36	0.08	0.31	38.87	0.00	4.73	0.00	86.25
700 G	27.07	15.00	0.09	0.62	0.01	0.28	40.49	0.00	4.67	0.00	88.22
701 G	27.46	14.94	0.18	0.00	0.36	0.35	38.94	0.00	4.39	0.00	86.62